Doctoral Dissertation

Enhanced Virtual Synchronous Generator Strategy by Model Predictive Multivariable Control: Studies on Voltage Source Inverter and Matrix Converter

Jonggrist Jongudomkarn

January 2020

Graduate School of Engineering,
Osaka University

Abstract

Distributed generations (DGs) are expected to be penetrated widely in the future power grid. Virtual synchronous generator (VSG) control can play a vital role in supporting the frequency stability of such a power grid thanks to its virtual inertia feature. However, there still exist some issues that can be improved to enhance the capacity of VSG control. For instance, the transient stability of DG can be significantly improved if VSG control is capable of riding through a short period of transient disturbances such as balanced and unbalanced voltage sag. Furthermore, the existing VSG control is mainly designed for the traditional two-level inverter with an energy storage unit. Hence, it is challenging to implement VSG control in a system without energy storage units such as matrix converters (MCs), as the inertial power cannot be drawn directly from energy storage elements and instead needs to be provided by the input power control. In order to solve the aforementioned issues, studies on the implementation of VSG control using finite control set model predictive control (FCS-MPC) are conducted. In this dissertation, a novel FCS-MPC based method for VSG with fault-ride-through ability is proposed for two-level inverter-interfaced DGs, and a novel approach based on FCS-MPC scheme is introduced for the implementation of VSG controls in indirect boost matrix converter (IBMC)-interfaced DGs.

This dissertation is organized as follows.

In Chapter 1, the background of the research, concepts of power converter-interfaced DGs, their existing types of control methods, challenges in these technologies, and the objectives of this research are discussed.

Principles and reviews of the state of the art of VSG control and FCS-MPC scheme are introduced in Chapter 2 along with their design procedures and control diagrams.

In Chapter 3, the implementation of the two-level-inverter-based VSG using FCS-MPC is proposed. Simulation studies showed that the FCS-MPC based VSG inherits all the properties of the VSG. Moreover, the FCS-MPC-based VSG allows simultaneous control of voltage and current to grant the two-level inverter system with current limiting ability.

In Chapter 4, other existing current limiting methods for two-level inverter-based VSGs are introduced, namely, the VSG with multiloop control and the VSG with virtual impedance current limiting. Several simulation and experimental studies validate the superior fault-ride-through capability of the proposed FCS-MPC-based strategy for both grid-connected and islanded operations in comparison with the other existing methods.

The implementation of VSG control in the IBMC-interfaced DGs using FCS-MPC is studied in Chapter 5. Comparative simulation studies between the proposed control schemes and the existing method have demonstrated that the proposed grid-forming control scheme offers many advantages

over the existing methods, which utilize a grid-following strategy. For instance, the proposed control scheme can operate in both grid-connected and islanded modes, is able to improve the quality of current waveforms significantly, and is capable of providing inertial power to the grid by dispatching active power from the input source. A scale-down experimental study is also conducted to validate the effectiveness of the proposed control scheme.

The dissertation is concluded in Chapter 6, where future challenges and possible future works are also discussed.

Table of Contents

Chapter 1
Introduction

1.1 Background

The indiscriminate uses of fossil fuels to supply indefinite demand of the world's energy have led to the rapid depletion of these non-renewable resources. Furthermore, the exploitation of them is also believed to be the leading cause of global warming and climate change [1]. Thus it was perfectly clear to power engineers and researchers in this field that new ways to generate energy with low emissions and in a sustainable way are imperative. One possible solution for this problem lies in the use of renewable energy sources (RES) such as wind and solar powers. This is clearly evidenced by the global capacity of wind turbines and solar cells, which are increasing annually [2], [3]. However, the limiting factors for the utilization of renewable resources are their intermittent and unpredictable nature.

Unlike conventional power generation, these alternative power sources usually require topologically power-source-dependent power converter in order to transform the energy sources into electrical power and deliver it to the power grid. With the deregulation of utilities and the emerging of power markets, such power-converter-based-power generators are often operating in parallel with the utility system and are connected to the utility distribution system near the loads. Such a method of generation is commonly referred to as "distributed generation" (DG). According to [4], DGs are expected to increase the reliability of the power supply by providing backup power generation for local customers, and with increasing penetration percentage of DGs, it is expected that the transmission loss can be reduced and the transmission/distribution capacity can be relieved. The current paradigm in the control of DGs is to extract the maximum possible power from the sources and to dispatch it all to the power grid. However, this is only acceptable as long as the capacity of DGs is low compared to the total capacity of the power grid, as an increasing percentage of DGs penetration in the power grid implies that a growing number of different power converter topologies and control techniques are working independently on one another in the system. In this situation, the chance of unexpected problems arising is high, and the control methodology that worked in the conventional centralized generation units oriented system might not be working. Hence different control policies for DGs might be required for the future power system.

1.1.1 Power Converter-Based Distributed Generations

DG refers to a variety of small power generation devices, which are located close to the load, helping to satisfy the total demand of the system. The typical power sources of DG technologies include natural gas, diesel-powered reciprocating engines, gas turbines, fuel cells, solar panels, and

wind turbines. DG technologies are generally less than 100 megawatts (MW) in size and can broadly be found in a wide range of configurations. Their applications are not only limited to utility power provider. For instance, distributed power systems can generate electricity in isolation, providing continuous, intermittent, peak, or even back-up power for on-site energy needs.

Most of DGs are equipped with a power-electronics converter at the output terminal, to convert the generated power to the desired voltage and frequency. The topologies of power converter used in these DG systems are naturally dependent on the types and nature of the utilized power sources. However, giving the objective of DGs to deliver power to the AC-grid, the types of power converters that suit the application of DGs are typically DC-AC converters such as voltage-source-inverters (VSI) and multilevel inverter, or AC-AC converters such as matrix converters (MCs) and back-to-back converters (B2Bs). The several power converters that can be deployed in DG applications are concluded, as shown in Fig. 1.1. Conventionally, DG systems consist of three-phase pulse-width-modulation (PWM)-based VSIs or B2Bs, which are employed for power conversion, grid synchronization, and power quality control [5]. However, bulky and lifetime-limited dc-link electrolytic capacitors are still often considered as a disadvantage of VSIs and B2Bs. Hence, MCs are also commonly investigated as a possible alternative configuration for DG Applications. The absence of the dc-link energy storage element, however, increases the complexity of the control algorithm due to the coupling of rectification and the inversion stages.

There are various existing control strategies for DGs, which are aiming for difference control objectives, i.e., active and reactive powers control [6], voltage, and frequency control [7] and etc. For grid-connected operation, the strategies can be classified into two basic types, namely grid-feeding control and grid-forming control [8]. Grid-feeding control treats the DGs as current sources, which are capable of controlling the output active and reactive power by control the amplitude and phase angle of the current injected into the AC bus. Nevertheless, the grid-feeding control is struggling to operate in an islanded network because it is not capable of controlling the grid voltage and frequency by itself. Instead, it commonly depends on the voltage and frequency of the synchronized power grid. As the percentage of DGs currently remains a negligible part compared with the overall grid power capacity, grid-feeding control-based DGs are regularly employed with the policy of extracting the maximum possible power from the sources and delivering it all to the power grid. Voltage and frequency fluctuation in the system caused by the injected power of DGs will be suppressed by the rotating mass and inertial response of conventional generators. Thus the system has the ability to stabilize itself and ride-through faults [9].

Grid-forming control, on the other hand, refers to a control strategy that enables the DG to act as a voltage source. The grid-forming-based DG is capable of regulating the voltage and frequency at the output terminal. Such DGs are able to form an independent islanded network and to control their output frequency to support grid frequency stability actively. However, this control method is conventionally not suitable for parallel operation with other grid-forming control-based DGs or the power grid. Nevertheless, frequency and voltage control in microgrids supplied by a number of voltage

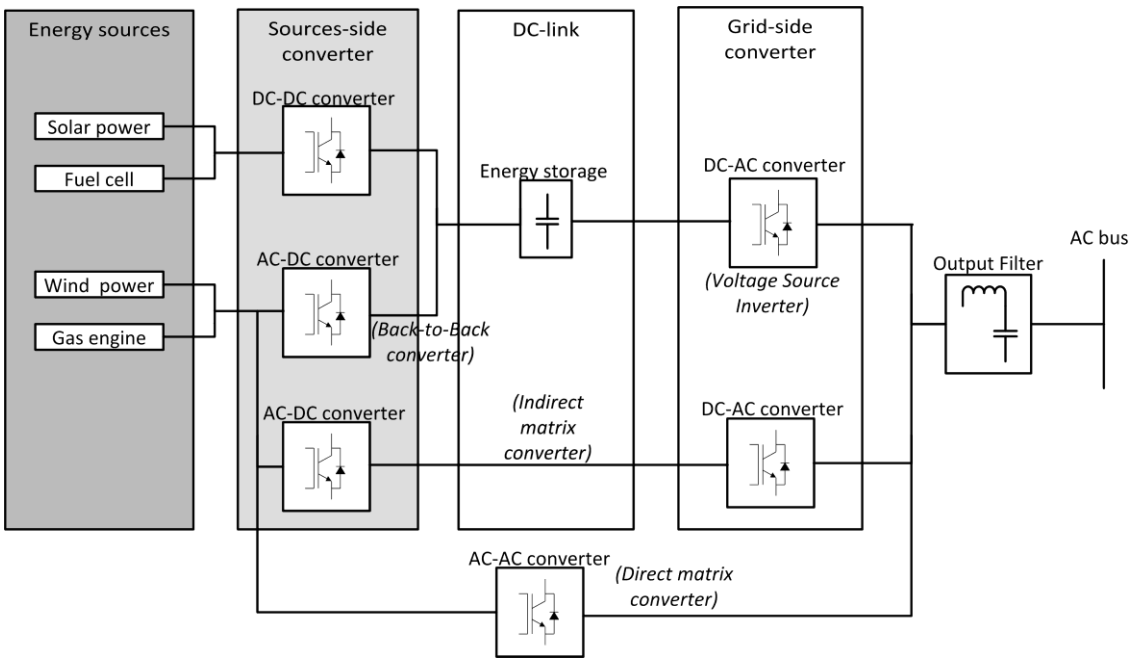

Fig. 1.1 General structure of power converter-interfaced distributed generators.

sources connected in parallel can be obtained using the droop control method, as proposed in [10] and shown in Fig. 1.2(a). In the referred work, the real and reactive power regulation is conducted according to the characteristics of the parallel operating synchronous generators (SGs). This method has been developed into a general approach for parallel inverters in microgrids, as studied in [11]–[18]. Likewise, droop control can be integrated with grid-feeding control. In this case, the droop characteristic will be utilized to determine active and reactive power command for DGs, as shown in Fig. 1.2(b). However, as power converter-interfaced DGs become the majority of the grid capability, the droop control methods cannot provide sufficient rotational inertia to ensure power grid stability [19]. As a result, the perturbation in the power frequency under the influence of changes in their net load will become much higher. Hence, in order to prevent an issue of frequency stability arising from the increasing share of DGs in the future electricity generation system, an approach called virtual Synchronous Generator (VSG) control was proposed in [20]. It stated that by letting the power electronics interface of the DG unit emulate the behavior of a real synchronous machine, a reaction similar to that of self-stabilizing synchronous generators to a disturbance in the system could be observed. VSG control can be adopted along with both voltage source control and current source control. However, the most adopted is the one with voltage source control, as illustrated in Fig. 1.2(c).

In accordance with the past research works of VSG, the results have clearly shown the advantages of using this concept in DGs to solve issues related to frequency deviations [21]–[27]. However, despite the success of VSG control, there are some issues for VSG control that still required some improvement. First, the proposed VSG controls [21]–[27] lack a current control loop, which makes it sensitive to fault conditions. Although some current limiting methods are proposed for VSG [28],

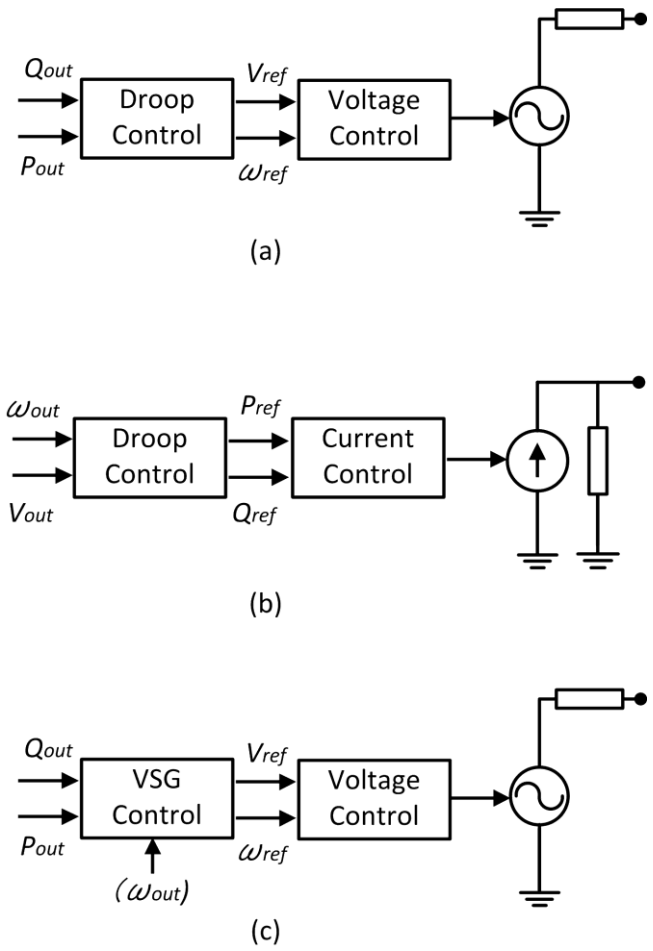

Fig. 1.2 Control methods of DGs.

(a) Voltage-source-based droop control. (b) Current-source-based droop control.

(c) VSG control [27], [19].

[29], the controls are still immature and have a lot of room for enhancement. Second, the studies on VSG so far are mostly done in the two-level-inverter-based system, and a study on other systems such as matrix converter is rare despite the many advantages of MCs. The corresponding reason for this might be the complex coupling between the rectifier and the inverter stages of MCs, which makes the implementation of VSG rather complicated and demanding. In order to get rid of the weakness in VSG control and to enhance the capability of the VSG control, a different methodology to implement VSG control is the subject of study in this dissertation.

1.1.2 Types of Power Converter Control Schemes

Several control techniques have been widely applied to power converters, according to [30]. These include linear and nonlinear controllers, adaptive control, repetitive control, fuzzy control, and predictive control , as shown in Fig. 1.3. Some of these use a straightforward algorithm such as hys-

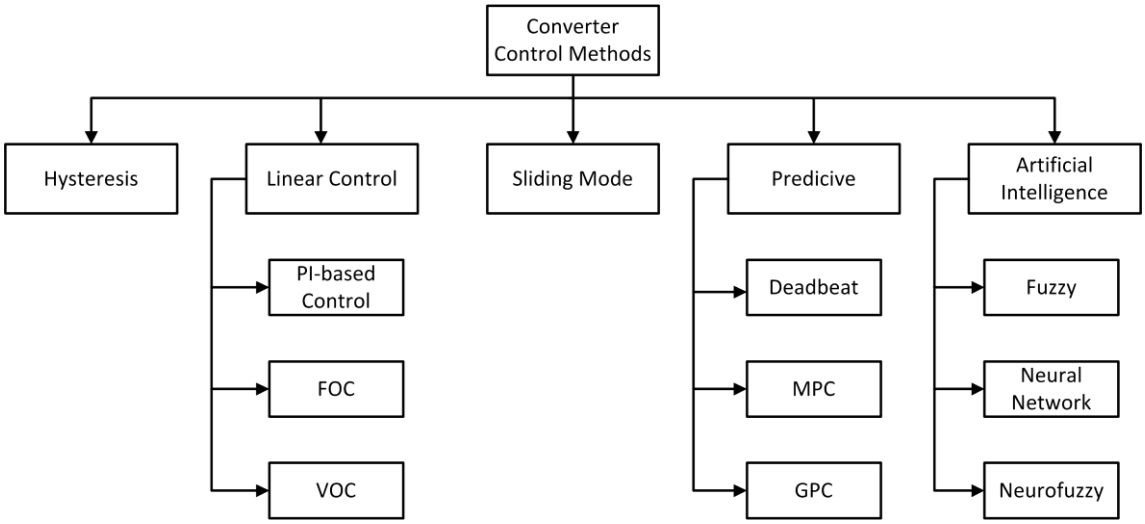

Fig. 1.3 Difference types of converter control schemes

teresis control, while some are generally complex and need relatively high calculation power such as fuzzy logic and neural network controls. The most commonly used control strategies illustrated in Fig. 1.3 will be introduced in this subsection. First, hysteresis control uses a comparison of the measured variable to its reference in order to determine the switching states of the power converters. Every time the error between control references and measured variables crosses the hysteresis band's boundary, a significant change in the switching state occurs. However, it has origin in analog electronics. Hence, in order to implement the control in a digital platform, a very high sampling frequency is required in order to capture the exact moment the error crosses the hysteresis band. Moreover, it generates a variable switching frequency, which might excite the output filter resonance. The example of hysteresis control is studied in [31].

With the presence of a modulation stage for generating signals of the power converter, any linear controller can be used with the power converter. The preferable choice is a proportional-integral (PI) controller. However, the PI control scheme is a single variable control and often requires an additional coordinate transformation in order to convert the control variables into a DC-form. Hence, a cascade control structure is required for controlling multiple inputs. This leads to several design steps and considerations in the process of achieving suitable control methods, which is challenging for the implementation in some systems such as MCs or multilevel converters. On the other hand, the rapid development of microprocessors and computer techniques has enabled the possibility of implementing new control schemes for power converters. These include fuzzy logic control, neural networks, sliding mode control, and predictive control, just to name a few. Among these emerging control methods, predictive control shows promising potential for the control of DGs and offers the possibility of enhancing the capability of VSG control. Although profoundly different approaches exist within the family of predictive control, all share a standard concept, which is to use the system

model for the prediction of the future system's behaviors and to employ an optimization criterion in order to determine the optimal actuation of the power converter.

One of the most studied predictive control for power converters is a finite control set model-predictive control (FCS-MPC), owing to its benefits of having a flexible control scheme that allows easy inclusion of multiple control variables, system constraints, and nonlinearities. A number of control solutions based on FCS-MPC for DG application appeared in the literature [32]–[36]. Compared with the classic linear PI and PWM controller, the MPC offers many advantages, including minimizing steady-state errors over a wide target frequency range, minimal harmonic distortion, fast dynamic response, and maximum dc-link utilization.

Considering the operation of VSG control-based DGs, several controls and regulations need to be regulated. Some of these are essential to ensure proper operation of DGs and to maintain power system stability, like the voltage and frequency control, while others are imposed for security reasons, like current limitations and voltage restrictions. This characteristic converges in a natural way to the utilization of FCS-MPC, as it is multiple-inputs-multiple-outputs (MIMO)-based control that has the ability to control several control variables and constraints at the same time via the inclusion of those terms in a single cost function. In addition, since the design of any control system must take into account the model of the system for adjusting the controller parameters, the employment of model predicting control will only simplify the control system design. This is beneficial for complex systems such as MCs-interfaced and multilevel converter-interfaced DGs. Furthermore, with practically all current control strategies being implemented in discrete time, the rapid advancement of the control platform, and the discrete nature of power converters that require a discrete signal to command the turn-on and turn-off of their switching devices, the compatibility of FCS-MPC for power converter-based DG are clearly highlighted as shown in Fig. 1.4.

1.2 Research Objectives

As it is discussed in the previous parts of this chapter, the utilization of DGs is a promising solution for the problem of the ever-growing energy demand and for the reliability enhancement of the local power supply by providing backup power generation. Currently, the VSG control is a highly-rated control method for power converter-interfaced DGs, as it can provide better dynamic performance and higher inertial response than conventional droop control. Still, other concerns over grid stability exist for VSG control, as the capacity of the DG-base system keeps increasing compared to the total capacity of the power grid. One of the most critical concerns is the interrupted or unstable operation in the DG system due to the effect of transient disturbances on the utility grid since the most frequently adopted VSG control does not have a proper current loop control. Without a proper countermeasure, the whole grid could suffer from a massive imbalance between the power supply and power demand. Furthermore, the traditional design of VSG control uses two-level-inverters as the primary circuit. Such a control design utilizes the measured output power to determine the frequency command and to generate a virtual inertial response. This is possible be-

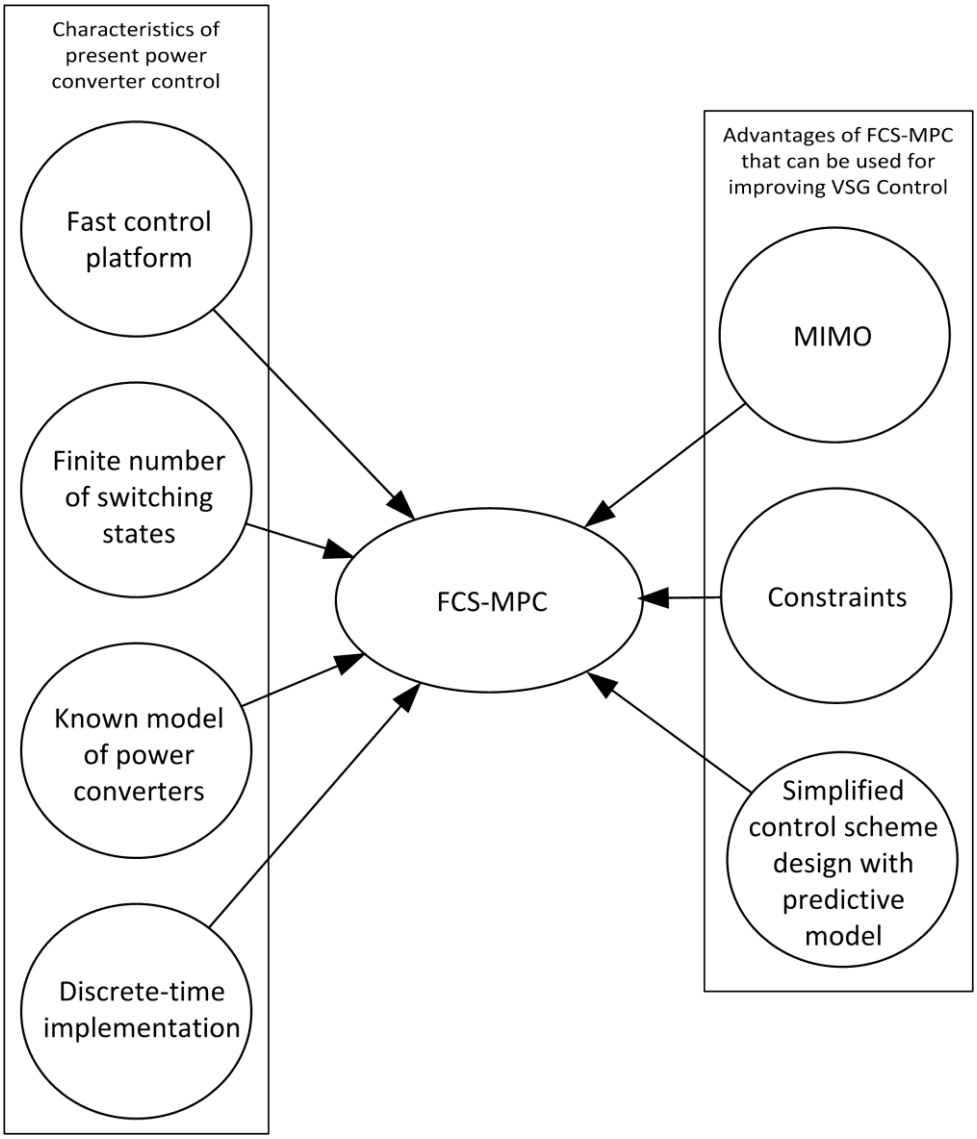

Fig. 1.4 Characteristics of FCS-MPC that makes it a potential solution for improving VSG control

cause the output power of such a system can be drawn directly from the energy storage element, and the power is dependent on the power angle between DG and the output network. However, for a conversion system without an energy storage element such as MCs, the output power is dispatched from the input power control and has no relation to the output network. Hence, it is clear that different method to generate virtual inertia is imperative.

In order to resolve the aforementioned issues of the VSG control, a study is conducted in this dissertation with FCS-MPC as a potential solution. FCS-MPC uses the system modeling to predict future system states and posses the ability to control multiple control objectives via calculation of cost function. The main aims of this research can be divided into two.

1. The first aim is to study the state of the arts methods of model predictive control for grid-connected DG systems, three-phase voltage-source inverters (VSIs) and then to optimize theses existing models, in the aspects which are overlooked in the preceding

works, especially on the power system stability issues that are occurring with the wide-spread of DG units. This is, for instance, the ability to self-stabilize the power system of VSG and ride through disturbances.

2. The second purpose of this study is to implement the VSG control in three-phase MC-interfaced DG using FCS-MPC algorithms as the primary solution. In this method, the inertial power needs to be dispatched directly from the input power control instead of the energy storage element.

Detailed discussions in the following chapters are organized as follows. In Chapter 2, the principles of VSG control and the principle and design procedure of FCS-MPC are introduced. In chapter 3, the implementation and design procedure of VSG in the two-level-inverter-interfaced system using FCS-MPC is studied. The study also verifies that the VSG control implemented by FCS-MPC inherits all the properties of PWM-based VSG control to support the power system stability. In chapter 4, in order to display the superior fault-ride-through ability of the proposed VSG control over other existing methods for inverter-based VSG control, namely the VSG with multiloop control and the VSG control with virtual impedance current limiting, comparative studies between FCS-MPC-based control and existing control are conducted with simulation and experiment results. In chapter 5, the existing control schemes for the indirect matrix converter, along with its advantages and disadvantages, are discussed. In response to that, a novel VSG control for indirect matrix converters using FCS-MPC is proposed as an improvement over the previous controls. The proposed control is able to generate a less distorted current waveform than the existing control method while providing inertial power through the control of the rectifier side of MC. In the opinion of the author, the study would be of value and interest for the future power generation system whom DGs will highly penetrate, as the modified VSG control not only can provide the frequency stability support but is dealing with the interrupted/unstable operation in the DG system due to the effect of transient disturbances. Furthermore, with the study on implementing VSG control with a complex system such as matrix converter, a new possibility for a more topologically diverse DG system will be opened up.

1.3 Conclusion

In this chapter, the background of the research in this dissertation was introduced. Main concepts, such as power converter-interfaced DG and its control strategy, were explained. As mentioned in the chapter, the VSG control has gained a lot of attention from power engineers, as it has a substantial effect on supporting the frequency stability of the power system thanks to its inertia support feature. However, there exist some significant issues and challenges that require improvement. In order to achieve that, various types of existing control schemes for power converters are discussed. Among theses, model predictive control has the characteristics that converge in a natural way to the implementation in the digital platform. The ability of FCS-MPC to achieve multiple control objectives are also very beneficial for the enhancement of VSG control capability regarding the issues discussed in

this chapter. Finally, the main research objectives of this dissertation were presented to give the readers a better understanding of the purposes of this research.

References

[1] B. Bose. "Global warming: Energy, environmental pollution, and the impact of power electronics", *IEEE Ind. Electron.* Mag., vol. 4, pp. 6-17, Mar. 2010.

[2] "Global Market Outlook For Solar Power / 2016-2020," *Solar Power Europe*.

[3] "Global Wind Report Annual Market Update 2014," *Global Wind Energy Council*.

[4] R. C. Dugan and T. E. McDermott, "Distributed generation," *IEEE Ind. Appl. Mag.*, vol. 8, no. 2, pp. 19–25, Mar./Apr. 2002.

[5] J. M. Carrasco, L. C. Franquelo, J. T. Bialasiewicz, E. Galvn, R. C. P. Guisado, M. A. M. Prats, J. I. Len, and N. Moreno-Alfonzo, "Power-electronic systems for the grid integration of renewable energy sources: A survey" *IEEE Trans. Ind. Electron*. , vol. 53, no. 4, pp. 1002-1016, Aug. 2006.

[6] D. Zhi, L. Xu, and B. W. Williams, "Improved direct power control of grid-connected DC/AC converters", *IEEE Trans. Power Electron*., vol. 24, no. 5, pp. 1280-1292, 2009.

[7] J. Alipoor, Y. Miura, T. Ise, "Power system stabilization using Virtual Synchronous Generator with Alternating Moment of Inertia" *IEEE Journal of Emerging and Selected Topics in Power Electronics* pp.(99) 1-9, 2014.

[8] J. Rocabert, A. Luna, F. Blaabjerg, and P. Rodríguez, "Control of power converters in AC microgrids," *IEEE Trans. Power Electron.*, vol. 27, no. 11, pp. 4734–4749, Nov. 2012.

[9] Q. Zhong and G. Weiss, "Static Synchronous Generators for Distributed Generation and Renewable Energy Power Systems Conference and Exposition," *PSCE '09, 2009, IEEE/PES* pp. 1-6, March 2009

[10] K. Debrabandere, B. Bolsens, J. Van den Keybus, A.Woyte, J. Driesen, and R. Belmans, "A voltage and frequency droop control method for parallel inverters," *IEEE Trans. Power Electron.*, vol. 22, no. 4, pp. 1107–1115, Jul. 2007.

[11] H. Han, Y. Liu, Y. Sun, M. Su, and J. M. Guerrero, "An improved droop control strategy for reactive power sharing in islanded microgrid," *IEEE Trans. Power Electron.*, vol. 30, no. 6, pp. 3133–3141, Jun. 2015.

[12] J. He, Y. W. Li, J. M. Guerrero, F. Blaabjerg, and J. C. Vasquez, "An islanding microgrid power sharing approach using enhanced virtual impedance control scheme," *IEEE Trans. Power Electron.*, vol. 28, no. 11, pp. 5272–5282, Nov. 2013.

[13] W. Yao, M. Chen, J. M. Guerrero, and Z.-M. Qian, "Design and analysis of the droop control method for parallel inverters considering the impact of the complex impedance on the power sharing," *IEEE Trans. Ind. Electron.*, vol. 58, no. 2, pp. 576–588, Feb. 2011.

[14] Q.-C. Zhong, "Robust droop controller for accurate proportional load sharing among inverters operated in parallel," *IEEE Trans. Ind. Electron.*, vol. 60, no. 4, pp. 1281–1290, Apr. 2013.

[15] C-.T. Lee, C-.C. Chu, and P-.T. Cheng, “A new droop control method for the autonomous operation of distributed energy resource interface converters,” *IEEE Trans. Power Electron.*, vol. 28, no. 4, pp. 1980–1993, Apr. 2013.

[16] Y. Zhu, Z. Fang, F. Wang, B. Liu, and Y. Zhao, “A wireless load sharing strategy for islanded microgrid based on feeder current sensing,” *IEEE Trans. Power Electron.*, vol. 30, no. 12, pp.6706–6719, Dec. 2015.

[17] M. B. Delghavi and A. Yazdani, “Islanded-mode control of electronically coupled distributed-resource units under unbalanced and nonlinear load conditions,” *IEEE Trans. Power Del.*, vol. 26, no. 2, pp. 661–673, Apr. 2011.

[18] J. Hu, J. Zhu, D.G. Dorrell, and J. M. Guerrero, “Virtual flux droop method — a new control strategy of inverters in microgrids,” *IEEE Trans. Power Electron.*, vol. 29, no. 9, pp. 4704–4711, Sept. 2014

[19] J. Liu, Y. Miura and T. Ise, "Comparison of Dynamic Characteristics Between Virtual Synchronous Generator and Droop Control in Inverter-Based Distributed Generators," *IEEE Transactions on Power Electronics*, vol. 31, no. 5, pp. 3600-3611, May 2016.

[20] J. Driesen and K. Visscher “Virtual synchronous generators,” in Proc. 2008 IEEE Power Energy Soc. Gen. Meeting—Convers. Del. Elect. Energy 21st Century, pp. 1–3.

[21] Q.-C. Zhong and G. Weiss, “Synchronverters: inverters that mimic synchronous generators,” *IEEE Trans. Ind. Electron*., vol. 58, no. 4, pp. 1259–1267, Apr. 2011.

[22] K. Sakimoto, Y. Miura, and T. Ise, “Stabilization of a power system including inverter type distributed generators by the virtual synchronous generator,” *IEEJ Trans. Power and Energy*, vol. 132, no. 4, pp. 341–349, Apr. 2012.

[23] S. D'Arco and J. A. Suul, "Virtual synchronous machines - Classification of implementations and analysis of equivalence to droop controllers for microgrids," *2013 IEEE Grenoble Conference*, Grenoble, 2013, pp. 1-7.

[24] Q.-C. Zhong, P.-L. Nguyen, Z. Ma, and W. Sheng, “Self-synchronized synchronverters: inverters without a dedicated synchronization unit,” *IEEE Trans. Power Electron.*, vol. 29, no. 2, pp. 617–630, Feb. 2014.

[25] M. Guan, W. Pan, J. Zhang, Q. Hao, J. Cheng, and X. Zheng, “Synchronous generator emulation control strategy for voltage source converter (VSC) stations,” *IEEE Trans. Power Syst.*, vol. 30, no. 6, pp. 3093–3101, Nov. 2015.

[26] H. Wu, X. Ruan, D. Yang, X. Chen, W. Zhao, Z. Lv, and Q.-C. Zhong, “Small-signal modeling and parameters design for virtual synchronous generators,” *IEEE Trans. Ind. Electron*., vol. 63, no. 7, pp. 4292–4303, Jul. 2016.

[27] J. Liu, Y. Miura, H. Bevrani, and T. Ise, “Enhanced virtual synchronous generator control for parallel inverters in microgrids,” *IEEE Trans. Smart Grid*, vol. 8, no. 5, pp. 2268–2277, Sep. 2017.

[28] J. Alipoor, Y. Miura, and T. Ise, "Voltage sag ride-through performance of Virtual Synchronous Generator," *2014 International Power Electronics Conference (IPEC-Hiroshima 2014 - ECCE ASIA)*, Hiroshima, 2014, pp. 3298-3305.

[29] A. D. Paquette and D. M. Divan, "Virtual Impedance Current Limiting for Inverters in Microgrids With Synchronous Generators," in *IEEE Transactions on Industry Applications*, vol. 51, no. 2, pp. 1630-1638, March-April 2015.

[30] Jose Rodriguez; Patricio Cortes, "Index in Predictive Control of Power Converters and Electrical Drives" , *IEEE*, 2012, pp.227-230

[31] G. C. Goodwin, M. M. Seron, and J. A. D. Dona, "Constrained Control and Estimation – An Optimization Perspective." Springer Verlag, 2005.

[32] H. Miranda, R. Teodorescu, P. Rodriguez, and L. Helle: "Model predictive current control for high-power grid-connected converters with output LCL filter", *Conf. of IEEE Ind. Electron*, Proc. 35th Annu, pp. 633-638, 2009.

[33] B. Arif, L. Tarisciotti, P. Zanchetta, J. C. Clare and M. Degano, "Grid Parameter Estimation Using Model Predictive Direct Power Control," *IEEE Transactions on Industry Applications*, vol. 51, no. 6, pp. 4614-4622, Nov.-Dec. 2015.

[34] J. Hu, J. Zhu, D. G. Dorrell: "Model predictive control of inverters for both islanded and grid-connected operations in renewable power generations", *IET Renewable Power Generation*, Vol. 8, Iss. 3, pp. 240-248, 2014.

[35] L. A. Serpa, S. Ponnaluri, P. M. Barbosa and J. W. Kolar, "A Modified Direct Power Control Strategy Allowing the Connection of Three-Phase Inverters to the Grid Through *LCL* -Filters," in *IEEE Transactions on Industry Applications*, vol. 43, no. 5, pp. 1388-1400, Sept.-oct. 2007.

[36] F. Donoso, A. Mora, R. Cárdenas, A. Angulo, D. Sáez, and M. Rivera, "Finite-Set Model-Predictive Control Strategies for a 3L-NPC Inverter Operating With Fixed Switching Frequency," in *IEEE Transactions on Industrial Electronics*, vol. 65, no. 5, pp. 3954-3965, May 2018.

Chapter 2
Principles of Virtual Synchronous Generator and Model Predictive Control

2.1 Introduction

Until recently, the main concerns on grid-connected RES have been with voltage and current trip limits and synchronization to the frequency of the grid. However, the growing share of DER in the electricity generation mix worldwide forces the RES-fed power generation system to adapt itself to a whole new situation in the electricity network, for instance, the system becomes vulnerable to voltage and frequency deviations due to the lack of system inertia. The use of a distributed energy storage system (DESS) with the concept of VSG control has proven to be one of the most attractive solutions for this problem. However, due to the nature of the control method, which uses the combination of output voltage and current with outer and inner control loops, proportional-integral regulators, and PWM modulators, the degree of freedom in control objectives is mostly limited. Model predictive control (MPC), on the other hand, offers advantageous over its counterpart by allowing many system variables and constraints to be included in the control targets. On top of that, the direct use of inverter states to determine system solution means a modulator can be eliminated from the control scheme. In this chapter, the principles and the design procedure of VSG and MPC control will be introduced, beginning with the principle of VSG control shown in Section 2.2. In this section, existing types of VSG control, including the basic VSG control scheme proposed by Ise Laboratory, Osaka University, are also discussed in detail. Then, the concept of MPC scheme, in general, and the FCS-MPC, from which the control methods in this dissertation are developed, will be introduced in Section 2.3 and Section 2.4, respectively.

2.2 Principles of Virtual Synchronous Generator Control

The basic concept of VSG control is to create virtual inertia in the power circuit by emulating the behavior of SGs. The well-known swing equation of SGs (2.1) is used to create rotational inertia in VSG using the relation between output power P_{out} and the input power P_{in}.

$$P_{in} - P_{out} = J\omega_m \frac{\mathrm{d}\omega_m}{\mathrm{d}t} + D(\omega_m - \omega_g), \tag{2.1}$$

where ω_g is the angular frequency of the bus, ω_m is the rotor angular frequency of a SG, J is the moment of inertia of rotating mass, and D is the damping factor of the damping power introduced by the damp winding, which depends on the power angle δ and SG impedance parameters. For the case of a round-rotor SG [1], D can be determined, as shown in (2.2).

$$D = V_{bus}^2 \left[\frac{T''_d X'_d (X'_d - X''_d)}{X''_d (X'_d + X_{line})^2} \sin^2 \delta + \frac{T''_q X'_q (X'_q - X''_q)}{X''_q (X'_q + X_{line})^2} \cos^2 \delta \right], \tag{2.2}$$

where V_{bus} is the amplitude of bus voltage, X_{line} is the line reactance, X'_d, X''_d, X'_q, X''_q are the d-axis and q-axis transient and sub-transient reactance of the SG, respectively, T''_d and T''_q are the d-axis and q-axis sub-transient short-circuit time constant of the SG, respectively. Knowing that (2.2) is only valid if mechanical losses are neglected, and the rotor flux linkage is fixed. The latter is not valid if the automatic voltage regulator (AVR) is applied. However, (2.2) can still be used to obtain an approximate value.

The shaft power of SGs is usually regulated by a governor, as described in the following equation.

$$P_{in} = P_0 - k_p(\omega_m - \omega_0) \tag{2.3}$$

where P_0 is the set value of active power, k_p is the droop coefficient, ω_0 is the nominal frequency. With (2.1), the rotational inertia is created with the injecting inertial power, which is drawn from the kinetic energy reservoir W stored in the rotating mass (2.4)

$$W = \frac{1}{2} J \omega_m^2. \tag{2.4}$$

Considering (2.1), the exchange of inertial power and the generation of the inertial response can be explained as follows. If $P_{in} > P_{out}$, ω_m increases, then W increases. This implies that the surplus generated power will be absorbed by the rotating mass in order to prevent the rise of power frequency according to *P-f* droop characteristic. On the other hand, if $P_{in} < P_{out}$, ω_m decreases, then W decreases. In this case, the inertial power from the rotating mass will be fed into the power system in order to compensate for the temporary power shortage and to oppose the reduction of power frequency.

Using the swing equation as the main idea, different types of VSG control are proposed in the literature. In this dissertation, the propose FCS-MPC-based VSG control was developed from the VSG control proposed by Ise Laboratory, which will be introduced in the following.

2.2.1 Overview of VSG Control Scheme Developed by Ise Laboratory of Osaka University

First, the VSG control developed by the research team from Ise Laboratory based on [2] will be introduced. The concept of VSG control is to emulate the characteristics of SGs. Thus It can be regulated using the well-known frequency and droop mechanism similar to the control of SGs. The mechanism of droop frequency and droop voltage is conducted according to the exchange of active and reactive powers between the SGs and the conventional grid. For instance, when the active power demanding increases, the speed of the prime mover drops. The speed regulation system of the prime mover will then increase the mechanical power. The phenomenon is recreated by the "Governor Model" block, shown in Fig. 2.1, using the mechanical frequency of rotors (ω_m) to obtain the shaft power (P_{in}) of a SG, as shown in (2.3).

Likewise, the regulation of reactive power Q flowing out of the SG can be realized by defining the voltage droop coefficient as the ratio of the required change of reactive power to the change of voltage, as done by the "Q Droop" block shown in Fig. 2.1. The $V-Q$ droop controller can be expressed as

$$Q_{ref} = Q_0 - k_q(V_{out} - E_0) \tag{2.5}$$

where E_0 is the nominal voltage, Q_{ref} is the reactive power command, Q_0 is the set value of reactive power, and k_q is the $V-Q$ droop coefficient.

As illustrated in Fig. 2.1, a PI controller is used to track the error between the output reactive power and the reference value (Q_{ref}) to obtain the output voltage amplitude command. A 20 Hz first-order low-pass filter is applied for Q_{out} in order to eliminate the ripples in measured output power. The function of this PI controller is similar to the automatic reactive power regulators (AQR) of the SG, in which the electromotive force (emf) is controlled by regulating the field current. Therefore, the output voltage amplitude command can be considered as the virtual internal emf E of the VSG.

In order to share the active and reactive power according to the ratings of DGs without communication, the droop coefficients should be designed proportionally to the capacities of each DG unit. Additionally, to resolve the problems of oscillation of active power during a disturbance and errors in reactive power-sharing as discussed in [3], two major control blocks are added into the enhanced VSG, i.e., the "stator reactance adjuster" and the "bus voltage estimator". The function of the stator reactance adjuster is to produce extra inverter output impedance to match the impedances between parallel-connected DGs in order to eliminate oscillation during a loading transition. This extra impedance will be called the "virtual impedance" of the inverter. The virtual impedance is realized by multiplication of the output current and the virtual stator inductor in the stationary frame, as shown in Fig. 2.2. The "bus voltage estimator", shown in Fig. 2.3, compensates the line voltage drop, and

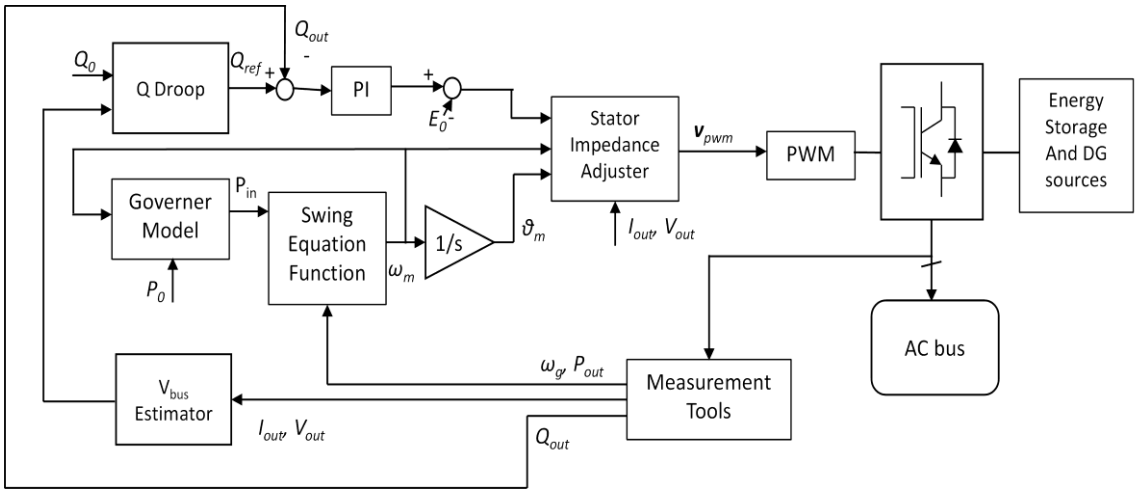

Fig. 2.1. The primary control diagram of VSG control developed by Ise laboratory

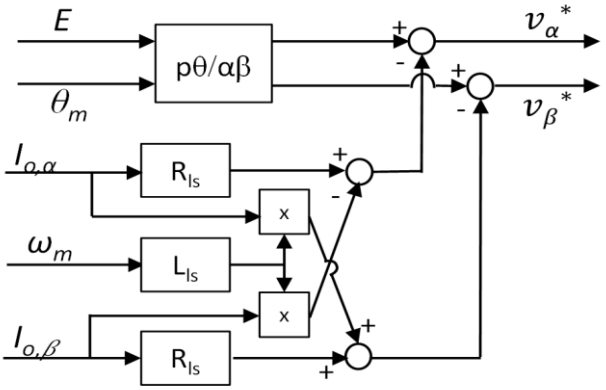

Fig. 2.2 "Stator Impedance Adjuster" block

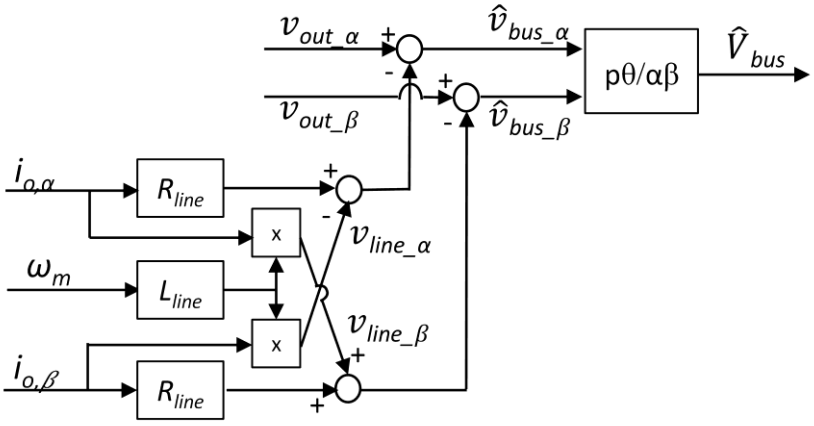

Fig. 2.3 "bus voltage estimator" block

uses the estimated bus voltage as input for the *V*-*Q* droop box in both parallel DGs to ensure proper reactive power-sharing between DGs. Finally, the output voltage of the PWM inverter V_{pwm} is obtained.

As this VSG control operates as a voltage source, it can be classified as a voltage-source-based method, it can operate independently, in a microgrid, and can be connected to the power grid directly, and no change of control is needed during operation mode transitions. Hence, VSG control can be classified as a voltage-source-based grid-forming control [4]. However, the primary VSG control developed by Ise laboratory requires a phase-locked loop (PLL) to provide the measured output frequency in order to create the damping power P_d for the block "Swing Equation", as follows.

$$P_d = D(\omega_m - \omega_g), \tag{2.6}$$

This reliance on the PLL can be removed when the pole placement method is adopted to provide an ideal damping effect without any frequency measurement, as proposed in [5]. With this method, the damping power will be determined by the measured output power and ω_m according to equation (2.7), instead of obtaining from the measured frequency ω_{PLL}, as done in (2.5).

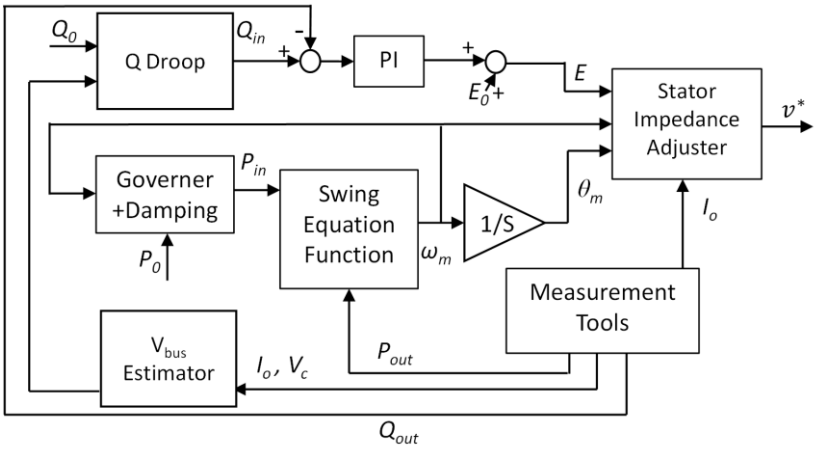

Fig. 2.4 The control diagram of VSG control with the pole placement method.

$$P_d = -k_{x\omega}(\omega_m - \omega_0) - k_{xp}P_{out} - \frac{k_{xi}}{s}P_d \tag{2.7}$$

where $k_{x\omega}$, k_{xp}, k_{xi} are the feedback gain of virtual rotor frequency, output active power, and the integral term of P_d , respectively. The tuning of these parameters is done according to [5] and will be omitted in this work. The modified control diagram of VSG control with the pole placement method is illustrated in Fig. 2.4.

2.2.2 Other Existing Types of Virtual Synchronous Generator Control

Apart from the VSG control developed by Ise Laboratory, a number of different VSG controls exist in the literature. According to [6], the VSG control schemes proposed in the literature can be categorized into three main groups based on the nature of the output reference from the VSG.

(1) Current references-based VSG control

The first group utilizes current references from VSG [7]. This method allows a quite natural implementation of high order electrical models of the SG since inverters are controlled to generate the currents that would result from a real SG. However, the control will rely on grid synchronization by a PLL and cannot operate in stand-alone mode.

Another example of the current reference-based VSG control is the one from the VSYNC project under the 6th European Research Framework program, which is the first research team trying to use virtual inertia control for inverters [10], and their control methods have been developed through [11]–[19]. It can be concluded that this control scheme is a current reference-based VSG control as a current control loop is applied at the output terminal. A PLL unit is used to detect the frequency of the grid and to provide angle reference for the *dq*-transformation.

(2) Voltage references-based VSG control

Another possible approach is to utilize the voltage references from VSG [8] - [9]. The group, which uses this approach, can be referred to as “voltage references from VSG.” Although only a reduced-order model of the SG can be applied in this approach, the utilizing voltage command allows

this VSG to function in stand-alone mode. In order to enhance the controllability, a classical cascaded control scheme of voltage and current control can also be utilized in the control methods of this group, as shown in [20]-[21]. However, to ensure stability in all operating conditions, tuning of PI has to be done appropriately, which can be challenging when a number of DGs are connected together [21].

(3) Power references-based VSG control

The last group emulates the inertia response by tracking the grid frequency without implementing any SG model [10]. The group is called “power references from VSG,” as current reference corresponding to a given power reference is used to command the DG. However, the control also relies on a PLL and cannot operate independently.

In this dissertation, the approach with voltage references from VSG is preferred, as the reduced-order model of SG was proved to be enough to provide the frequency support to the grid [3] and smooth transition between grid-connected and islanded modes is ensured in DG controlled by voltage references-based VSG control.

2.3 Model Predictive Control for Power Electronics

The born of predictive control can be traced back to the 1960s when the author of [22] presented the idea of precalculation of the plant’s behavior via mathematical model and used these values to determine optimum actuating variables. After the introduction of the idea, it had to wait for almost 20 years until interest in this field started to surge. The first-ever considered predictive control scheme was proposed in 1979 under the name "Dynamic Matrix Control" (DMC) [23]. DMC was conceived to tackle the multi-variable constrained control problems for the oil and chemical industry. In 1987, an alternative concept of the predictive controller, known as Generalized Predictive Control (GPC), was introduced by [24]. While the original DMC formula was completely deterministic and did not include any explicit disturbance model, GPC was developed more to the stochastic aspect. The GPC approach is traditionally not suitable for multi-variable constrained systems, which are commonly encountered in power electronics and drive systems. Thus an extension is required when GPC is to be used for multi-dimension systems, which adds up complexity to the control scheme. For this reason, DMC has more impact on industry compare to its counterpart [25]. The initial research on Model Predictive Control (MPC) is also characterized by an attempt to understand the operation of DMC. Predictive control was first proposed for the control of electrical drives and power converter in the 1980s. Holtz published a predictive method to control the armature current of the DC machine fed by the line-commutated converter [26] and a predictive controller for the current of AC-machine [27]. After 1990, many publications on the topic were released. Nevertheless, they are mostly enhancement or a combination of one another. Categorized by operation principle, they can be broadly grouped into trajectory-based, hysteresis-based, and model-based predictive control. Well-known control schemes such as Direct Self Control (DSC) and Direct Mean Torque Control (DTMC) belong to the trajectory-based method, while Direct Torque Control (DTC) or Direct Power

Control (DPC) could be seen as a hysteresis-based predictive controller. The concepts of trajectory-based and hysteresis-based methods are very similar. One is an attempt to force the system into a predefined trajectory, while the other tries to keep the value of the control parameter within a tolerance band. Model-based predictive control, on the contrary, uses an entirely different concept. Unlike the hysteresis- and trajectory-based method, which uses only the current system state, to predict the future controlled value of the system, MPC takes both the past and the actual values into account. According to the predefined cost function, optimal actuating variables can be determined under the consideration of multiple controlled variables and constraints.

The principle of model predictive control was introduced for industrial control applications in the 1970s after the first ideas of this strategy have already been published in 1960 by Emeljanov. Traditionally, this method had been mainly used in a slow process industry such as chemical plants and oil refineries due to its high computation demand. MPC does not denote a particular control algorithm, but rather a whole family of controller types. The common characteristic of all these controllers is the principle of determining an optimum value for the actuating variable by using an explicit model of the system. The basic structure of MPC can be summarized as follows [28]:

(1) Predict the future behavior of the process state/output with a system model.
(2) Compute the future input signals on line at each step by minimizing a cost function under inequality constraints on the manipulated (control) and/or controlled variables.
(3) Apply on the controlled plant only the first of the vector control variable and repeat the previous step with new measured input/state/output variables.

In the area of electrical drive and power converter, due to its high sampling frequency, an intuitive approach to reducing the computational load for solving optimal control problems is required, for instance, by using a fixed number of iterations in each sampling step. This is possible in power converter-based system due to the discrete nature of power converters, which means the number of actuation of the system is limited to the number of possible switching states of the converter. Alternatively, the computational load can be reduced by using the previous solution for a warm-start of the optimization algorithm in order to successively reduce the suboptimality of the predicted trajectories.

Apart from GPC, model-based predictive control can be separated, according to [29], at least into three classes:

(1) Finite control set model predictive control (FCS-MPC): FCS-MPC takes advantage of the inherent features of the converter, which can only produce eight different switching states by turning on and off the gates for each leg of the converter. This control approach uses the converter switching states as control variables directly. Thus it is also known as direct model predictive control. The introduction of this kind of control approach in the field of power converters control was first done by [30]. Thereafter, there has been a number of works, which present such control schemes for various power converters and drives.
(2) Two-configuration Predictive Control (2PC): 2PC consists of applying successively two configurations of the power converter during a computation step; one of these configura-

tions leads to null voltages. The principle of such a control scheme reads as follows. In the first step, the future values of load currents are calculated, assuming that null voltages are applied during the whole next sampling period (the free response). Then, an active state of the converter is selected and the response based on this state, for instance, the values that the controlled values would reach if this converter configuration were applied for the whole sampling period will be computed (the force response). Finally, from these calculated values, one can acquire the time in which the null voltage and active configuration should be applied in one period so that the actual actuating values are as close as possible to the desired values. There are a number of variations of this approach, but the concept is always as described. The works based on this method are, for example, [31].

(3) PWM Model Predictive Control (PPC): The third class of the predictive control approach calculates the voltages required to reach the desired point after one period and remains there. Then, a pulse-width modulation (PWM) is used to translate these desired voltages into switching orders. This method is also noted as "dead-beat control" by some works. PPC operates with six configurations per sampling period. Hence, the required actuating values could be precisely reached. The works, which are occupied with this method, have been presented in [32].

Furthermore, a number of novel MPC strategies are proposed in the literature, which combines the concepts of the three classes of MPC mentioned previously, such as "continuous control set MPC" or "modulated MPC" [38], [39]. Although these methods offer clear advantages over FCS-MPC, for instance, the reduction in ripple and a fixed switching frequency, similar to 2PC and PPC MPC, the tuning of cost function's weighting parameters of such methods are a lot more complicated than FCS-MPC when multiple variables are considered in the controllers. Hence, FCS-MPC is viewed as an optimal solution for improving VSG controls in this work.

2.4 Finite Control Set Model Predictive Control

2.4.1 Principle and System Model

The basic ideas of FCS-MPC are based on the use of a system model to predict the future behavior of the system variable. The system model is a discrete-time model which can be expressed in the state-space model form:

$$\boldsymbol{x}(k+1) = \boldsymbol{A}\boldsymbol{x}(k) + \boldsymbol{B}\boldsymbol{u}(k) \tag{2.8}$$

$$\boldsymbol{y}(k) = \boldsymbol{C}\boldsymbol{x}(k) + \boldsymbol{D}\boldsymbol{u}(k) \tag{2.9}$$

The optimal actuation will be selected among these predictions based on a predefined cost function that represents the desired behavior of the system. The cost function is a function of the references, future states, and the future actuation, which can be defined with the following equation.

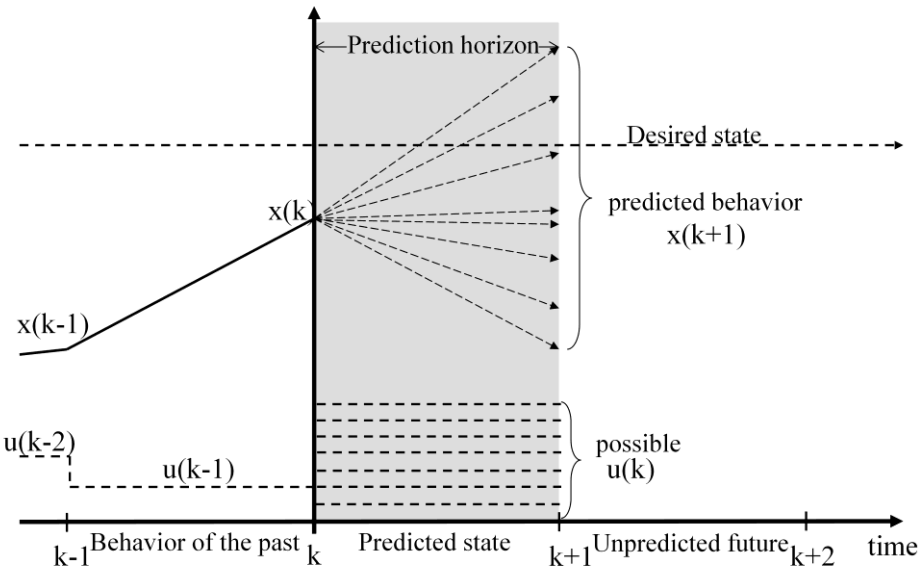

Fig. 2.5 Functional Principle of FCS-MPC

$$J(k) = f(\boldsymbol{x}(k+1), \boldsymbol{u}(k)) \tag{2.10}$$

In other words, MPC is an optimization problem that consists of minimizing the cost function J. For each sampling instant, the controller will employ the optimal actuator in the converter. Then at the next sampling instant, the new measured data will be utilized to obtain a new optimal actuation. This is called a receding horizon strategy. Giving the fact that the number of actuators (switching states that a converter can switch into) is finite, the number of forecasts that need to be made is limited to this number, and thus, the algorithm is called finite control set MPC. The working principle of FCS-MPC can be summarized in Fig 2.5.

In order to design FCS-MPC, the discrete-time models of the systems, and the modeling of the power converters with consideration of its possible switching states need to be obtained. The former models differ for different topologies and applications, and thus, they will be discussed along with the systems under study in chapter 3 and chapter 5. The latter, on the other hand, depends on the types of converters alone. The fundamental elements of power converters are the semiconductor switches, which can be simplified as an ideal switch with only on and off states. Hence, the total number of switching states of a power converter is equal to the number of possible combination of states of each switch, which can be described with $N = x^y$, when x is the number of possible states of each leg of the converter, and y is the number of legs of the converter. Nevertheless, the states that result in undesired system conditions such as short-circuits must be removed from the set of possible switching stats. Utilizing the corresponding voltage or current, which is produced by each of the possible switching states and the system model, a prediction for the future system behavior can be conducted. In order to give a clearer understanding of this topic, examples of modeling of voltage and current source inverter will be discussed in the next subsection.

(1) Example of Voltage Source Converter

The circuit configuration of a three-phase voltage source converter is shown in Fig. 2.6. As seen in the figure, either one of the power switches of each leg of a converter (for instance either S_1 or S_4) is allowed to turn on at any time to prevent the short circuit from occurring to the DC-link. Thus, taking into account that the number of possible states of each leg of the converter is 2 and the number of legs is 3, the converter can generate 2^3 equal to eight possible different switching states as listed in Table 2.1, where the switching signal S_a, S_b and S_c can be defined with equation (2.11)

$$S_{abc} = \begin{cases} 1 \text{ if an upper switch on and a lower switch off} \\ 0 \text{ if an upper switch off and a lower switch on} \end{cases} \tag{2.11}$$

The converter voltage corresponding to these switching signals is determined by Clarke's transformation.

$$\boldsymbol{v}_{\alpha\beta} = \frac{2}{3}\begin{bmatrix} 1 & -\frac{1}{2} & -\frac{1}{2} \\ 0 & \frac{\sqrt{3}}{2} & -\frac{\sqrt{3}}{2} \end{bmatrix}\begin{bmatrix} v_{an} \\ v_{bn} \\ v_{cn} \end{bmatrix} \tag{2.12}$$

$$\boldsymbol{v}_{\alpha\beta} = \frac{2}{3}\begin{bmatrix} v_{an} - \frac{v_{bn}}{2} - \frac{v_{cn}}{2} \\ \frac{\sqrt{3}}{2}v_{bn} - \frac{\sqrt{3}}{2}v_{cn} \end{bmatrix} \tag{2.13}$$

Considering Fig. 2.7, it can be concluded that if we converse the values of v_{aN}, v_{bN}, and v_{cN} and v_{an}, v_{bn}, and v_{cn} with Clarke's transformation, their values in $\alpha\beta$-frame are actually equivalent. Hence equation (2.13) can be written as follows.

$$\boldsymbol{v}_{\alpha\beta} = \frac{2}{3}\begin{bmatrix} S_a V_{dc} - \frac{S_b V_{dc}}{2} - \frac{S_c V_{dc}}{2} \\ \frac{\sqrt{3}}{2}S_b V_{dc} - \frac{\sqrt{3}}{2}S_c V_{dc} \end{bmatrix} \tag{2.14}$$

when V_{dc} is the dc-link voltage and v_{aN}, v_{bN} and v_{cN} are the phase-to-neutral voltage and can be described as a function (2.15) of S_a, S_b and S_c.

TABLE 2.1 Switching States and Voltage Vectors

S_a	S_b	S_c	Voltage Vectors
0	0	0	V_0
1	0	0	V_1
1	1	0	V_2
0	1	0	V_3
0	1	1	V_4
0	0	1	V_5
1	0	1	V_6
1	1	1	V_7

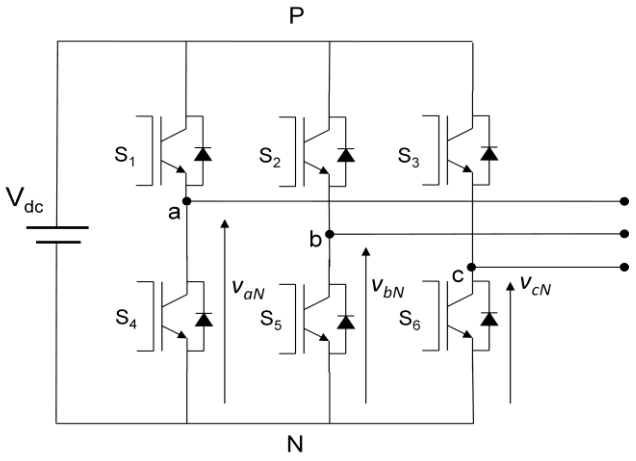

Fig. 2.6 Three-phase Voltage Source Converter

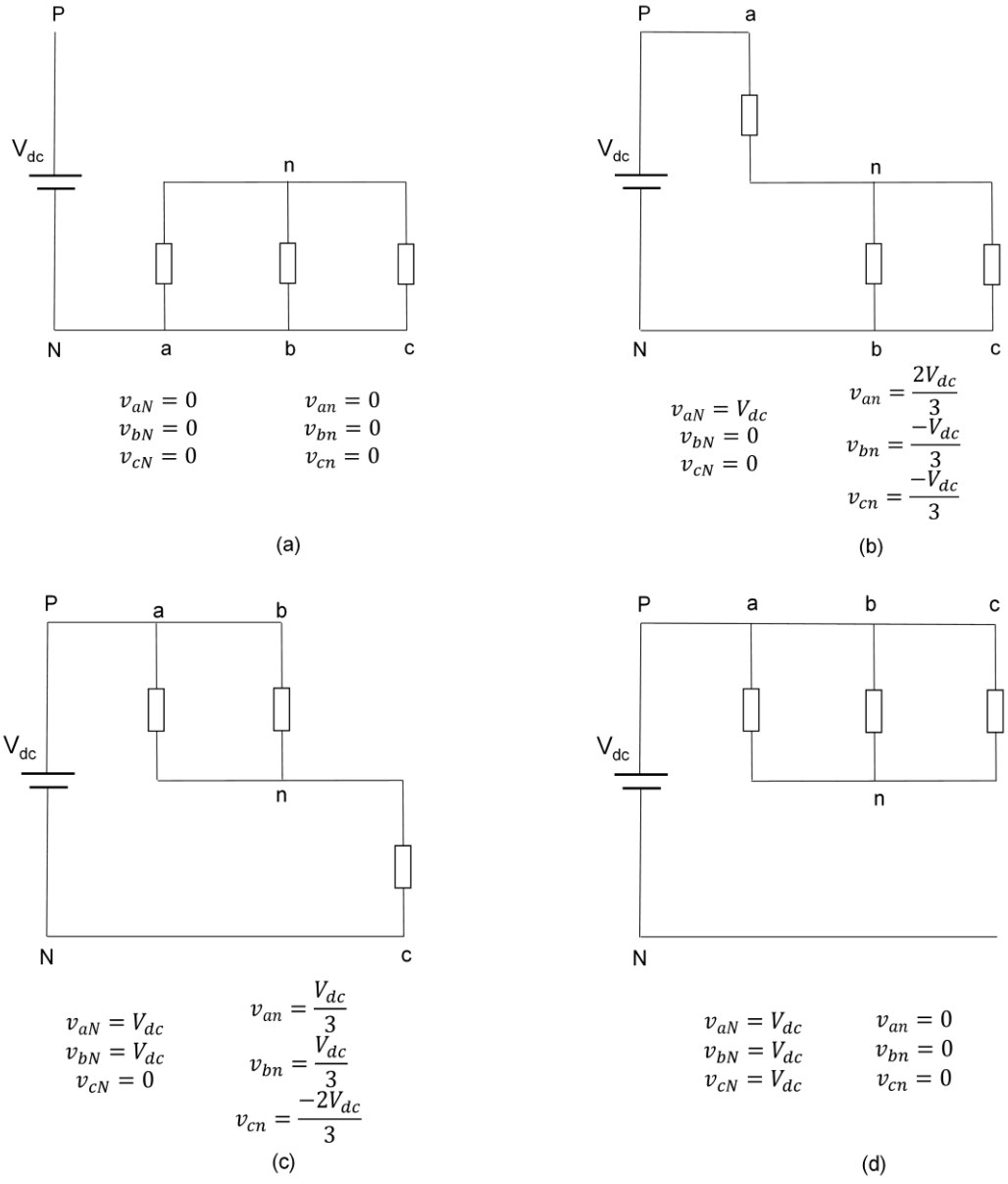

Fig. 2.7 Equivalent load configuration

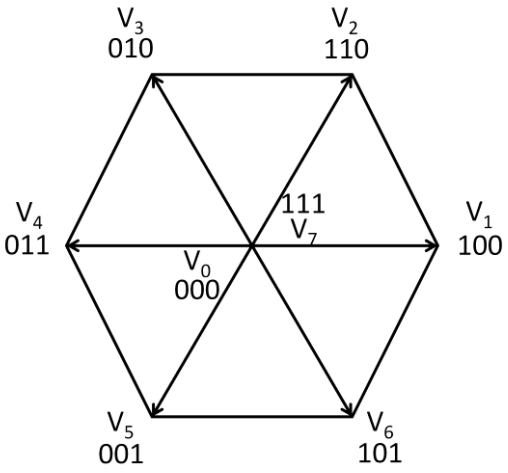

Fig. 2.8 Space Voltage Vectors Representation

$$\begin{aligned} v_{aN} &= S_a V_{dc} \\ v_{bN} &= S_b V_{dc} \\ v_{cN} &= S_c V_{dc} \end{aligned} \tag{2.15}$$

Considering the configuration in Fig. 2.6, equation (2.12), and the possible switching states in Table 2.1, using Clarke's transformation, the converter voltage (v_{vs}) in αβ-coordination for each switching state can be determined with equation (2.16).

$$\boldsymbol{v}_{vs,\alpha\beta} = \frac{2}{3}(v_{aN} + a v_{bN} + a^2 v_{cN}) \tag{2.16}$$

where a is the unitary vector, which represents the 120^{o} phase displacement between the phase. Therefore, the converter voltage produced by the eight possible switching states of the converter can be represented in αβ-coordination with space voltage vector V_0–V_7, as shown in Figure 2.8. This representation is known as space vector representation, where $\{V_1, V_2, V_3, V_4, V_5, V_6\}$ represent six active switching states of the rectifier, while V_0 and V_7 indicate the cases when all three upper power transistor switches are all turned on, or all turned off, which causes a short circuit in three legs

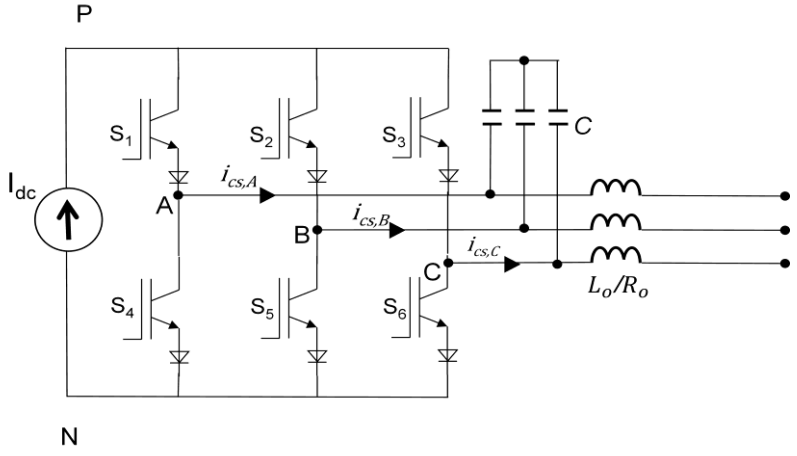

Fig. 2.9 Three-phase Current Source Converter

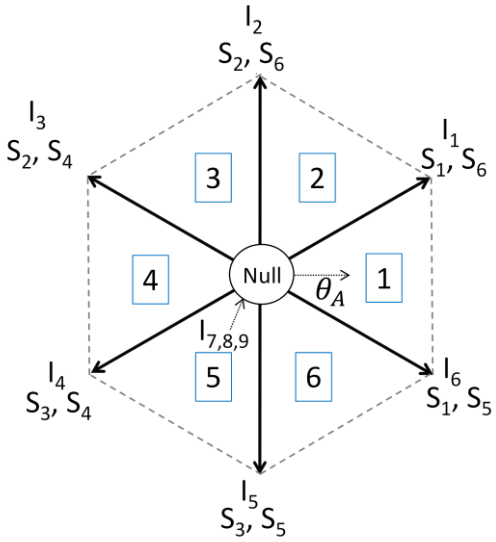

Fig. 2.10 Space Current Vectors Representation

of the converter. Hence, these two voltage vectors are called zero voltage vectors. Each of these voltage vectors will be used as input actuators for the prediction of MPC.

(1) Example of Current Source Converter

The circuit configuration of a three-phase current source converter is shown in Fig. 2.9. Similar to the case of voltage source converter, the number of possible switching states that the converter can generate is limited, as concluded in Table 2.2. For active vectors denoted as $I_1 - I_6$, the current source converter uses six unidirectional switches in two converter's legs: one in the upper part (switches 1, 2, 3) and second in the lower part of the bridge (switches 4, 5, 6). The switches are chosen in such a way, as concluded in Table 2.2. Three passive vectors (zero vectors) are denoted as $I_7 - I_9$. In this case, both upper and lower switches of one of the three converter's legs are turned on

TABLE 2.2 Switching States and Current Vectors

ON SWITCHES	i_A	i_B	i_C	U_{PN}	Current Vectors
S_1, S_6	I_{dc}	0	$-I_{dc}$	V_{AC}	I_1
S_2, S_6	0	I_{dc}	$-I_{dc}$	V_{BC}	I_2
S_2, S_4	$-I_{dc}$	I_{dc}	0	V_{BA}	I_3
S_3, S_4	$-I_{dc}$	0	I_{dc}	V_{CA}	I_4
S_3, S_5	0	$-I_{dc}$	I_{dc}	V_{CB}	I_5
S_1, S_5	I_{dc}	$-I_{dc}$	0	V_{AB}	I_6
S_1, S_4	0	0	0	0	I_7
S_2, S_5	0	0	0	0	I_8
S_3, S_6	0	0	0	0	I_9

at the same time. The generated current $I_1 - I_9$ can be displayed in space current vectors representation, as illustrated in Fig. 2.10. The converter current (i_{cs}) in αβ-coordination for each switching state can be determined with equation (2.17).

$$\boldsymbol{i}_{cs,\alpha\beta} = \frac{2}{3}\begin{bmatrix} 1 & -\frac{1}{2} & -\frac{1}{2} \\ 0 & \frac{\sqrt{3}}{2} & -\frac{\sqrt{3}}{2} \end{bmatrix}\begin{bmatrix} i_A \\ i_B \\ i_C \end{bmatrix} \tag{2.17}$$

Therefore, each of the converter current produced by the nine possible switching states of the current source converter can be used as input actuators for the prediction of MPC.

2.4.2 Types of Cost Function

A cost function is a tool to analyze performance or to define the operating range of the controller. It allows multiple control objectives to be considered at the same time, which is a unique advantage of MPC. This cost function may consist of several types of control terms. The most common terms that can be included in a cost function will be introduced as follows:

(1) Reference following

The most common expressions in a cost function are the ones that represent references following. These terms can be expressed generally as the error between the predicted value and its reference, as can be seen in the following equation.

$$g_1 = (\boldsymbol{x}^* - \boldsymbol{x}(k+1))^2 \tag{2.18}$$

where g_1 is reference following cost function, $\boldsymbol{x}^*$ is the reference value and $\boldsymbol{x}(k+1)$ is the predicted value. An absolute error can be used instead of a squared error. However, when two or more different terms are included in the cost function, a squared error represents a better reference following. Alternatively, an integral value of error for one sampling period is also a promising choice, as cost function considers the trajectory of the variable between the instant *k* and the instant *k+1*, which leads to more accurate reference tracking. A reference following cost function can be used alone or together with other types of control terms.

(2) Actuation constraints

The actuation constraint is a term that represents the control effort of a power converter, which is related to the voltage or current variations, the switching frequency, or the switching losses. For example, if one wants to minimize the magnitude of the difference between the previously applied voltage vector *v(k-1)* and the voltage vector to be applied *v(k)*, the actuation constraints are often used together with the reference following cost function as shown in the following cost function.

$$g_2 = g_1 + \lambda_2 \| v(k-1) - v(k) \| \tag{2.19}$$

where g_2 is the actuation constraints and λ_2 is a weighting factor that allows the importance of control effort to be adjusted.

(3) Hard constraints

Although model predictive control can achieve direct control of output variables without the need for inner control loops, the uncontrolled internal variables can reach values that are outside their allowed range. In order to prevent this from happening, limitations can be included as an additional term in the cost function. For example, a hard constraint to ensure that DC-voltage is always positive can be defined as follows.

$$g_3 = \begin{cases} 10^8, & u_{DC}(k+1) < 0 \\ 0, & u_{DC}(k+1) \geq 0 \end{cases} \tag{2.20}$$

where g_2 is the actuation constraints. The hard constraint is also customarily used together with the reference following cost function

2.4.3 Weighting Factor Design

Although no weighting factors are necessary for the cost function when only one type of variable is controlled, to fully utilize the advantage of MPC, multiple objectives control is preferable. This can be done simply by introducing the additional control terms in the cost function. However, as the number of terms in the cost function increases, the adjustment of the weight parameters is not a straightforward task, especially when they are of a different nature. Each additional term in the cost function has a specific weighting factor, which is used to tune the importance of that term related in relation to the other control targets. These parameters have to be appropriately designed in order to achieve the desired performance. This problem is still an open topic in literature. Different solutions have been thoroughly analyzed, and several approaches have been proposed [33]–[37]. Among these, [33] offers basic guidelines to reduce the uncertainty and improve the effectiveness of the tuning stage are presented in this section, depending on the nature of the different terms involved in the formulation of the cost function.

(1) Cost function with a second (less important) term

According to [33], this is the easiest case for weighting factor adjustment since the system can be first controlled using only the primary control objective or term. This can be very simply achieved by neglecting the secondary terms forcing the weighting factor to zero, $\lambda_2 = 0$. Hence the main idea of the tuning procedure is to convert the cost function with a second term into a cost function without weighting factors. Then, in order to establish the tradeoff between the first term and the second term, it is necessary to establish measurements or figures of merit that will be used to evaluate the quality achieved by adjusting the weighting factor. Once the measures are defined, evaluate the system behavior with simulations starting with $\lambda_2 = 0$ and increase the value gradually. Record the corresponding measures for each value of λ_2. Stop the increments of λ_2, once the measured value for the second term has reached the desired value for the specific application, or keep increasing, until the primary variable is not controlled properly. Then plot the results and select values of the system that fulfill the requirements for both variables.

(2) Cost functions with equally important terms

According to [33], a difficulty in this kind of weighing gains tuning is the different nature of the variables. For example, when controlling torque and flux in an adjustable speed drive application with a nominal torque and flux of 25[Nm] and 1[Wb] respectively, the torque error can have different orders of magnitudes making both variables not equally important in the cost function, affecting the system performance. Thus the first step is to normalize the cost function. Once normalized, all the terms will be equally important, and now, $\lambda_2 = 1$ can be considered as a starting point since the second term is as important as the first term in this control system, thus $\lambda_2 = 0$ is not allowed. Usually, a suitable λ_2, is closely located to 1. The second step is the same as with the previous procedure, i.e., measurements or figures of merit have to be defined, and they will be used to evaluate the quality achieved by the weighting factor. The last step is to perform the branch and bound algorithm. When a small interval of weighting factors has been reached, meaning by a small interval, that there are no significant differences in the measures between the upper and lower bounds of the interval, then the weighting factor has been obtained. More explanation regarding this tuning method can be found in [33].

2.5 Conclusion

In this chapter, the principles and types of VSG, including the one that is developed by the research team of Osaka University, are introduced. Then, the brief introduction to MPC control for power electronics applications is presented. Besides, this chapter focusses on one of the predictive control methods that belonged to the MPC family, namely the FCS-MPC, since it is selected as the primary control algorithm in this dissertation. As seen in section 2.4, the principle of FCS-MPC, the examples of how to obtain system model from voltage and current sources converters, along with the guideline of how to design the weighing parameters, are presented in detail.

References

[1] J. Machowski, J. Bialek, and J. R. Bumby, *Power System Dynamics and Stability*. New York: John Wiley & Sons, 1997, pp. 141–182.

[2] T. Shintai, Y. Miura, and T. Ise, “Reactive power control for load sharing with virtual synchronous generator control,” in *Proc. 7th Int. Power Electron. Motion Control Conf.*, 2012, pp. 846–853.

[3] J. Liu, Y. Miura, H. Bevrani, T. Ise, "Enhanced virtual synchronous generator control for parallel inverters in microgrids", *IEEE Transactions on Smart Grid,* vol. 8, no. 5, pp. 2268-2277, Sept. 2017.

[4] J. Rocabert, A. Luna, F. Blaabjerg, and P. Rodriguez, “Control of power converters in AC microgrids”, *IEEE Transaction on Power Electron*, vol. 27, no. 11, pp. 4734–4749, Nov. 2012.

[5] J. Liu, Y. Miura, and T. Ise, “Fixed-parameter damping methods of virtual synchronous generator control using state feedback,” *IEEE Access*, vol. 7, pp. 99177–99190, 2019.

[6] S. D'Arco and J. A. Suul, "Virtual synchronous machines - Classification of implementations and analysis of equivalence to droop controllers for microgrids," *2013 IEEE Grenoble Conference*, Grenoble, 2013, pp. 1-7.

[7] C. Pelczar, "*Mobile Virtual Synchronous Machine for Vehicle-to-Grid Applications*," Dr. Eng. Dissertation, Clausthal University of Technology, Clausthal-Zellerfeld, Germany, March 2012.

[8] S. M. Ashabani, Y. A.-R. I. Mohammed, "A Flexible Control Strategy for Grid-Connected and Islanded Microgrids With Enhanced Stability Using Nonlinear Microgrid Stabilizer," *IEEE Transactions on Smart Grid*, Vol. 3, No. 3, pp. 1291-130 , September 2012.

[9] H. Alatrash, A. Mensah, E. Mark, G. Haddad, J. Enslin, "Generator Emulation Controls for Photovoltaic Inverters," *IEEE Transactions on Smart Grid*, vol 3, no. 2, pp. 996-1011, June 2012.

[10] J. Driesen and K. Visscher "Virtual synchronous generators," *in Proc. 2008 IEEE Power Energy Soc. Gen. Meeting—Convers. Del. Elect. Energy 21st Century*, pp. 1–3.

[11] K. Visscher and S. W. H. de Haan, "Virtual synchronous machines (VSG's) for frequency stabilisation in future grids with a significant share of decentralized generation," in *Proc. IET-CIRED Seminar SmartGrids for Distribution*, 2008, pp. 1–4.

[12] M.P.N. van Wesenbeeck, S.W.H. de Haan, P. Varela, and K. Visscher, "Grid tied converter with virtual kinetic storage," in *Proc. IEEE Bucharest PowerTech*, 2009, pp.1–7.

[13] T. Loix, S. de Breucker, P. Vanassche, J. van den Keybus, J. Driesen, and K. Visscher, "Layout and performance of the power electronic converter platform for the VSYNC project," in *Proc. IEEE Bucharest PowerTech*, 2009, pp. 1–8.

[14] M. Albu, K. Visscher, D. Creanga, A. Nechifor, and N. Golovanov, "Storage selection for DG applications containing virtual synchronous generators," in *Proc. IEEE Bucharest PowerTech*, 2009, pp.1–6.

[15] T. Vu Van, A. Woyte, M. Albu, M. van Hest, J. Bozelie, J. Diaz, T. Loix, D. Stanculescu, and K. Visscher, "Virtual synchronous generator: Laboratory scale results and field demonstration," in *Proc. IEEE Bucharest PowerTech*, 2009, pp.1–6.

[16] M. Albu, J. Diaz, V. Thong, R. Neurohr, D. Federenciuc, M. Popa, and M. Calin, "Measurement and remote monitoring for virtual synchronous generator design," in *Proc. IEEE Int. Workshop Appl. Measurements for Power Syst.*, 2010, pp.7–11.

[17] V. Karapanos, Z. Yuan, and S. W. H. de Haan, "SOC maintenance and coordination of multiple VSG units for grid support and transient stability," presented at the 3rd VSYNC workshop, Cheia, Romania, 2010. [Online]. Available: http://www.vsync.eu/fileadmin/vsync/user/docs/ Workshop3/Karapanos.pdf

[18] M. Albu, M. Calin, D. Federenciuc, and J. Diaz, "The measurement layer of the Virtual Synchronous Generator operation in the field test," in *Proc. IEEE Int. Workshop Appl. Measurements for Power Syst.*, 2011, pp.85–89.

[19] V. Karapanos, S. W. H. de Haan, and K. H. Zwetsloot, “Testing a virtual synchronous generator in a real time simulated power system,” in *Proc. Int. Conf. Power Syst. Transients*, 2011.

[20] A. Perera, "Virtual Synchronous Machine-based Power Control in Active Rectifiers for Micro Grids," MSc. Thesis, Norwegian University of Science and Technology, Trondheim, Norway, July 2012

[21] S. D'Arco, J. A. Suul, and O. B. Fosso, "Automatic Tuning of Cascaded Controllers for Power Converters Using Eigenvalue Parametric Sensitivities," *IEEE Transactions on Industry Applications*, vol. 51, no. 2, pp. 1743-1753, March-April 2015.

[22] S. V. Emeljanov, *Automatische Regelsysteme mit veraenderlicher Struktul*, R. Oldenbourg Verlag, Munich, Germany, 1969.

[23] C. R. Cutler, B. L. Remaker, *Dynamic Matrix Control: A Computer Control Algorithm,* AIChE 86th, National Meeting, Houston, 1979.

[24] D.W. Clarke, C. Mohtadi, P.S. Tuffs, “Generalized predictive control—Part I. The basic algorithm”, *Automatica,* vol. 23, Issue 2, 1987, pp. 137-148.

[25] J. Brian Froisy, “Model predictive control: Past, present, and future”, *ISA Transactions*, vol. 33, Issue 3, 1994, pp. 235-243.

[26] J. Hpltz and U. Schwellenberg, "A New Fast-Response Current Control Scheme for Line-Controlled Converters," *IEEE Transactions on Industry Applications*, vol. IA-19, no. 4, pp. 579-585, July 1983.

[27] J. Holtz and S. Stadtfeld, “A predictive controller for the stator current vector of ac machines fed from a switched voltage source,” in *Proc. Int. Power Electron. Conf*., Tokyo, 1983, pp. 1665–1675.

[28] T. Zheng, “Model Predictive Control”, *Sciyo*, Chapters published August 18, 2010, under CC BY-NC-SA 3.0 license. www.intechopen.com/books/model-predictive-control

[29] F. Morel, X. Lin-Shi, J. Retif, B. Allard and C. Buttay, "A Comparative Study of Predictive Current Control Schemes for a Permanent-Magnet Synchronous Machine Drive," in *IEEE Transactions on Industrial Electronics*, vol. 56, no. 7, pp. 2715-2728, July 2009.

[30] J. Rodriguez, J. Pontt, C. Silva, M. Salgado, S. Rees, U. Ammann, P. Lezana, R. Huerta, and P. Cortes, “Predictive control of three-phase inverter,” *Electron. Lett*., vol. 40, no. 9, pp. 561–563, Apr. 29, 2004

[31] M. Pacas and J. Weber, "Predictive direct torque control for the PM-synchronous machine," *IECON'03. 29th Annual Conference of the IEEE Industrial Electronics Society* (IEEE Cat. No.03CH37468), Roanoke, VA, USA, 2003, pp. 1249-1254 Vol.2.

[32] P. Correa, M. Pacas, and J. Rodriguez, "Predictive Torque Control for Inverter-Fed Induction Machines," *IEEE Transactions on Industrial Electronics*, vol. 54, no. 2, pp. 1073-1079, April 2007.

[33] P. Cortes et al., “Guidelines for weighting factors design in model predictive control of power converters and drives,” *in Proc. IEEE ICIT*, 2009, pp. 1–7.

[34] P. Zanchetta, “Heuristic multi-objective optimization for cost function weights selection in finite states model predictive control,” *in Proc. IEEE PRECEDE*, 2011, pp. 70–75.

[35] F. Villarroel et al., “Multiobjective switching state selector for finite states model predictive control based on fuzzy decision making in a matrix converter,” *IEEE Trans. Ind. Electron*., vol. 60, no. 2, pp. 589–599, Feb. 2013.

[36] C. A. Rojas et al., “Predictive torque and flux control without weighting factors*,” IEEE Trans. Ind. Electron*., vol. 60, no. 2, pp. 681–690, Feb. 2013.

[37] S. Alireza Davari, D. A. Khaburi, and R. Kennel, “An improved FCS-MPC algorithm for an induction motor with an imposed optimized weighting factor,” *IEEE Trans. Power Electron*., vol. 27, no. 3, pp. 1540–1551, Mar. 2012.

[38] A. A. Ahmed, B. K. Koh, and Y. I. Lee, "A Comparison of Finite Control Set and Continuous Control Set Model Predictive Control Schemes for Speed Control of Induction Motors," *IEEE Transactions on Industrial Informatics*, vol. 14, no. 4, pp. 1334-1346, April 2018.

[39] F. Donoso, A. Mora, R. Cárdenas, A. Angulo, D. Sáez, and M. Rivera, "Finite-Set Model-Predictive Control Strategies for a 3L-NPC Inverter Operating With Fixed Switching Frequency," *IEEE Transactions on Industrial Electronics*, vol. 65, no. 5, pp. 3954-3965, May 2018.

Chapter 3
Implementation of FCS-MPC-Based VSG Control for Inverter-Interfaced DGs

3.1 Introduction

The results of the past research works have clearly demonstrated that the VSG-based DGs can contribute to the creation of inertia and damping effect and solve issues related to frequency deviations [1]-[7]. Moreover, VSG control can be integrated with droop characteristics. Thus, such VSG control inherits the advantages of droop control [8], for instance, proper load sharing among parallel-connected DGs, and smooth transition between grid-connected and islanded modes [9]. Still, with the growing importance of DGs, it is beneficial to study the control concept of VSG under various conditions, for instance, power quality and fault management, as it is very well-known that inverter current should be limited during short-circuit faults and overload conditions. Otherwise, semiconductor switches can be damaged because of their low thermal inertia [10]–[11]. Since VSI-based DGs are usually used in a voltage-controlled mode, where voltage and frequency are regulated at the DG terminal, they often lack the capability to limit current. Although a multiloop control structure regulating current and voltage can be utilized, the cascade structure of the multiloop control often leads to a slow dynamic response of the controller. This is a limiting factor for overcurrent limiting function, which should act immediately right after disturbances occur in order to prevent the overcurrent from damaging any sensitive devices in the DG system.

In recent years, finite control set model predictive control (FCS-MPC) has been presented as an attractive alternative for the control of power converters because it has a flexible control scheme that allows easy inclusion of multiple control variables, system constraints, and nonlinearities. Previously, some control solutions based on FCS-MPC for DGs appeared in the literature; for instance, FCS-MPC strategies for a grid-connected operation are proposed in [12]-[16]. Conclusively, several benefits of the MPC scheme can be observed, including being simple to apply in multivariable systems, the possible inclusion of constraints, straightforward control law, and fast dynamic response. Among these, the effective multiple-input-multiple-output (MIMO) control of FCS-MPC and the fast dynamic response are highly attractive for achieving overcurrent prevention ability. The multivariable system of the controller allows the inclusion of both voltage and current control into a single control loop. This grants the controller with the ability to limit overcurrent without a transition between normal and overcurrent mode. The fast dynamic response of FCS-MPC can also be considered the main advantage over other PWM-based methods. Additionally, the existence of voltage

outer loop control in αβ-axis can assist in dealing with nonlinearity and distortion in current and voltage waveform under the effect of transient disturbance [17].

3.2 The Proposed FCS-MPC-Based VSG Control

3.2.1 Overview

The overall control diagram of the proposed control is shown in Fig. 3.1. It is composed of the FCS-MPC, the VSG control, and the current command parts. The FCS-MPC uses a mathematic model of the system to predict the system variables and to evaluate the optimal switching states for VSI. The FCS-MPC part will be explained in subsection 3.2.2, whereas the VSG control with the pole place method part is adopted from [18], as already discussed in subsection 2.2.1. In this part, the voltage command variables of the VSG are determined. In order to accomplish the FCS-MPC scheme with both voltage and current control, a current command need to be provided. This command is generated from the current command part, as explained in subsection 3.2.3.

3.2.1 System Model

The model of the system with the inverter side inductor and filter capacitor of a *LCL* filter depicted in Fig. 3.2 is utilized to forecast the voltage and current output of the system. This model can be described in $\alpha\beta$-frame with capacitor dynamics equation (3.1) and inductance dynamics equation (3.2).

$$C\frac{d\boldsymbol{v}_c}{dt} = \boldsymbol{i}_f - \boldsymbol{i}_o \tag{3.1}$$

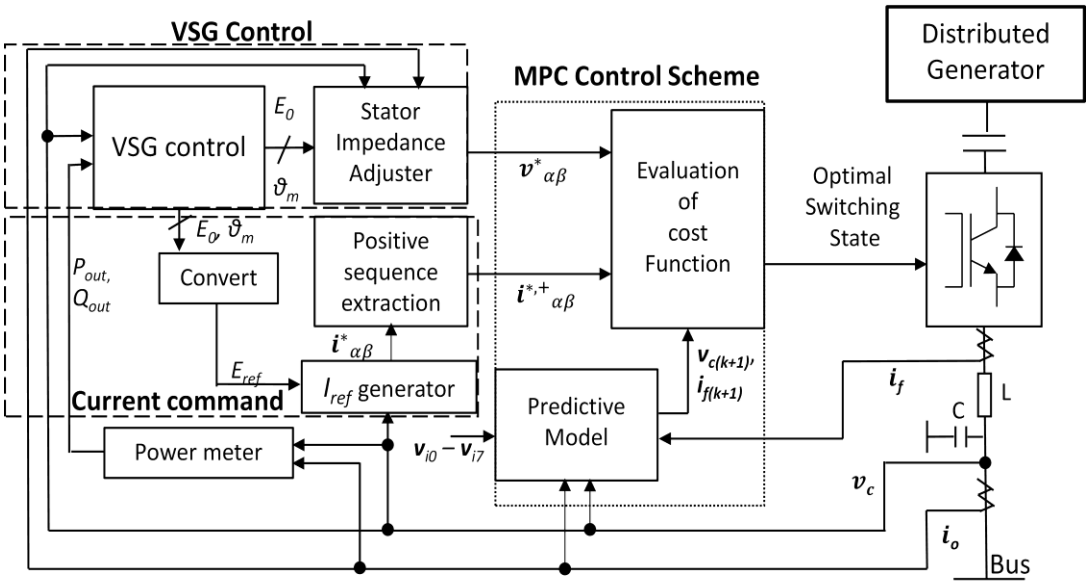

Fig. 3.1 Control Diagram of the purposed FCS-MPC-Based VSG Control

$$L\frac{d\boldsymbol{i}_f}{dt} = \boldsymbol{v}_i - \boldsymbol{v}_c \tag{3.2}$$

where $\boldsymbol{v}_c = \left[v_{c,\alpha}\ v_{c,\beta}\right]^T$, $\boldsymbol{v}_i = \left[v_{i,\alpha}\ v_{i,\beta}\right]^T$, $\boldsymbol{i}_f = \left[i_{f,\alpha}\ i_{f,\beta}\right]^T$ and $\boldsymbol{i}_o = \left[i_{o,\alpha}\ i_{o,\beta}\right]^T$ are output voltage, inverter voltage, inductor current, and the output current. These equations can be rewritten as follows (3.3):

$$\frac{d\boldsymbol{x}}{dt} = \boldsymbol{A}\boldsymbol{x} + \boldsymbol{B}\boldsymbol{v}_i + \boldsymbol{B}_d\boldsymbol{i}_o \tag{3.3}$$

where $\boldsymbol{x} = \begin{bmatrix} i_{f,\alpha} \\ i_{f,\beta} \\ v_{c,\alpha} \\ v_{c,\beta} \end{bmatrix}, \boldsymbol{A} = \begin{bmatrix} 0 & 0 & -\frac{1}{L} & 0 \\ 0 & 0 & 0 & -\frac{1}{L} \\ \frac{1}{C} & 0 & 0 & 0 \\ 0 & \frac{1}{C} & 0 & 0 \end{bmatrix}, \boldsymbol{B} = \begin{bmatrix} \frac{1}{L} & 0 \\ 0 & \frac{1}{L} \\ 0 & 0 \\ 0 & 0 \end{bmatrix}$ and $\boldsymbol{B_d} = \begin{bmatrix} 0 & 0 \\ 0 & 0 \\ -\frac{1}{C} & 0 \\ 0 & -\frac{1}{C} \end{bmatrix}$

A discrete-time model of the system derived from (3.3) for a sampling time T_s can be expressed in (3.4), as explained by [38].

$$\boldsymbol{x}(k+1) = \boldsymbol{A}_q\boldsymbol{x}(k) + \boldsymbol{B}_q\boldsymbol{v_i}(k) \ + \boldsymbol{B}_{dq}\boldsymbol{i}_o(k) \tag{3.4}$$

where $\boldsymbol{A}_q = e^{\boldsymbol{A}T_s}, \boldsymbol{B}_q = \int_0^{T_s} e^{\boldsymbol{A}\tau}\,\boldsymbol{B}d\tau$ and $\boldsymbol{B}_{dq} = \int_0^{T_s} e^{\boldsymbol{A}\tau}\,\boldsymbol{B}_d d\tau$.

From (3.4), it can be seen that the future values $\boldsymbol{v_c}(k+1)$ and $\boldsymbol{i_f}(k+1)$ can be determined according to each possible input voltage $\boldsymbol{v_i}(k)$.

3.2.1 Current Command Generation

With the MIMO system, FCS-MPC can embed voltage and current into a single loop control, as depicted in Fig. 3.1. In order to achieve this, the current reference needs to be provided for the controller. The current command can be determined by considering the relationship between the inverter phase voltage, line currents, and the capacitor phase voltage, as shown in Fig. 3.2. It can be described in a stationary frame or $\alpha\beta$-frame with Eq. (3.5).

$$\boldsymbol{v}_{i,\alpha\beta} = \boldsymbol{v}_{C,\alpha\beta} + \boldsymbol{i}_{f,\alpha\beta}(R_f + j(X_{L,f} + X_S)) \tag{3.5}$$

where $\boldsymbol{v}_{i,\alpha\beta}$ is inverter phase voltage, $\boldsymbol{i}_{f,\alpha\beta}$ the filter current and $\boldsymbol{v}_{C,\alpha\beta}$ is the capacitor voltages. Let X_S denote the virtual stator reactance, $X_{L,f}$ the filter reactance and R_f denote filter resistance.

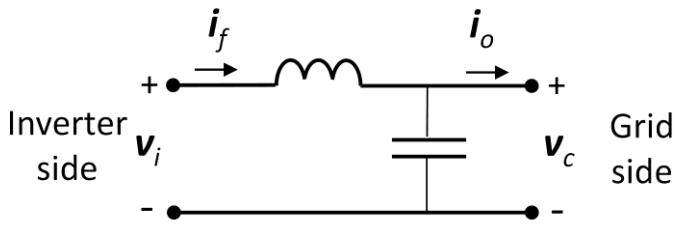

Fig. 3.2 Control Diagram of the purposed FCS-MPC-Based VSG Control

Unlike the previous VSG controls, the voltage command in the FCS-MPC scheme is used to control capacitor voltage instead of inverter voltage, and thus, the voltage drop in the filter inductance has to be compensated in the voltage command. This can be achieved by adding L_f to the virtual impedance (L_{ls}) in the stator impedance adjuster. Hence the total virtual impedance in FCS-MPC's case becomes $X_S = \omega(L_S + L_{ls})$. If we consider the $\boldsymbol{v_{i,\alpha\beta}}$ in (3.5) to equal the voltage command of VSG control without virtual impedance, the currents references i_α^* and i_β^* can be expressed as illustrated in Eq. (3.6) and they will be used as the current command for FCS-MPC.

$$\begin{bmatrix} i_\alpha^* \\ i_\beta^* \end{bmatrix} = \boldsymbol{Y}\left\{\begin{bmatrix} E_0 cos\theta_m \\ E_0 sin\theta_m \end{bmatrix} - \begin{bmatrix} v_{c,\alpha} \\ v_{c,\beta} \end{bmatrix}\right\} \tag{3.6}$$

where $\boldsymbol{Y} = \frac{1}{{R_f}^2 + {X_S}^2}\begin{bmatrix} R_f & X_S \\ -X_S & R_f \end{bmatrix}$, E_0 is internal emf reference and θ_m the phase angle reference from VSG. The overcurrent limiting can be fulfilled by merely limiting the magnitude of currents references i_α^* and i_β^*.

In order to balance the power-sharing between parallel inverters, the stator impedance adjuster was added to VSG control. In this block, the product of output current and virtual impedance is added to the voltage command, as demonstrated in Fig. 3.1 However, in the event of unbalanced short-circuit faults, the output current becomes imbalanced. This unbalance distorts the voltage command and thus generates a non-sinusoidal current in the DG. Unlike other presented control methods, FCS-MPC uses a control loop in $\alpha\beta$-axis. Since the inverter current is controlled to track the current reference, as discussed in the previous section, the current control has the ability to suppress distortion in current as long as current reference remains sinusoidal. This can be accomplished by removing negative-sequence from current reference. For this purpose, the method proposed in [19], referred to as second-order generalized integrator (SOGI) bandpass filter (BPF) depicted in Fig. 3.3, is considered in this work. According to [20], the positive-phase-sequence vectors can be extracted with the following equations.

$$\boldsymbol{i}_\alpha{}^{(p)}(t) = \left[\boldsymbol{\imath}'_\alpha(t) - \mathrm{q}\boldsymbol{\imath}'_\beta(t)\right] \tag{3.7}$$

$$\boldsymbol{i}_\beta{}^{(p)}(t) = \left[\boldsymbol{\imath}'_\beta(t) + \mathrm{q}\boldsymbol{\imath}'_\alpha(t)\right] \tag{3.8}$$

where $\boldsymbol{i}_{\alpha\beta}{}^{(p)}(t)$ are the amplitudes of positive-phase-sequence voltage vectors, $\boldsymbol{\imath}'_{\alpha\beta}$ is the fundamental component of $\boldsymbol{i}_{\alpha\beta}{}^{(p)}(t)$, q is a phase-shift operator in the time-domain which obtains the quadrature-phase waveform (90-degrees lag) of the original in-phase waveform. Hence, the new current command can be derived from (3.7) and (3.8).

3.2.2 Cost Function

Contrarily to classical control schemes, the presence of the cost function allows FCS-MPC to take into account a number of control goals, and to control different state variables simultaneously. Therefore, it is highly vital to select the cost function properly. For the control of VSI-based VSG, the

control system is set to track the voltage and current reference($\boldsymbol{v}^*_{\alpha\beta}$ and $\boldsymbol{i}^*_{\alpha\beta}$) simultaneously. This can be achieved by defining the cost function (3.9).

$$g = (\boldsymbol{v}_{c,\alpha\beta(k+1),pu} - \boldsymbol{v}^*_{\alpha\beta,pu})^2 + (\boldsymbol{i}_{f,\alpha\beta(\mathrm{k}+1),pu} - \boldsymbol{i}^*_{\alpha\beta,pu})^2 \tag{3.9}$$

where $\boldsymbol{v}^*_{\alpha\beta,pu} = \left[v^*_\alpha \; v^*_\beta\right]^T$ is the reference vector of the capacitor voltage in the per-unit system, $\boldsymbol{i}^{*(\mathrm{p})}_{\alpha\beta,pu} = \left[\boldsymbol{i}^*_\alpha \; \boldsymbol{i}^*_\beta\right]^T$ is the reference vector of the inductor current in the per-unit system, $\boldsymbol{v}_{c,\alpha\beta}(k+1) = \left[v_\alpha \; v_\beta\right]^T$ is the predicted capacitor voltage and $\boldsymbol{i}_{f,\alpha\beta}(k+1) = \left[i_\alpha \; i_\beta\right]^T$ is the predicted inductance current. Additionally, weighting factors can be included in the cost function to tune the importance between the overcurrent-limiting effect and active/reactive power control. (Power control is prioritized when a larger weighting factor is selected for voltage reference tracking, and smaller weighting factor works contrariwise.)

3.2.3 Virtual Voltage Vectors for Harmonic Reduction

One of the problems of FCS-MPC is the low degree of freedom in switching instances compared to PWM. While PWM-based control uses an explicit solution of the system to calculate the switching instances of the inverter, FCS-MPC can only change its switch state once within a sample period after the calculation is done. Furthermore, a constant switching frequency is not guaranteed in FCS-MPC, as the change of switching state in each sampling is determined from the cost function process. These result in a variable switching frequency or large ripples with a broad harmonic spectrum.

In order to alleviate these problems, the idea of virtual vectors was proposed in [21] and [22]. Virtual vectors are generated as a linear combination of the discrete physical states of the inverter. However, unlike [21] and [22], 24 extra virtual vectors in addition to the 7 switching states, are generated. Totally, 31 voltage vectors are utilized for predictive control, as demonstrated in Fig. 3.4. This number was selected based on the computational capability of available hardware, as a higher number of virtual vectors would bring the total computational time closer toward 25% of the modulation period. This would result in an inaccurate generation of some of the virtual vectors, as explained later in this section. The extra switching states grant more freedom to the switching instances

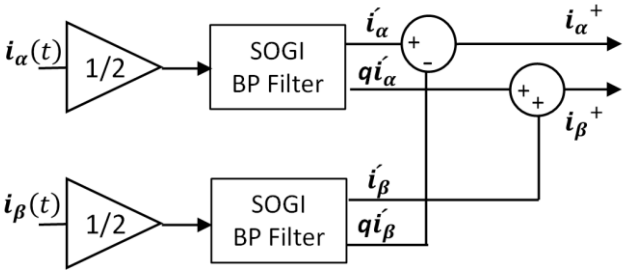

Fig. 3.3 Structure for extracting positive sequences based on SOGI-BPF.

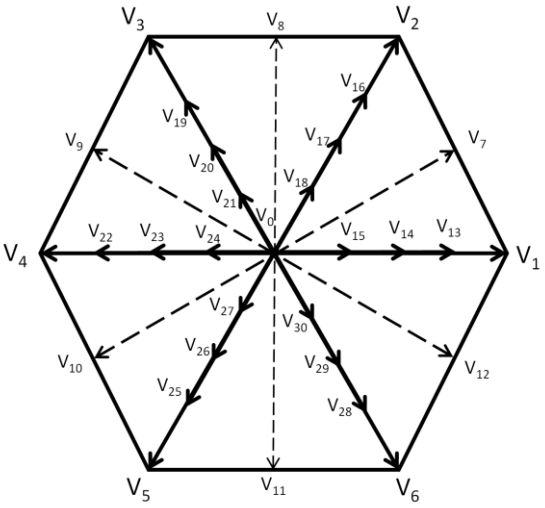

Fig. 3.4 Interpolated virtual switching states

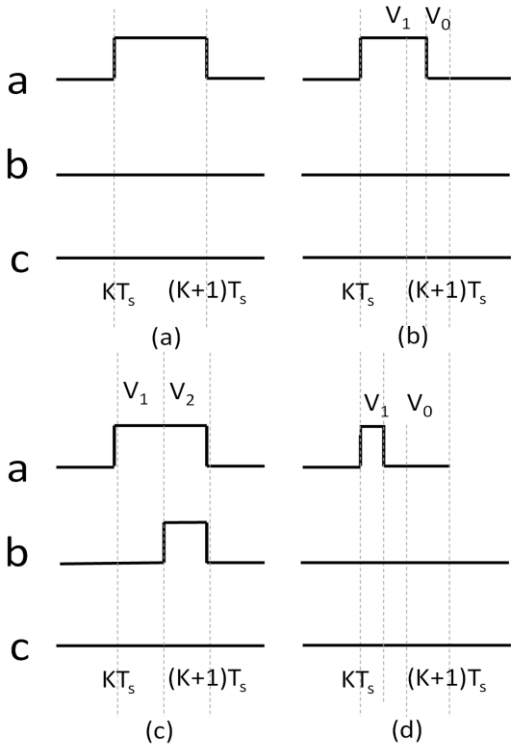

Fig. 3.5 Modulation of interpolated switching states; (a) switching states v_1. (b) switching states v_{13}. (c) switching states v_7. (d) switching states v_{15}

of FCS-MPC. The switching states *V0, V1, V2, V3, V4, V5,* and *V6* in the figure represent the physical switching states of an inverter, as explained in section 2.4. When a combination of these real vectors is applied in a switching sequence for a specific time quantity, new virtual vectors can be

generated. This can be further explained with the diagram in Fig. 3.5 It illustrates the virtual switching states *V7*, *V13,* and *V15*, for which each of its virtual states is implemented by modulation of the two nearest physical switching states (*i.e., V1* and *V2*) or one physical state and one zero vector (*i.e., V1* and *V0*). For instances, switching states *V13* results from applying *V1* for 75% of the modulation period (T_S), whereas *V0* is applied for 25% of the period. Similarly, switching states *V7* can be created by applying *V1* and *V2* for 50% of the modulation period each, and switching states *V15* is generated when *V0* is applied for 75% and *V1* is applied for 25% of the period, respectively. The same principle goes for the creation of the rest of the virtual vectors. By doing so, the inverter has three more possibilities to change its state at 25%, 50%, or 75% of the modulation period instead of always switching at the end/start of the modulation period. Hence, switching instances of FCS-MPC becomes more flexible, and harmonic caused by switching frequency can be reduced in exchange of higher calculation time since 31 sets of inverter voltage vectors (including one zero voltage vector) are used during prediction instead of eight in the conventional method.

3.2.4 Filter Resonance

The average switching frequency of FCS-MPC is challenging to determine in advance since it depends not only on the sampling frequency but also on the inverters operating point. Hence, the spread harmonic spectrum of FCS-MPC might contain components at the resonant frequency of *LCL*-filter at a certain point of operating. However, this will result in resonance, only when, no more than one of the three states of the filter (inverter current ($i_f(s)$) for predictive direct current control [23]-[27]) is directly controlled, whereas two other states, i.e., grid side inductor current ($i_o(s)$) and capacitor voltage ($v_c(s)$), are indirectly controlled by the first state and thus highly dependent on filter impedances.

As most of the previously presented FCS-MPC-based grid-connected DGs utilize the single-input-single-output (SISO) system-based predictive direct current control or predictive power control strategies [23]-[27], only $i_f(s)$ is directly regulated. To avoid resonance, distortion in the other states of the filter such as $v_c(s)$ needs to be indirectly restrained through $i_f(s)$ reference. This can be achieved by an active damping strategy based on virtual resistance (VR), which has been applied to the FCS-MPC based grid-connected VSI with some success [26], [27]. Nevertheless, problems may occur as soon as $v_c(s)$ is distorted by harmonics, which cannot be dampened by VR.

My proposed FCS-MPC, on the other hand, utilizes MIMO system to control both $v_c(s)$ and $i_f(s)$ simultaneously. This is different from conventional cascade control of voltage and current, where settling time of the inner loop has to be significantly faster than the settling time of the outer loop. Therefore, at the resonance frequency where $v_c(s)$ and $i_f(s)$ are oscillating with the same dynamics, the control of the outer loop is not fast enough to provide damping effect. Contrarily, the multivariable control of FCS-MPC is conducted at the same bandwidth. This ensures that the regula-

tion of $v_c(s)$ can damp the distortion caused by the harmonics of $i_f(s)$ and the control of $i_f(s)$ is able to reduce the disturbance caused by the harmonics of $v_c(s)$. Additionally, only two degrees of freedom exist out of the three states of the *LCL*-filter since $i_o(s)$ is a function of $v_c(s)$ and $i_f(s)$. Hence, by controlling both degrees of freedom of the *LCL*-filter, the frequency response between the filter states is no longer influenced by its impedance alone. Thus the uncontrolled resonant energy oscillation between the inductances and the capacitance is effectively avoided. This concept has been successfully applied in grid-connected AC/DC-converters, as proposed in [28]-[31]. A similar concept was also proposed in [32].

3.2.5 Issue of Stability

Stability analysis of FCS-MPC has been until recently relatively undeveloped despite its success in a variety of power electronics applications. One of the main reasons is due to the fact that the MPC strategy, in general, does not provide an explicit solution of the system. This makes characterizing the resulting closed-loop performance a highly complex task [33]. Alternatively, a capable stability analysis method was proposed based on the Lyapunov stability theory in [34]. Instead of a closed-loop performance study, the work suggested that practical stability can be established by considering the cost function of the optimal problem as a candidate Lyapunov function. A similar concept was proposed later on in [35]–[36], and it was concluded that the cost function of FCS-MPC could be designed to obtain the desired performance while guaranteeing the practical stability of the power converter. In this work, stability analysis was not conducted as it is not the focus of my research. Nevertheless, stability issue is considered one of the most important open problems for FCS-MPC and the prior studies in [34]–[36] can be used as references to carry out further research on this topic.

3.3 Simulation and Discussion

In order to verify whether the ability of VSG control is inherited by the FCS-MPC-based control scheme, the simulation of the test circuit, shown in Fig. 3.6, is conducted. The simulation parameters are concluded in Table 3.1. The proposed control scheme is tested under both grid-connected and islanded operations. First, DG1 and DG2 are connected at the bus and to the grid. A sudden change of grid frequency from 60 Hz to 59.7 Hz has been simulated when the system operates in the grid-connected mode with a power reference of 5 kW at T = 2 s. For a real power system, the frequency will never change instantaneously, but this case is simulated to study a worst-case scenario of frequency disturbance. Then DGs are disconnected from the grid at T = 4 s. Finally, during the islanded operation, the load will change from 5.1 kW, 0.2 kvar to 7.3 kW, 0.6 kvar.

The simulation results are shown in Fig. 3.7. From Fig. 3.7 (a), it can be seen that during grid-connected operation, the two DGs are sharing active and reactive power properly according to their ratings throughout the operation. When grid frequency decreased at T = 2 s, the overshoot of

TABLE 3.1 SIMULATION PARAMETERS

Parameter	Value	Parameter	Value
S_{base1}	5 kVA	M_i^*	4 s
S_{base2}	2.5 kVA	X_{S1}	0.9pu
$E_0 = V_{grid}$	200 V	X_{S2}	0.9pu
$\omega_0 = \omega_{grid}$	376.99 rad/s	$Q_{0\,i}^*$	0 pu
$P_{0\,i}^*$	1 pu		
POLE PLACEMENT PARAMETERS			
Parameter	Value	Parameter	Value
k_p	20 pu	k_{xw}	156.2718 pu
k_{xp}	14.36193 pu	k_{xi}	110.1699 pu

active power can be observed in Fig. 3.7(a) for both DGs. This implies that the reduction in grid frequency is releasing inertial energy from the VSG, resulting in a power injection to the grid in or-

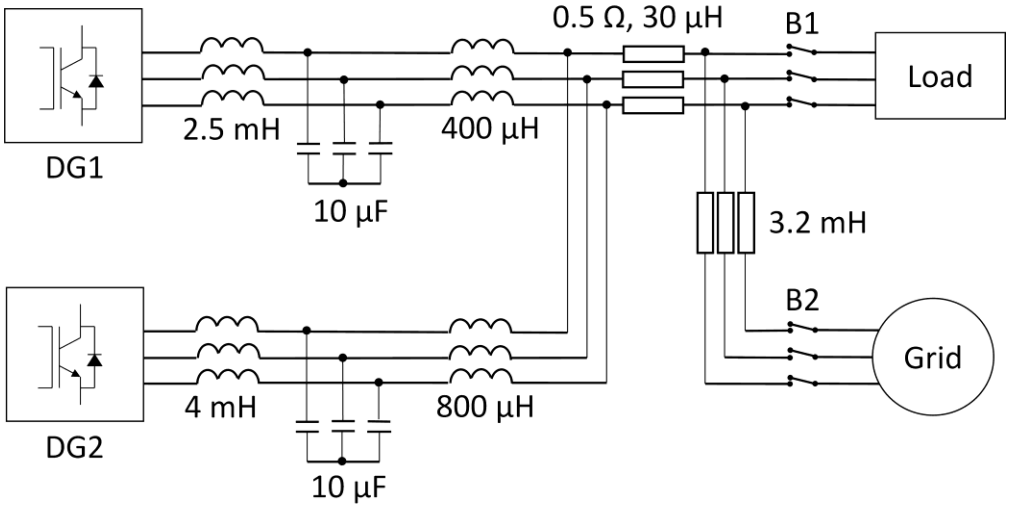

Fig. 3.6. Simulation circuit diagram

der to slow down the change of grid frequency. This is different from droop characteristics because in case of droop control, although power will increase due to the decrease in frequency. No overshoot will be observed. At time T = 4., the two DGs are disconnected from the grid. The active and reactive power, shown in Fig. 3.7(a), and output amplitude, shown in Fig. 3.7(b), indicate that the DG can smoothly transit from grid-tied operation to islanded operation. As illustrated in Fig. 3.7(c).

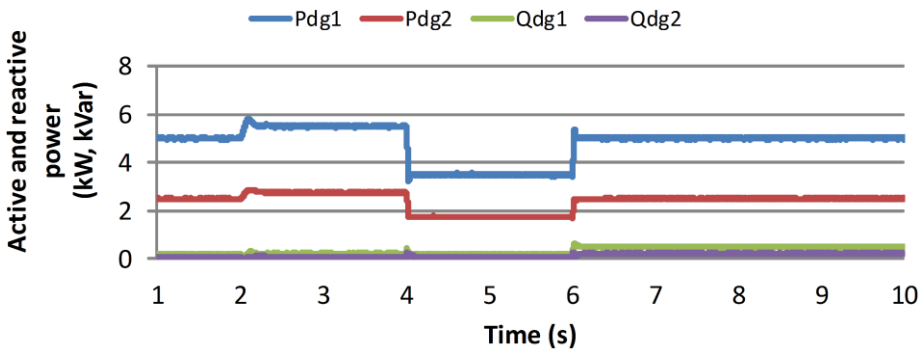

(a)

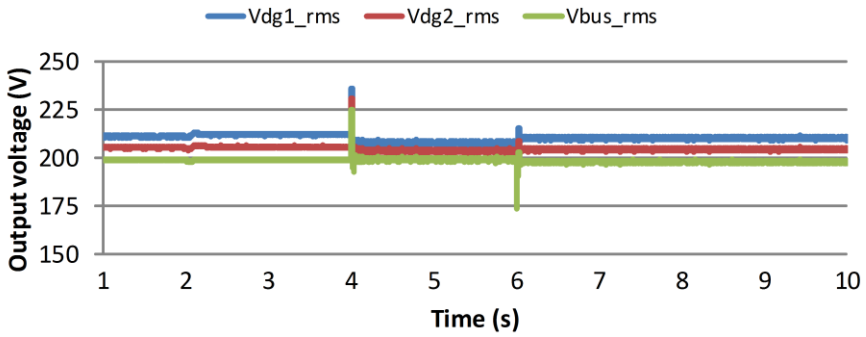

(b)

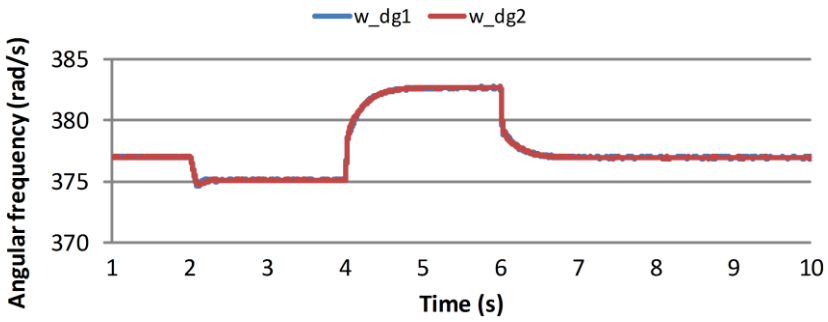

(c)

Fig. 3.7. Simulation results of the proposed control in grid-connected and islanded mode under normal condition

the frequency outputs of DGs are slowly changing, which indicates the inertia response of the VSGs. The same phenomena can be observed at $T = 6$ s. when loading changes from 5.1 kW, 0.2 kvar to 7.3 kW, 0.6 kvar. Furthermore, the output amplitudes of DGs are maintained around the nominal values throughout the operation. Hence, It can be concluded that the proposed FCS-MPC-based VSG control inherits all the properties of VSG control.

3.4 Conclusion

In this chapter, a FCS-MPC-based control scheme is presented for a three-phase inverter with an output *LCL* filter, beginning with the design procedure for FCS-MPC and the integration of VSG control into FCS-MPC control. The open issues of FCS-MPC, such as stability analysis and harmonic reduction, are also discussed in this chapter. Finally, the simulation results of the proposed control under the normal operating condition are presented. Results show that the proposed scheme can operate in both grid-connected and islanded modes while achieving proper active and reactive power sharing, proper control of output voltage, and virtual inertia feature to slow down frequency deviation during load transitions and grid islanding. Hence, it is confirmed that the proposed FCS-MPC-based VSG control inherits all the properties of VSG control. The proposed control is also capable of a current limiting ability since the multivariable control of voltage and current is achieved. This statement will be verified in Chapter 4.

References

[1] J. Driesen and K. Visscher "Virtual synchronous generators," *in Proc. 2008 IEEE Power Energy Soc. Gen. Meeting—Convers. Del. Elect. Energy 21st Century*, pp. 1–3.

[2] K. Sakimoto, Y. Miura, and T. Ise, "Stabilization of a power system including inverter type distributed generators by the virtual synchronous generator," *IEEJ Trans. Power and Energy*, vol. 132, no. 4, pp. 341–349, Apr. 2012.

[3] Q.-C. Zhong and G. Weiss, "Synchronverters: inverters that mimic synchronous generators," *IEEE Trans. Ind. Electron*., vol. 58, no. 4, pp. 1259–1267, Apr. 2011.

[4] Q.-C. Zhong, P.-L. Nguyen, Z. Ma, and W. Sheng, "Self-synchronized synchronverters: inverters without a dedicated synchronization unit," *IEEE Trans. Power Electron.*, vol. 29, no. 2, pp. 617–630, Feb. 2014.

[5] M. Guan, W. Pan, J. Zhang, Q. Hao, J. Cheng, and X. Zheng, "Synchronous generator emulation control strategy for voltage source converter (VSC) stations," *IEEE Trans. Power Syst.*, vol. 30, no. 6, pp. 3093–3101, Nov. 2015.

[6] H. Wu, X. Ruan, D. Yang, X. Chen, W. Zhao, Z. Lv, and Q.-C. Zhong, "Small-signal modeling and parameters design for virtual synchronous generators," *IEEE Trans. Ind. Electron*., vol. 63, no. 7, pp. 4292–4303, Jul. 2016.

[7] S. D'Arco and J. A. Suul, "Virtual synchronous machines - Classification of implementations and analysis of equivalence to droop controllers for microgrids," *2013 IEEE Grenoble Conference*, Grenoble, 2013, pp. 1-7.

[8] J. M. Guerrero, J. Matas, L. G. de Vicuña, M. Castilla, J. Miret, "Wireless-Control Strategy for Parallel Operation of Distributed- Generation Inverters," *IEEE Transactions on Industrial Electronics*, Vol. 53, No. 5, pp 1461-1470, October 2006.

[9] J. Liu, Y. Miura and T. Ise, "Comparison of Dynamic Characteristics Between Virtual Synchronous Generator and Droop Control in Inverter-Based Distributed Generators," *IEEE Transactions on Power Electronics*, vol. 31, no. 5, pp. 3600-3611, May 2016.

[10] N. Bottrell and T. Green, "Comparison of current-limiting strategies during fault ride-through of inverters to prevent latch-up and wind-up", *IEEE Trans. Power Electron*, vol. 29, no. 7, pp. 3786–3797, 2014.

[11] C. Plet, M. Graovac, T. Green, and R. Iravani, "Fault response of grid-connected inverter dominated networks," *IEEE Power and Energy Society General Meeting*, Jul. 2010, pp. 1–8, 2010.

[12] J. Rodriguez et al., "State of the Art of Finite Control Set Model Predictive Control in Power Electronics," *IEEE Transactions on Industrial Informatics,* vol. 9, no. 2, pp. 1003-1016, May 2013.

[13] H. Miranda, R. Teodorescu, P. Rodriguez, and L. Helle: "Model predictive current control for high-power grid-connected converters with output LCL filter", *Conf. of IEEE Ind. Electron*, Proc. 35th Annu, pp. 633-638, 2009.

[14] B. Arif, L. Tarisciotti, P. Zanchetta, J. C. Clare and M. Degano, "Grid Parameter Estimation Using Model Predictive Direct Power Control," *IEEE Transactions on Industry Applications*, vol. 51, no. 6, pp. 4614-4622, Nov.-Dec. 2015.

[15] J. Hu, J. Zhu, D. G. Dorrell: "Model predictive control of inverters for both islanded and grid-connected operations in renewable power generations", *IET Renewable Power Generation*, Vol. 8, Iss. 3, pp. 240-248, 2014.

[16] L. A. Serpa, S. Ponnaluri, P. M. Barbosa and J. W. Kolar, "A Modified Direct Power Control Strategy Allowing the Connection of Three-Phase Inverters to the Grid Through *LCL* -Filters," *IEEE Transactions on Industry Applications*, vol. 43, no. 5, pp. 1388-1400, Sept.-oct. 2007.

[17] J. Jongudomkarn, J. Liu and T. Ise, "Comparison of Current-Limiting Strategies of Virtual Synchronous Generator Control during Fault Ride-Through," *IFAC-PapersOnLine*, vol. 51, issue 28, 2018, pp. 256-261.

[18] J. Liu, Y. Miura, and T. Ise, "Fixed-parameter damping methods of virtual synchronous generator control using state feedback," *IEEE Access*, vol. 7, pp. 99177–99190, 2019.

[19] . V. Timbus, P. Rodriguez, R. Teodorescu, M. Liserre, and F. Blaabjerg, "Control Strategies for Distributed Power Generation Systems Operating on Faulty Grid," *2006 IEEE International Symposium on Industrial Electronics*, Montreal, Que., 2006, pp. 1601-1607.

[20] P. Cortes, G. Ortiz, J. I. Yuz, J. Rodriguez, S. Vazquez and L. G. Franquelo, "Model Predictive Control of an Inverter With Output *LC* Filter for UPS Applications," *IEEE Transactions on Industrial Electronics*, vol. 56, no. 6, pp. 1875-1883, June 2009.

[21] S. Vazquez et al., "Model Predictive Control with constant switching frequency using a Discrete Space Vector Modulation with virtual state vectors," 2009 *IEEE International Conference on Industrial Technology*, Gippsland, VIC, 2009, pp. 1-6.

[22] H. Moon, J. Lee, and K. Lee, "A Robust Deadbeat Finite Set Model Predictive Current Control Based on Discrete Space Vector Modulation for a Grid-Connected Voltage Source Inverter," *IEEE Transactions on Energy Conversion*, vol. 33, no. 4, pp. 1719-1728, Dec. 2018.

[23] H. Miranda, R. Teodorescu, P. Rodriguez, and L. Helle: “Model predictive current control for high-power grid-connected converters with output LCL filter”, *Conf. of IEEE Ind. Electron*, Proc. 35th Annu, pp. 633-638, 2009.

[24] B. Arif, L. Tarisciotti, P. Zanchetta, J. C. Clare and M. Degano, "Grid Parameter Estimation Using Model Predictive Direct Power Control," *IEEE Transactions on Industry Applications*, vol. 51, no. 6, pp. 4614-4622, Nov.-Dec. 2015.

[25] J. Hu, J. Zhu, D. G. Dorrell: “Model predictive control of inverters for both islanded and grid-connected operations in renewable power generations”, *IET Renewable Power Generation*, Vol. 8, Iss. 3, pp. 240-248, 2014.

[26] L. A. Serpa, S. Ponnaluri, P. M. Barbosa and J. W. Kolar, "A Modified Direct Power Control Strategy Allowing the Connection of Three-Phase Inverters to the Grid Through *LCL* -Filters," *IEEE Transactions on Industry Applications*, vol. 43, no. 5, pp. 1388-1400, Sept.-oct. 2007.

[27] F. Donoso, A. Mora, R. Cárdenas, A. Angulo, D. Sáez, and M. Rivera, "Finite-Set Model-Predictive Control Strategies for a 3L-NPC Inverter Operating With Fixed Switching Frequency," *IEEE Transactions on Industrial Electronics*, vol. 65, no. 5, pp. 3954-3965, May 2018

[28] Z. Ma, S. Saeidi, and R. Kennel, "FPGA Implementation of Model Predictive Control With Constant Switching Frequency for PMSM Drives," *IEEE Transactions on Industrial Informatics*, vol. 10, no. 4, pp. 2055-2063, Nov. 2014.

[29] J. Scoltock, T. Geyer, and U. K. Madawala, "A Model Predictive Direct Current Control Strategy With Predictive References for MV Grid-Connected Converters With *LCL* -Filters," *IEEE Transactions on Power Electronics*, vol. 30, no. 10, pp. 5926-5937, Oct. 2015.

[30] P. Falkowski and A. Sikorski, "Dead-time compensation in a new FCS-MPC of an AC/DC converter with a *LCL* filter," *2016 13th Selected Issues of Electrical Engineering and Electronics (WZEE)*, Rzeszow, 2016, pp. 1-6.

[31] N. Panten, N. Hoffmann, and F. W. Fuchs, "Finite Control Set Model Predictive Current Control for Grid-Connected Voltage-Source Converters With *LCL* Filters: A Study Based on Different State Feedbacks," *IEEE Transactions on Power Electronics*, vol. 31, no. 7, pp. 5189-5200, July 2016.

[32] P. Falkowski and A. Sikorski, "Finite Control Set Model Predictive Control for Grid-Connected AC–DC Converters With *LCL* Filter," *IEEE Transactions on Industrial Electronics*, vol. 65, no. 4, pp. 2844-2852, April 2018.

[33] D. E. Quevedo, G. C. Goodwin, and J. A. De Doná, “Finite constraint set receding horizon quadratic control,” *Int. J. Robust Nonlinear Control*, vol. 14, no. 4, pp. 355–377, Jan. 2004.

[34] R. Aguilera and D. Quevedo, “On stability and performance of finite control set MPC for power converters,” in *Proc. Workshop Predictive Control Elect. Drives Power Electron,* 2011, pp. 55–62.

[35] R. Aguilera and D. Quevedo, “Predictive control of power converters: Designs with guaranteed performance,” *IEEE Transaction* Industrial Informatics, vol. 11, no. 1, pp. 53–63, Feb. 2015.

[36] H. T. Nguyen and J. Jung, "Finite Control Set Model Predictive Control to Guarantee Stability and Robustness for Surface-Mounted PM Synchronous Motors," *IEEE Transactions on Industrial Electronics*, vol. 65, no. 11, pp. 8510-8519, Nov. 2018.

Chapter 4
Comparison between FCS-MPC and Other Existing Methods for VSG Control-Based Inverter Regarding Fault-Ride-Through Ability

4.1 Introduction

Although the results of the past research works have clearly demonstrated that the VSG-based DGs can contribute to the creation of inertia and damping effect and solve issues related to frequency deviations [1]-[6], still, other concerns exist over grid stability under the massive DG penetration. One of the most critical concerns is the interrupted operation in the DG system due to the effect of transient disturbances on the utility grid. Without a proper countermeasure, the whole grid could suffer from a massive imbalance between the power supply and power demand. According to the Japanese grid code [7], the requirements for the power conditioner of low voltage ride through (LVRT) or fault ride-through (FRT) from 2017 stated that for fault duration within 1 s and voltage drop larger than 20 % of rated voltage, the DGs have to remain connected. This indicates that in such an event of a fault, the DGs must not be tripping. Nevertheless, unlike a conventional generator, semiconductor switches in the inverter-based DGs system cannot tolerate overcurrent conditions due to their low thermal inertia [8]. Therefore, it must quickly detect the fault and prevent overcurrent in the inverter and equipment connected to the grid.

Yet, the LVRT ability of the VSG-based system has not been thoroughly analyzed. For instance, a current restraining method under balance voltage sag was presented in [9] based on control mode switching. However, it faces a challenge of managing the transition between normal mode and overcurrent mode during and after fault condition, especially against the case of asymmetrical voltage sag, where the current becomes oscillatory under unbalanced condition. A method based on virtual impedance to limit the current of VSG during the fault event was proposed in [10], despite that, only the case of balance voltage sag was presented, and thereby, there is doubt over the ability of this method against unbalance voltage sag since the proposed VSG are prone to unbalance and nonlinearity due to the absence of output voltage control loop. In [11], the evaluations of voltage sag consequences and of a current-suppressing strategy were conducted for both symmetrical and asymmetrical voltage sag, however only the case of mild voltage sag (over 0.9 pu) was studied in the presented work. Recently, a grid-connected based DG that utilized voltage references provided by VSG

to achieve current control via virtual admittance is proposed in [16]. Although the control is able to cope with unbalanced faults, since the issue of overcurrent-limiting was not explicitly addressed, it is undetermined whether the dynamic response of the method in [16] is quick enough to deal with overcurrent condition. Another way to accomplish overcurrent limiting in VSG is to use multiple loop control of voltage and current, and the current limiting can be done in the current loop by only limiting current reference as proposed in [12]. However, to ensure stability in all operating conditions, tuning of PI has to be done appropriately, which can be challenging when a number of DGs are connected together [20]. Windup and waveform clipping is also the disadvantages of this method [14]. Furthermore, when multiloop control is connected to another voltage source, the control has a problem with active and reactive power regulation during and after disturbance, as shown in [15]. Reference [14] also indicates that maintaining stability after disturbances and exiting current limiting are other issues for multiloop control. In literature, there also exist other types of current limiting strategies, which can be accomplished in the voltage control loop. These current-limiting methods are typically accomplished by reducing the voltage magnitude when the current exceeds a threshold [17], or by a current-limiting proportional-integral (PI) controller [18]. Adopting these methods in VSG control, however, could lead to another shortcoming as a complicated strategy for entering and exiting overcurrent mode is required.

In this chapter, a comparative study in simulations and experiments between the FCS-MPC based VSG with simultaneous control of voltage and current in a single control loop and two existing control schemes with the current limiting ability for VSG control, namely multiloop VSG control [13] and VSG with virtual impedances current limiting [10].

4.2 The Multiloop VSG Control

4.2.1 Overview

Multiloop control uses an outer voltage loop that provides the current reference to an inner current loop. The control has an inherent current limiting ability due to the use of current regulators. Limiting inverter current magnitude in multiloop is relatively simple; however, maintaining stability is challenging, particularly when multiloop control connects to dissimilar voltage sources such as synchronous generators [20] and grid [21]. Reference [21] also demonstrated that the use of simple current reference saturation limiters might cause instability in the event of unbalanced voltage sag since the current reference saturates and the voltage controller may lose control, as the inverter and generator frequencies diverge, and the system becomes unstable.

A multiloop VSG with a cascade structure of voltage and current control loops is presented in Fig. 4.1 The controller comprises inner and outer control loops. An inner control loop is designed to control the filter current, while an outer control loop is designed to control the inverter output voltage. Both voltage and current control loop are implemented in the synchronous reference frame (*dq*-coordinates). The voltage magnitude reference and frequency are given by the power generation

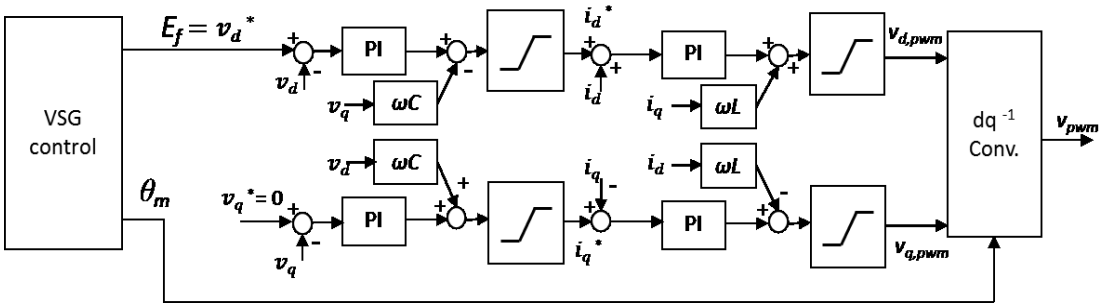

Fig. 4.1 The control diagram of multiloop VSG control

part of VSG control presented in Chapter 3. As depicted in Fig. 4.1, the controller aligns the q-axis with the output voltage by setting the d-axis voltage reference (v_d^*) to zero and the q-axis voltage reference (v_q^*) to the desired voltage magnitude. The outer loop then uses the references to control the output voltage in *dq*-coordinates ($\boldsymbol{v}_{dq}$) and provides the current reference ($\boldsymbol{i}_{dq}^*$) to the inner current loop system via PI controllers to control the output current ($\boldsymbol{i}_{dq}$), as shown in Fig. 4.1. The output of the inner controller is limited by the modulation limit of the PWM and the dc-bus voltage, while the output of the outer voltage controller is the current reference, which is limited by the current rating of the semiconductors within the inverter. The current reference saturation limiters set at +/ − 1.06 pu [20] ($I_{\text{mag}} = \sqrt{1.062 + 1.062} = 1.5$ pu).

4.2.2 Current Controller Tuning

For low order controlled plants without time delay, the modulus optimum is often used in the conventional analog controller tuning when the controlled system has one dominant time constant and other minor time constant. This method is widely used because of its simplicity and fast response. According to [13], for tuning the parameters of the inner loop current controllers in Fig. 4.1, the delay effect of the converter pulse-width modulated (PWM) operation must be considered. By approximating the effect of the PWM with a first-order transfer function and assuming feedforward of the measured voltages and ideal decoupling of the *d*- and *q*-axes, the open-loop transfer function $h_{cc,dq}$ for the current controllers can be approximated with (4.1) [22], [23].

$$h_{cc,dq}(s) \approx \left(k_{pc} + \frac{k_{ic}}{s}\right) \cdot \frac{1}{1 + T_v s} \cdot \frac{1}{R_{pu}(1 + T_1 s)} \tag{4.1}$$

where k_{pc} and k_{ic} are PI controller parameters of the inner loop of multiloop control and R_{pu} is the filter resistance in per-unit. According to [13], the time constants T_1 for the filter inductor and T_v for the delay approximation of the PWM are approximated with (4.2), as shown in the following:

$$\begin{aligned} T_1 &= \frac{L}{R} \\ T_v &\approx \frac{1}{2f_{sw}} \end{aligned} \tag{4.2}$$

when L is the filter inductor and f_{sw} is the switching frequency. Based on the open-loop transfer function in (4.1), the PI current controller gains can be selected according to the modulus optimum (MO) criterion commonly applied for current controllers in drives and grid-connected converters [22], [24]. This tuning technique corresponds to pole cancelation in the open-loop transfer function, and to a gain selecting to achieve critical damping of the resulting closed-loop transfer function. According to the technique, k_{pc} and k_{ic} can be determined by (4.3)

$$\begin{aligned} k_{pc} &= \frac{L}{2T_v} \\ k_{ic} &= \frac{R}{2T_v} \end{aligned} \tag{4.3}$$

It is clearly seen from (4.3) that the PI controller parameters and, thus, the current controller bandwidth is directly limited by the switching frequency.

4.2.3 Voltage Controller Tuning

From the cascaded structure shown in Fig. 4.1, it is clear that the tuning of outer loop control gains is constrained by the bandwidth of the inner loop current controllers. According to [13], for the sake of simplifying, the closed-loop current controllers can be approximated by a first-order transfer function [23]. Assuming an ideal decoupling of the *d*- and *q*-axes, the open-loop transfer function of the voltage controllers can be expressed by (4.4).

$$h_{vc,dq}(s) \approx \left(k_{pv} + \frac{k_{iv}}{s}\right) \cdot \frac{1}{1 + T_{eq,cc}s} \cdot \frac{1}{T_{c1}s} \tag{4.4}$$

when k_{pv} and k_{vc} are PI controller parameters of the outer loop of multiloop control and the time constant $T_{eq,cc}$ representing the closed-loop current controller and the integral time T_{c1} of the filter capacitor are defined by (4.5), where C_{pu} is the filter capacitor in per-unit and ω_0 is the nominal output frequency.

$$\begin{aligned} T_{eq,cc} &= 2T_v \\ T_{c1} &= \frac{C_{pu}}{\omega_0} \end{aligned} \tag{4.5}$$

Since the open-loop transfer function of the voltage controller (4.4) already has two poles at the origin, an alternative criterion to tune the controllers in this condition is given by the symmetrical optimum criteria. The symmetrical optimum criterion ensures maximum phase margin at the cross-over frequency of the open-loop transfer function. The tuning of PI controller gains k_{pv} and k_{iv} can be expressed as follows.

$$\begin{aligned} k_{pv} &= \frac{T_{c1}}{aT_{eq,cc}} \\ k_{iv} &= \frac{T_{c1}}{a^3 {T^2}_{eq,cc}} \end{aligned} \tag{4.6}$$

where 'a' is a design parameter that relates the tuning of the PI controller to the damping factor ζ of the closed-loop transfer function, as given by [23], [24]. The damping factor can be changed by varying 'a'. So the value of 'a' can be chosen for the condition fulfilling desired performance. According to [13], the conventional tuning approach requires a sufficient difference in the bandwidth between the outer voltage controller and the inner current controller. Traditionally, this is ensured by increasing the value of a until the bandwidth of the voltage controller is at least one decade below the current controller bandwidth.

4.3 The Virtual Impedance Current Limiting Method

4.3.1 Overview

Originally, virtual impedance is used to adjust the power-sharing between DGs. However, this impedance can also be used to limit overcurrent, as suggested in [14]. The idea is to increase virtual impedance proportional to the size of the current magnitude when the current magnitude exceeds a predefined value. This increased impedance will reduce the voltage command and thus preventing overcurrent. if the current magnitude is lower than this threshold, then the virtual impedance will be reverted back to the original value. A VSG control with virtual impedance current limiting is presented in Fig. 4.2. The control diagram is similar to the VSG control presented in subsection 2.2.1 except that the "Stator Impedance Adjuster" block is modified to achieve current-limiting ability.

4.3.2 Virtual Impedance

In order to achieve the current-limiting ability, the inverter's output impedance will be increased during an overcurrent condition. By increasing the output impedance, the voltage reference is reduced and thereby preventing the voltage controller from commanding an excessively large current reference [25]–[27]. Unlike multiloop control, where the current limiter is embedded in the current control loop, the virtual impedance adjuster can be integrated into the voltage reference controller,

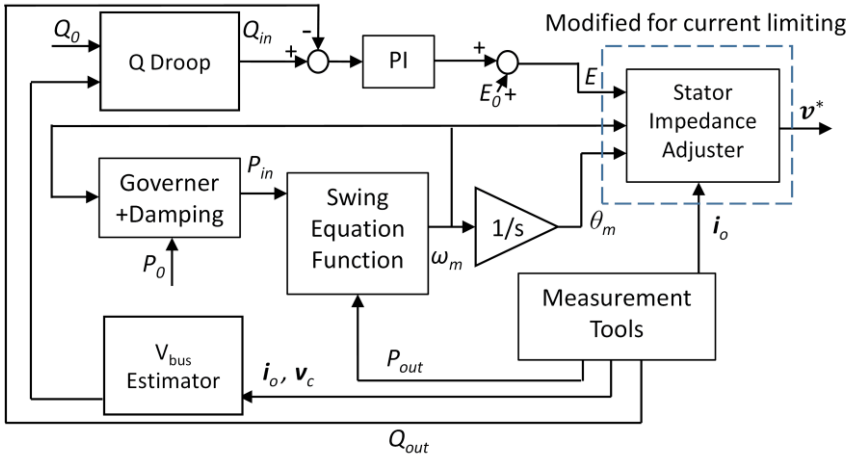

Fig. 4.2 The control diagram of VSG control with virtual impedance current limiting

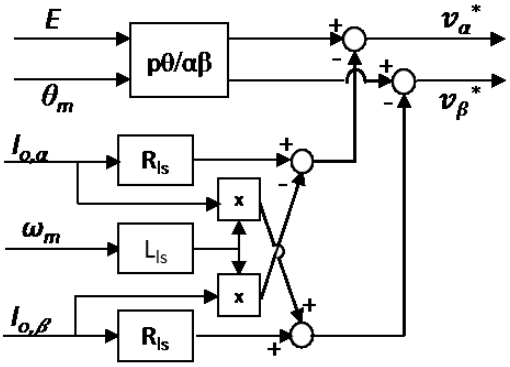

Fig. 4.3 "Stator Impedance Adjuster" block

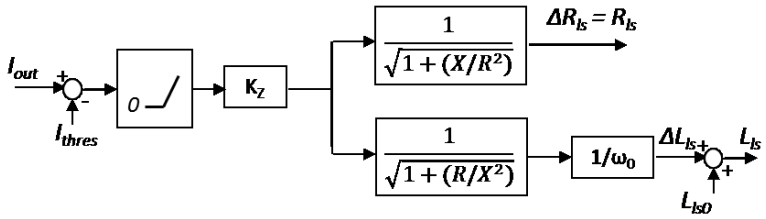

Fig. 4.4 Virtual stator impedance calculator

and hence, the current-limiting ability can be achieved without actually controlling current.

In the VSG control scheme, constant virtual stator inductance (L_{ls0}) is generated by the "Stator Impedance Adjuster" block as illustrated in Fig. 4.3. This inductance exists to assist in transient active power-sharing and system damping increasing [28]. In the VSG control with virtual impedance current limiting, the transient virtual stator impedance $\Delta Z_{ls}=\Delta R_{ls}+\omega\Delta L_{ls}$ is also generated in addition to L_{ls0} for the purpose of DG overcurrent limiting during a fault event as proposed in [14]. Hence, the overall virtual inductance (L_{ls}) becomes $L_{ls}= L_{ls0}+\Delta L_{ls}$. The effect of increased impedance to reduced peak current can be easily understood with the following equation.

$$V_0 = I_{max}\sqrt{\Delta {R_{ls}}^2 + (\omega L_{ls})^2} \tag{4.2}$$

where V_0 is the magnitude of inverter output voltage during fault and I_{max} is the desired maximum allowed current magnitude. If the voltage drop is constant, I_{max} becomes smaller as stator impedance increases. The increase in impedance was achieved by adding ΔZ_{ls} to the original virtual impedance. The value of ΔZ_{ls} is defined according to (4.3)-(4.4) and Fig. 4.4.

$$\Delta R_{ls} = \max\{K_z(i_{o,rms} - I_{thres}), 0\} \tag{4.3}$$

$$\Delta L_{ls} = \Delta R_{ls}(X/R) \tag{4.4}$$

where K_z is limiting gain, and X/R is the current limiting virtual impedance ratio. According to (4.3) and (4.4), if the output current ($i_{o,rms}$) exceeds the predefined threshold value(I_{thres}), ΔZ_{ls} proportional to the amount of overcurrent will be applied to the VSG. In this strategy, by using the amount of overcurrent to generate extra output impedance, the control will enter the current limiting mode automatically once overcurrent occurs, and it will exit the mode as soon as the overcurrent condition ceases to exist.

4.3.3 Setting Current Limit Gain

Suitable values of K_z and X/R should be chosen corresponding to the level of fault. According to [14], the voltage drop V_0 should equal the voltage magnitude command during the event of faults. This can be ensured by determining K_z and X/R that generates the desired V_0 according to equation (4.2). More explanation can be found in [14]. It should be noted that the parameter K_z is determined according to the amount of voltage drop. However, in the real system, different kind of disturbance exists, and it is hard to foresee precisely how significant the voltage drop will be. This makes the tuning of this limit gain complicated in practice. If the gain is too small, current limiting will fail. On the other hand, if the gain is too large, the amount of drop in voltage command generated by virtual impedance could surpass the magnitude of the original voltage command. This can lead to instability in the control system.

4.4 FRT-Ability Comparison Between Existing Methods and FCS-MPC-Based Method via Simulations Results

In order to evaluate the current limiting ability of each control method, the test circuit, illustrated in Fig. 4.5, is simulated in PSCAD/EMTDC for each method in grid-connected operation, and simulation and experiment are conducted for all three methods in islanded mode. DG1 has a rating of 5 kW, while DG2 has a rating of 2.5 kW. Passive *LCL* filters were used in both DG1 and DG2. The filter inductances are designed such that the voltage drop across the inductor is around 0.08 pu for the inverter side and 0.02 pu for the grid side. The capacitance *C* is then calculated to set the cut-off frequency of the filter much lower than the switching frequency. The same design was applied to all three control schemes. The virtual impedance X_S is selected as 0.9pu in this simulation to suppress non-sinusoidal current injection. A sampling frequency of 18 kHz was utilized for PWM based control schemes, whereas a sampling frequency of 40 kHz was selected for MPC in order to acquire a mean switching frequency around 14 kHz, which is at the same level as the switching frequency of the PWM control scheme (18 kHz). In order to justify the current limiting-ability of the control, peak current is expected to be lower than 2pu (40A for DG1 and 20A for DG2) throughout the operation.

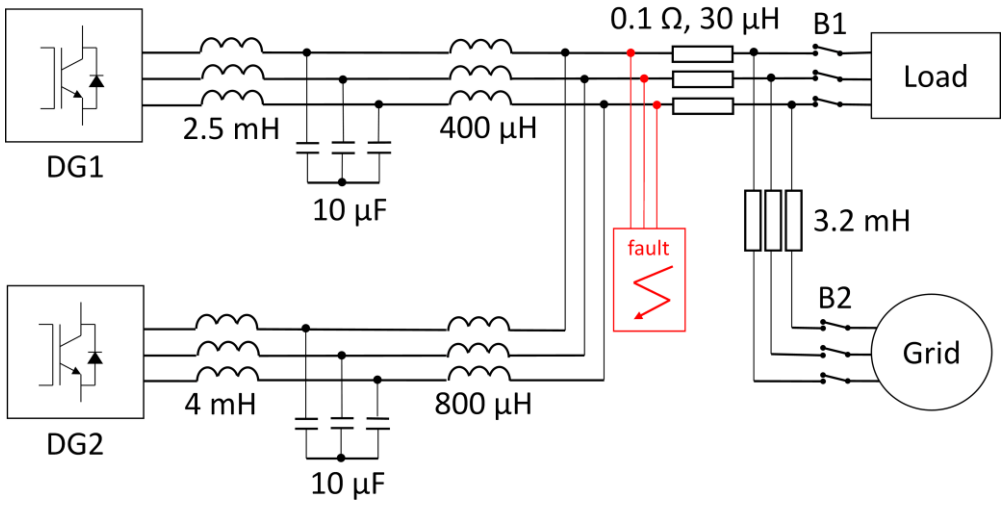

Fig. 4.5. Simulation circuit diagram

TABLE 4.1

CONTROL PARAMETERS

VSG			
Parameter	Value	Parameter	Value
S_{base1}	5 kVA	M_i^*	8 s
S_{base2}	2.5 kVA	X_{S1}	0.9pu
V_{rated}	200 V	X_{S2}	0.9pu
$\omega_0 = \omega_{grid}$	376.99 rad/s		
Multiloop			
$k_{p,v1}$	0.2857	$T_{i,v1}$	0.0025
$k_{p,i1}$	0.125	$T_{i,i1}$	0.04
$k_{p,v2}$	0.2857	$T_{i,v2}$	0.0025
$k_{p,i2}$	0.2	$T_{i,i2}$	0.04
Virtual impedance			
K_{Z1}	1.75	K_{Z2}	0.5

Important simulation parameters are listed in Table 4.1.

4.4.1 Grid-Connected Operation

For grid-connected mode, the load connected to the system is 6.6 kW+ 0.6 kVar. $P_{0,dg1}$ and $P_{0,dg2}$ are set at 5 kW and 2.5 kW, respectively, while Qref1 and Qref2 are both set to 0kVar. The events of a three-phase to ground fault and a line-to-line fault were simulated across the bus, as

shown in Fig. 4.4, while the fault resistance is set to 0.8 Ω. The fault occurs at $T = 2.5$ s and it is automatically cleared at $T = 2.7$ s. The active and reactive powers of DG1 and DG2 in the event of a three-phase fault are displayed in Fig. 4.6, for which the existing control schemes and the proposed control strategy are implemented. The active and reactive powers of multiloop control VSG, presented in Fig. 4.6(a) clearly indicate that the controller is incapable of restoring the power control after the fault is cleared. The reason for this might be the slow dynamic response of the cascade structure of multiloop control, which is unable to track the grid voltage after the fault is cleared because there is some phase difference between the output voltage of DG and grid and the voltage control. As for the VSG control with virtual impedance current limiting and the proposed FCS-MPC-based control shown in Fig. 4.6(b)-(c), the controllers are able to restore power control right after the fault clearance. Fig. 4.7 presents the current waveforms of DG1 and DG2 in the event

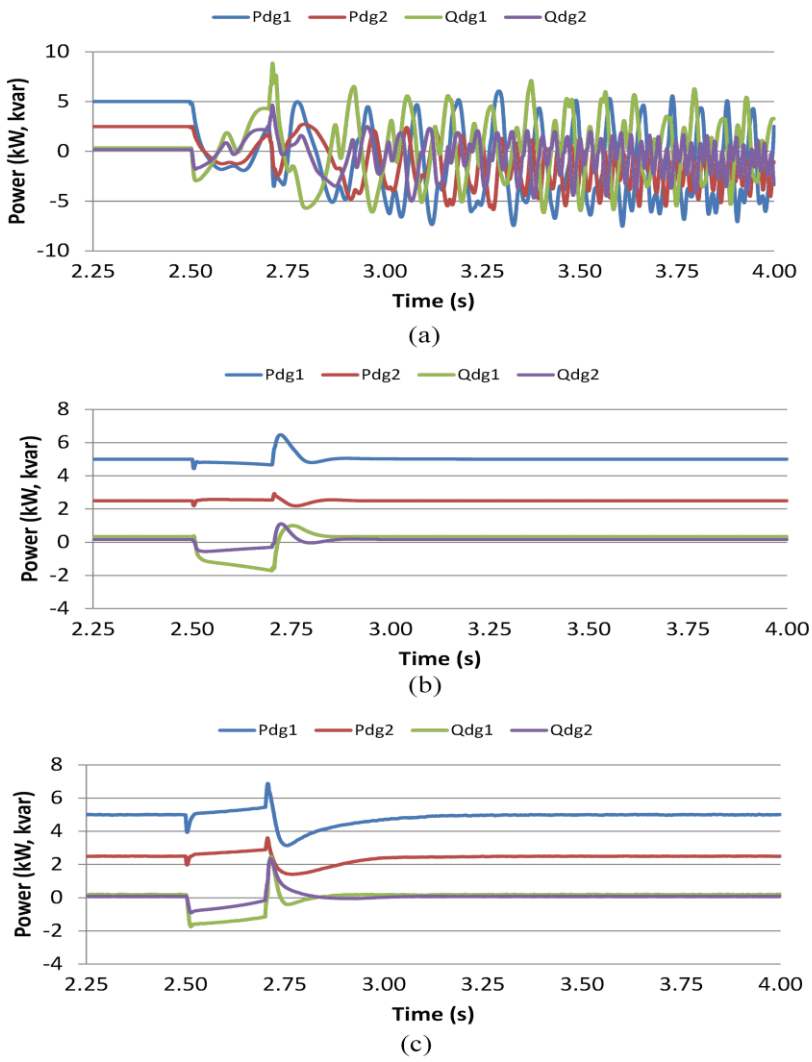

Fig. 4.6. Simulation of active and reactive power of grid-connected DG1 and DG2 in the event of a three-phase fault. (a) Multiloop control VSG. (b) VSG with virtual impedance current limiting. (c) FS-MPC based VSG

of a three-phase fault for all three control schemes under study. It can be deducted from the figures that all three controllers are capable of current limiting in the event of a three-phase fault. The waveforms of active and reactive power of DG1 and DG2 in the event of a line-to-line fault are illustrated in Fig. 4.8. Similar to the case of a three-phase fault, multiloop control failed to restore power control after fault clearing due to the low dynamic response of cascade control, while VSG control with virtual impedance current limiting and the proposed FCS-MPC-based control are able to restore power control properly. Fig. 4.9 presents the current waveforms of DG1 and DG2 in the event of a line-to-line fault. It can be deducted from Fig. 4.9 (a) that during the fault, the multiloop control was unable to limit the peak current of DG2 within the acceptable range. Hence the overcurrent-limiting failed. For the VSG control with virtual impedance current limiting, although the controller was able to limit the peak current of DG2 within the acceptable range, the limited current waveforms became distorted as the magnitude of the output current oscillated due to the unbalanced nature of the fault. Since the increased virtual impedance is generated proportional to the increased output current magnitude, it oscillated in the same way that the current magnitude did.

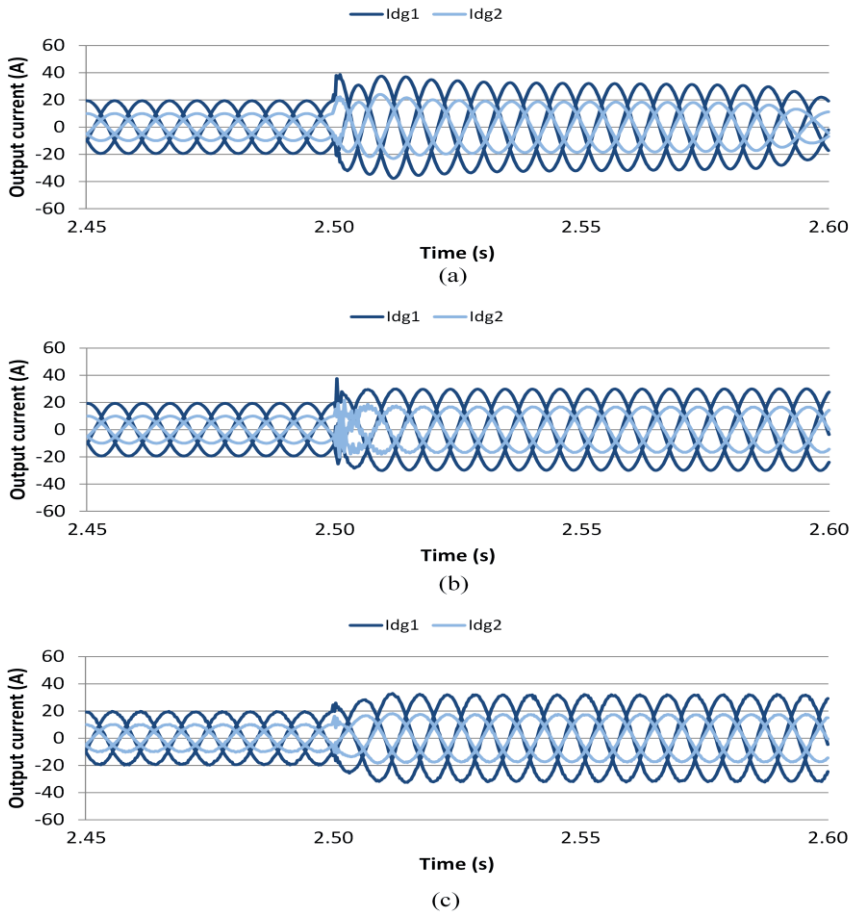

Fig. 4.7. Simulation of current waveforms of grid-connected DG1 and DG2 in the event of a three-phase fault. (a) Multiloop control VSG. (b) VSG with virtual impedance current limiting. (c) FS-MPC based VSG

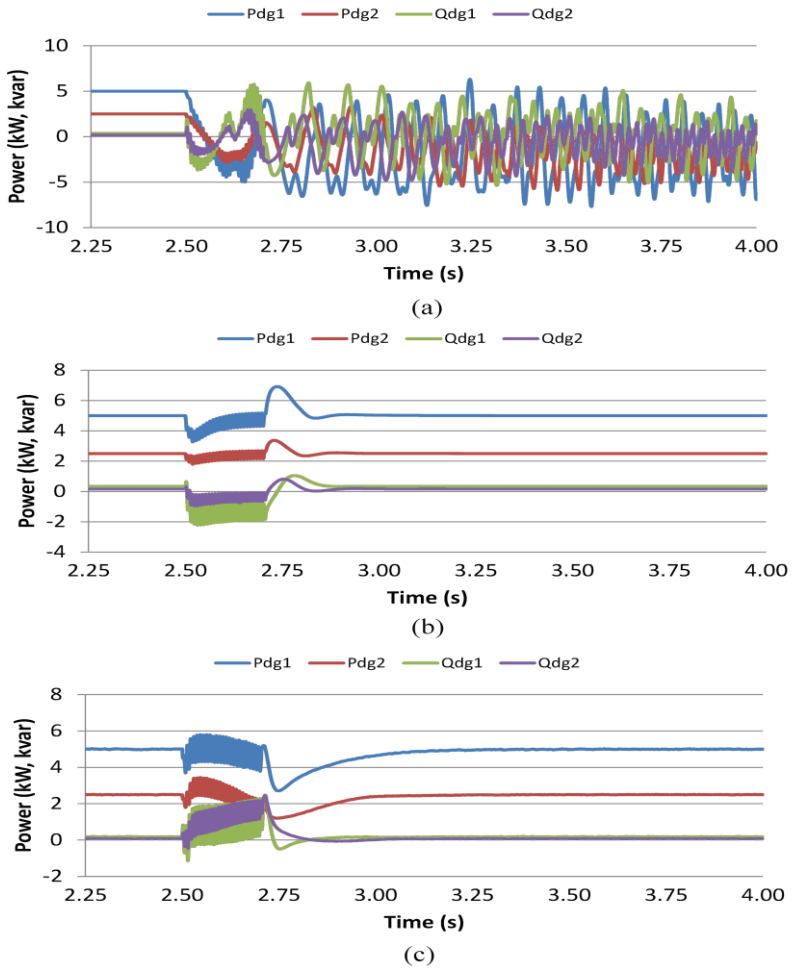

Fig. 4.8. Simulation of active and reactive power of grid-connected DG1 and DG2 in the event of a line-to-line fault. (a) Multiloop control VSG. (b) VSG with virtual impedance current limiting. (c) FS-MPC based VSG

On the other hand, the proposed FCS-MPC-based control is capable of peak current limiting. Furthermore, as shown in Fig. 4.9 (c), even under unsymmetrical condition, the MPC controller uses the measured voltage and current to find the optimal inverter switching state, which provides voltage and current as close as possible to the desired values. Hence, comparatively sinusoidal waveform of inverter current is produced. However, the steady-state current waveforms of FCS-MPC based system displays more ripples in comparison to its PWM counterparts.

4.4.2 Islanded Operation

For islanded mode, the load connected to the system is 6.6 kW+ 0.6 kVar. The other setting of the system is the exact same with the case of grid-connected mode except that now DGs are operating independently from the grid. Event of three-phase fault or line-A-to-line-B fault is conducted at 4s to 4.5s. Due to hardware restriction, the fault resistance was selected as 5Ω in the former case and 2.5Ω

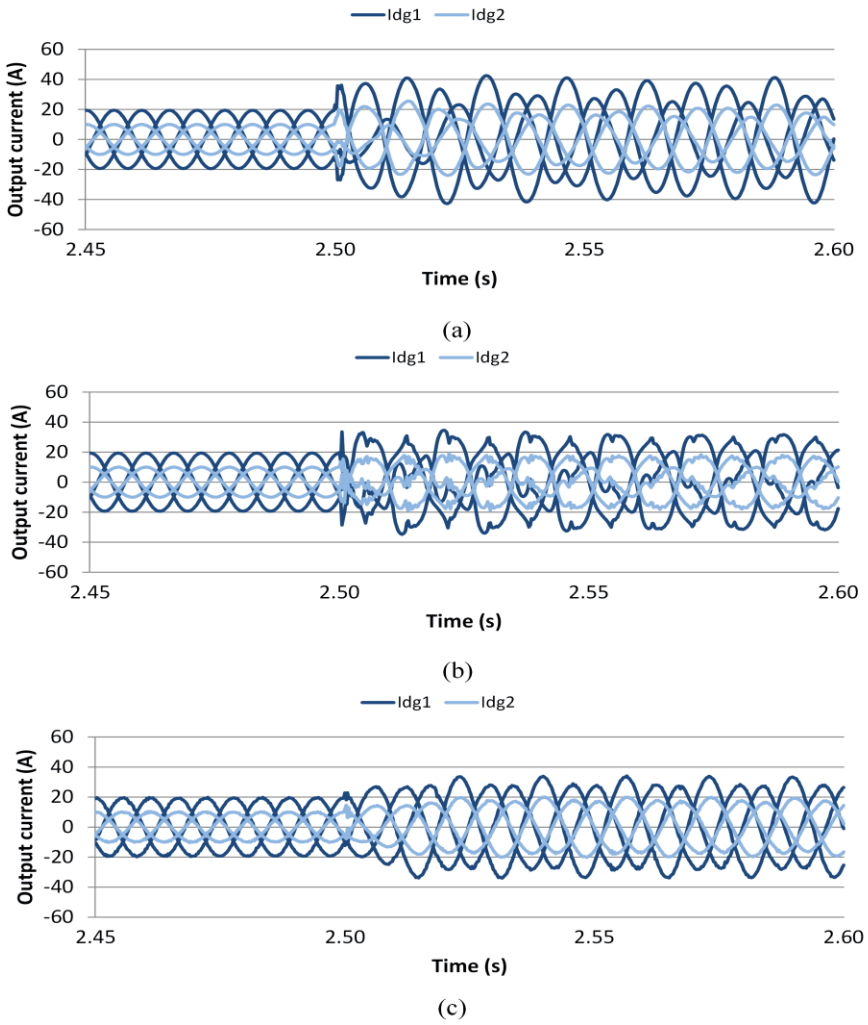

Fig. 4.9. Simulation of current waveforms of grid-connected DG1 and DG2 in the event of a line-to-line fault. (a) Multiloop control VSG. (b) VSG with virtual impedance current limiting. (c) FS-MPC based VSG

in the latter case. This corresponds to a voltage drop to around 0.65pu for the former and to 0.6-0.7pu for the latter case. Current waveforms of multiloop control during the event of fault are shown in Figs. 4.11 (a) and 4.13 (a). For the case of three-phase faults, overcurrent limiting ability can clearly be seen, as peak current is kept under 2 pu throughout the fault event. In the case of a line-to-line fault, although overcurrent can be prevented, the current becomes distorted, as the current command becomes oscillatory due to oscillating $\boldsymbol{v}_{dq}$ in the outer loop voltage control.

The active and reactive power waveforms are depicted in Fig. 4.10 (a) and 4.12 (a) for three-phase fault and line-to-line fault, respectively. Compared to the other two methods, the restoration of power control after fault event is slower in multiloop control, as the power oscillates for a short period before it settles. The active power-sharing in parallel connected inverters is done by managing an appropriate distance between angles of each inverter, which is determined by the VSG control part.

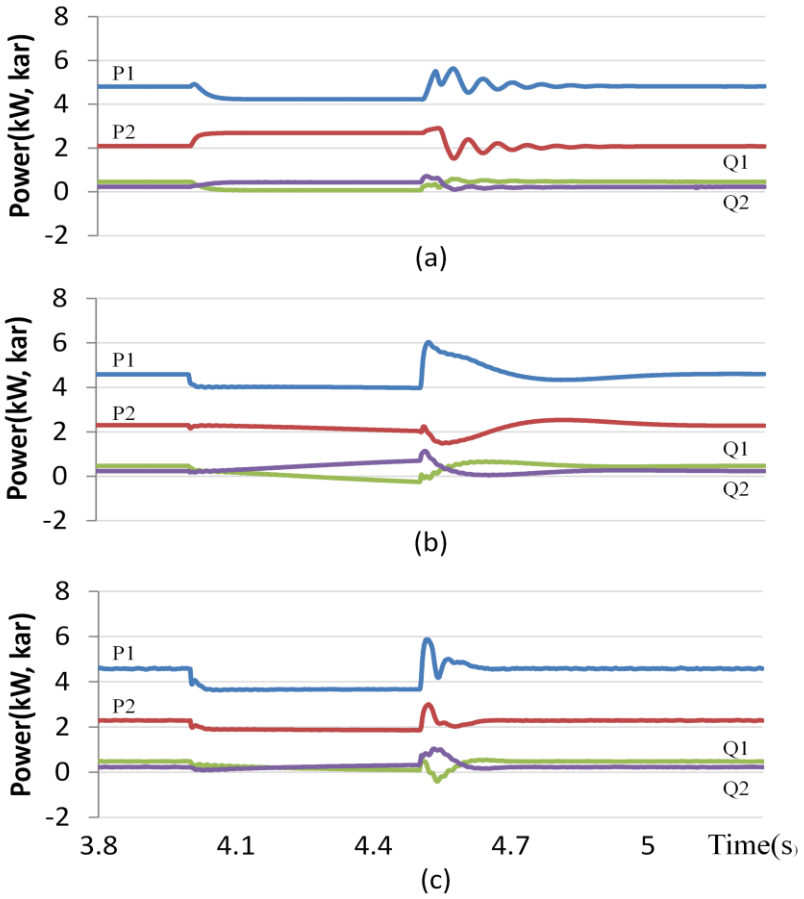

Fig. 4.10 Simulation of active and reactive power of islanded DG1 and DG2 in the event of a three-phase fault. (a) Multiloop control VSG. (b) VSG with virtual impedance current limiting. (c) FS-MPC based VSG

In the fault event, the power angle balance was disrupted and the two inverters need to restore their previous power angle distance after fault clearance. In multiloop control, however, power angle references from VSG are not applied directly to the inverter and got affected by quadrature axis components of the cascade control loop, which results in slow dynamic response and oscillation in active and reactive power. The active and reactive power restoration can become quicker if the sensitivity of the PI control in the outer voltage loop is increased. However, it will lead to more significant oscillation in current command during the fault event, and as a consequence, the distortion of current increases. Therefore, there is clearly a trade-off between distortion in current during disturbances and the ability to track power command in multiloop control. The oscillation of active and reactive power and distortion in current waveform, however, are reduced compared with the result in [15], since the nonlinearity-sensitive -PLL is removed from the multiloop.

The current and power waveforms of VSG with virtual impedance are illustrated in Figs 4.10 (b) – 4.13 (b). In the event of a three-phase fault (Fig. 4.10 (b) and Fig. 4.11 (b)), the control strategy is able to achieve an overcurrent-limiting. After the fault is cleared, *P* and *Q* gradually settle toward the

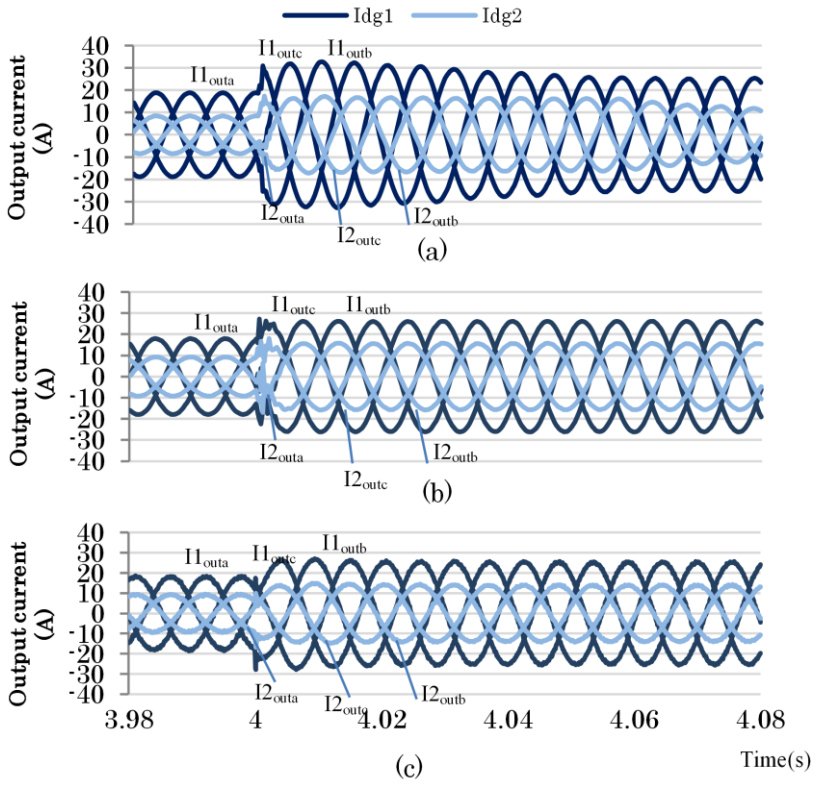

Fig. 4.11 Simulation of current waveforms of islanded DG1 and DG2 in the event of a three-phase fault. (a) Multiloop control VSG. (b) VSG with virtual impedance current limiting. (c) FS-MPC based VSG

steady-state values. The power restoration cannot be done immediately, as the increased virtual impedance cannot be entirely removed right after the fault clearance, and this impedance acts to oppose the change in current and also slows down power restoration. However, unlike multiloop control, there is no oscillation in active and reactive power during restoration.

In the case of unbalanced voltage sag (Fig. 4.12 (b) and 4.13 (b)), the output current becomes oscillatory due to the unsymmetrical condition of the fault. This causes distortion in the current waveform since the increased output impedance is calculated using the oscillated output current. As a result, output current becomes more oscillatory and the distortion will get amplified again when the new value of virtual impedance is calculated. The author tried to ease the influence of oscillated output current with a low pass filter. However, this will lead to low dynamic response in overcurrent detection and thus degrades the current limiting ability of the control, especially at the instance when the fault first occurs. In the worst-case scenario, where the output current oscillates across the $I_{thresh\text{-}old}$, the control will rapidly switch between normal and overcurrent mode, which might lead to a failure in overcurrent prevention or a much-distorted voltage and current waveforms. In order to avoid these problems, overcurrent limiting strategies without transition between normal mode and overcurrent mode is preferable in the case of an unsymmetrical fault. In DG2 the peak current exceeds

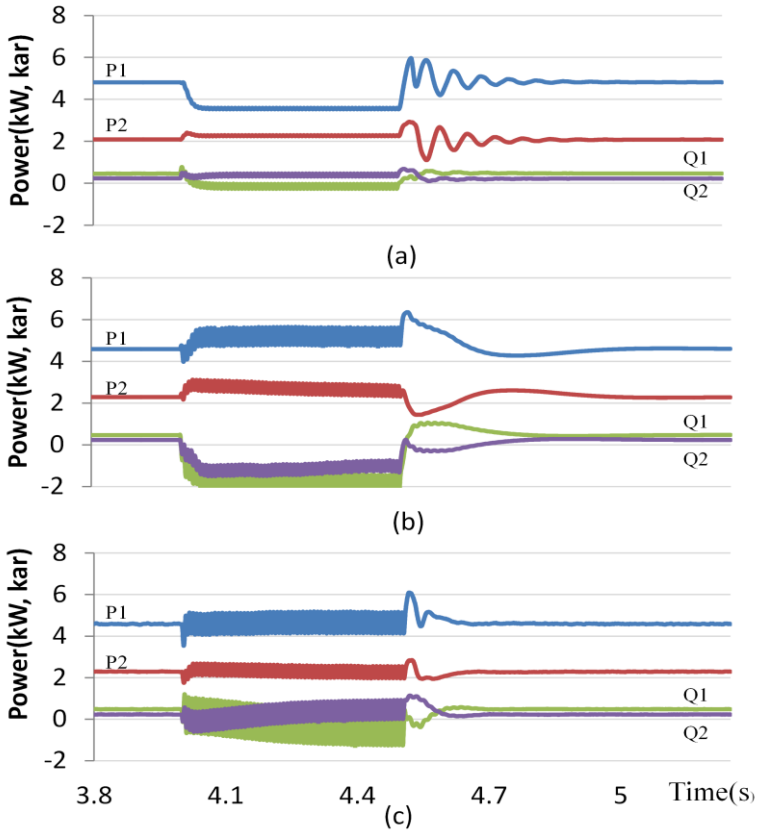

Fig. 4.12. Simulation of active and reactive power of islanded DG1 and DG2 in the event of a line-to-line fault. (a) Multiloop control VSG. (b) VSG with virtual impedance current limiting. (c) FS-MPC based VSG

the maximum allowed current regardless of the size of the limiting gain, as the amount of the drop in voltage command already exceeds the voltage command generated by VSG. Hence, the control failed to limit overcurrent.

The active and reactive power in the case of unbalance voltage sag is demonstrated in Fig. 4.12 (b). In this case, similar behavior as the three-phase fault case can be observed, as P and Q gradually settle to their values prior to the fault event.

The current waveforms of FS-MPC-based VSG are displayed in Fig. 4.11 (c) and 4.13 (c). The current limiting ability is confirmed for both types of faults. Moreover, in the case of unbalanced voltage sag, thanks to its current loop control in $\alpha\beta$-frame, the control shows a superior non-sinusoidal current suppressing capability than the other two methods, as distortions are mostly reduced. Fig. 4.13 (c) also displays that the unbalance in current is also restrained compared to multiloop control. The active and reactive powers are presented in Fig. 4.10 (c) and 4.12 (c). The restoration of P and Q after the fault clearance in the FS-MPC-based method is the quickest one out of the three methods, as both voltage and current control are used in power tracking simultaneously, and saturation of the current reference is avoided.

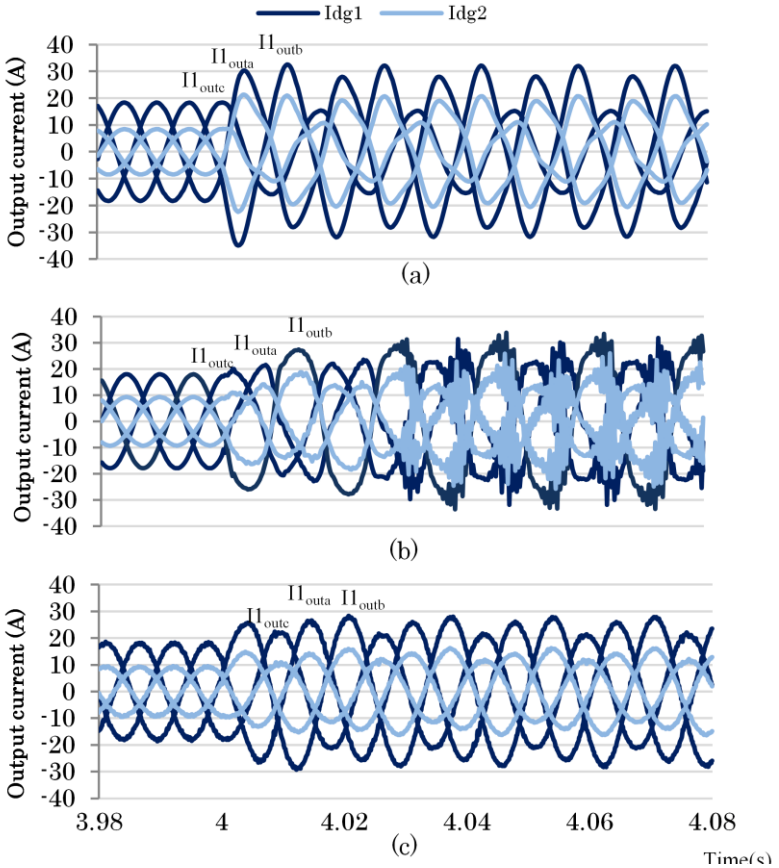

Fig. 4.13. Simulation of current waveforms of islanded DG1 and DG2 in the event of a line-to-line fault. (a) Multiloop control VSG. (b) VSG with virtual impedance current limiting. (c) FS-MPC based VSG

4.5 Experimental Verification and Discussion

The simulation results of the islanded-parallel DGs case are further verified by experimental results in the laboratory, illustrated in Fig. 4.14 and Fig. 4.15. The setting of the test circuit is the same as that of the simulation circuit depicted in Fig. 4.5, and the control parameters and the experiment scenario are also adopted from the simulations. Both inverters are controlled independently by a digital control unit Myway PE-Expert IV, and the presented data are internal variables of the control unit, which are recorded using the embedded function of PE-View X. This is a software interface of Myway PE-Expert IV. Additionally, HIOKI PW6001 Power analyzer was used to obtain FFT analysis data. By comparing the experimental results displayed in Fig. 4.16-4.20 to the simulation results displayed in Figs. 4.10-4.13, it can be concluded that all comments on simulation results still stand for the experimental results. The results of the current waveforms in the experiment are very similar to the waveforms in the simulations. On the other hand, the active and reactive power from experiment results differs a bit from simulations. The possible causes might be the difference between the

ideal DC sources of inverter in simulation, as opposed to the real DC sources in the experiment set-up. In the case of multiloop control, the power oscillation is reduced in experimental results compared with the simulation, as a low pass filter was used in the experiment to reduce noise from the measured signal. Nevertheless, the dynamic response of each control methods shows the same tendency in both simulation and experiment, for instances, after fault clearing, active and reactive pow-

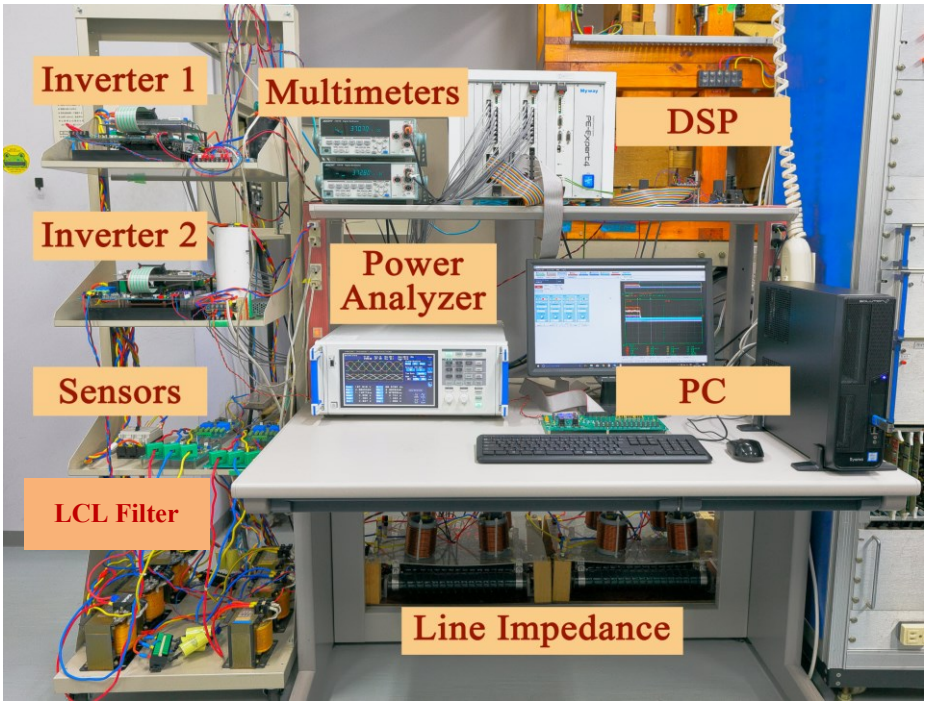

Fig. 4.14. Microgrid testbed for experimental verification.

Fig. 4.15. Photos of the load systems.

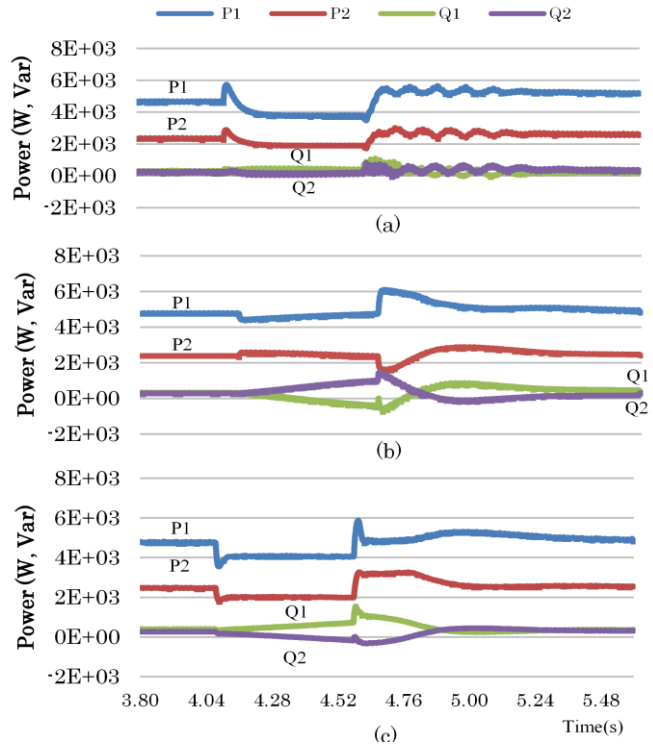

Fig. 4.16. Experiment results of active and reactive power of islanded DG1 and DG2 in the event of a three-phase fault. (a) Multiloop control VSG. (b) VSG with virtual impedance current limiting. (c) FCS-MPC based VSG

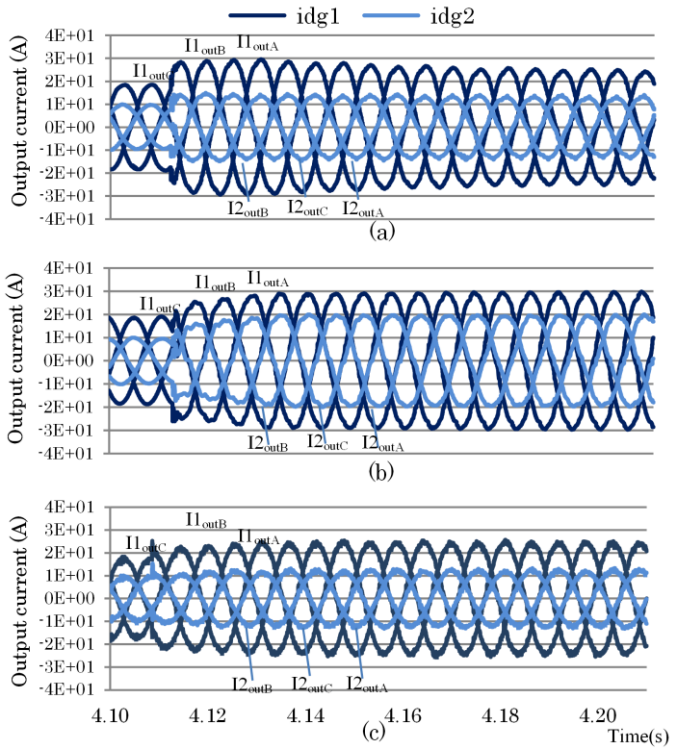

Fig. 4.17. Experiment results of current waveforms of islanded DG1 and DG2 in the event of a three-phase fault. (a) Multiloop control VSG. (b) VSG with virtual impedance current limiting. (c) FCS-MPC based VSG

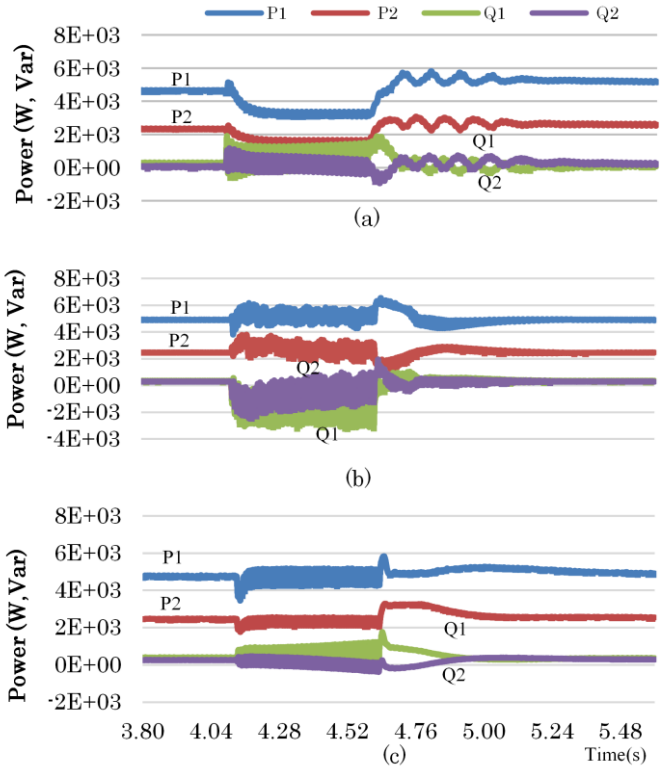

Fig. 4.18. Experiment results of active and reactive power of islanded DG1 and DG2 in the event of a line-to-line fault. (a) Multiloop control VSG. (b) VSG with virtual impedance current limiting. (c) FCS-MPC based VSG

er in multiloop control displays some oscillations, whereas FCS-MPC based VSG can restore power a little bit quicker than VSG with virtual impedance current limiting against balanced voltage sag.

The zoomed up of current waveforms in Fig. 4.17, and Fig. 4.19 are displayed in Fig. 4.20. Fig. 4.20(g)-20(i) also indicate that the current ripple is notably higher in FCS-MPC in steady-state. In Fig. 4.21, fast Fourier transform (FFT) analyses of phase-A-voltage and current waveforms of DG1 illustrate the harmonics of voltage and current under 100th order. The results confirm the previous discussion that the harmonic spectrum of FCS-MPC is dispersed compared to those of PWM-based methods. Although the broad harmonic spectrum cannot be removed in the proposed control scheme, the amount of harmonic from the 5th to the 100th order was kept only around 0.5% of the fundamental component. Additionally, a ratio of the total harmonic component from the 2nd order to the 100th order to the fundamental wave (THD) for each control scheme is also displayed in Fig. 4.21. It indicates that the multiloop control and the VSG with virtual impedance current limiting have THDs of around 2% for both voltage and current components, whereas the proposed control scheme has a slightly higher THDs around 3.5% and 3.2% for voltage and current components, respectively. Although the proposed control generates notably higher THDs than the other two methods, these numbers are within 5%, which is an acceptable level in power grids operation. Furthermore, the

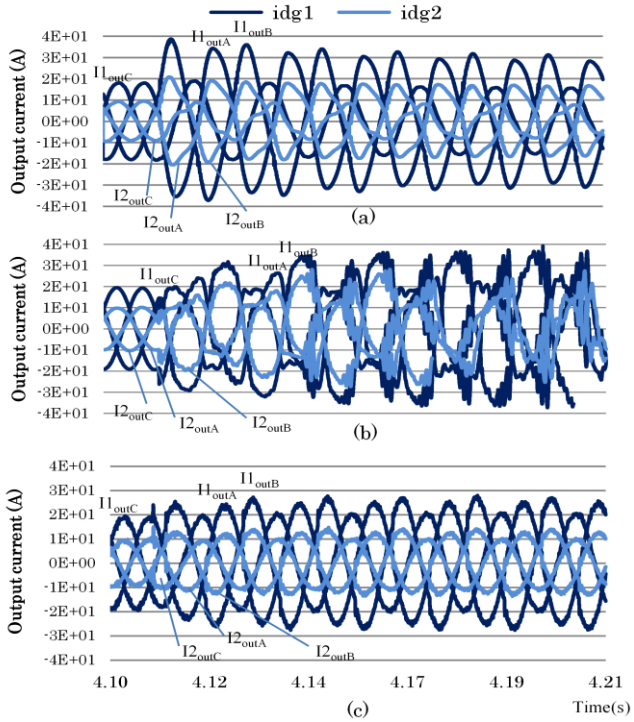

Fig. 4.19. Experiment results of current waveforms of islanded DG1 and DG2 in the event of a line-to-line fault. (a) Multiloop control VSG. (b) VSG with virtual impedance current limiting. (c) FCS-MPC based VSG

amplitude of harmonics in each order and sampling frequency of the inverter can be further reduced, if an increased number of virtual voltage vectors are applied as studied in [29]-[31]. This is especially evident in [30], where the effectiveness and performance of FS-MPC based method for a two-level grid-connected voltage source inverter is verified. In [32], by utilizing a high computational power FPGA and parallel computation, quasi-continuous sets of inverter voltage vectors can be generated. In this case, a sampling period and a harmonic spectrum comparable to PWM-based control are expected, as MPC utilizes a conventional space-vector-pulse-width-modulation (SVPWM) to generate inverter‘s switching signal. To avoid the high computational burden in MPC, strategies to significantly reduce calculation time for a high number of virtual voltage vectors are also proposed in [30]–[31]. Alternatively, the harmonic spectrum can be improved by utilizing optimized LCL filter design to attenuate both high and low order harmonics, as proposed in [33]–[34].

4.6 Conclusions

A comparative study between a FCS-MPC-based VSG control schemes, a VSG with virtual impedance current limiting, and a multiloop VSG control are presented for a three-phase inverter-interfaced DGs regarding their FRT-abilities. Results from simulations and experiments have been conducted to evaluate the performances of the proposed control in comparison with the existing control in both grid-connected and islanded operations.

For grid-connected operation, the multiloop VSG control does not have the fault-ride-through ability, as it failed to provide the power to the grid after the fault is cleared. In the case of VSG control with virtual impedance current-limiting, although it is capable of overcurrent limiting and can ride through fault, the controller generates a distorted current waveform when the disturbance is asymmetrical. The proposed control, on the other hand, is able to limit peak current, while providing comparatively sinusoidal current waveform regardless of the nature of the disturbances.

As for the islanded operation, in the event of a three-phase fault, the three control methods have the ability to limit over current and ride through fault. However, out of the three methods, FCS-MPC based VSG demonstrates the best control of active and reactive power after fault clearance. In the event of unbalanced voltage sag, the FCS-MPC-based control outperforms the other two methods, as it shows an ability to suppress unbalance and non-sinusoidal current. In contrast to that, VSG with virtual impedance current limiting failed to limit overcurrent in this case, whereas multiloop control suffers from poor active and reactive power control. Therefore, it is validated that the proposed FCS-MPC-based VSG control strategy possesses a superior current-limiting ability and FRT capability in comparison with other existing methods.

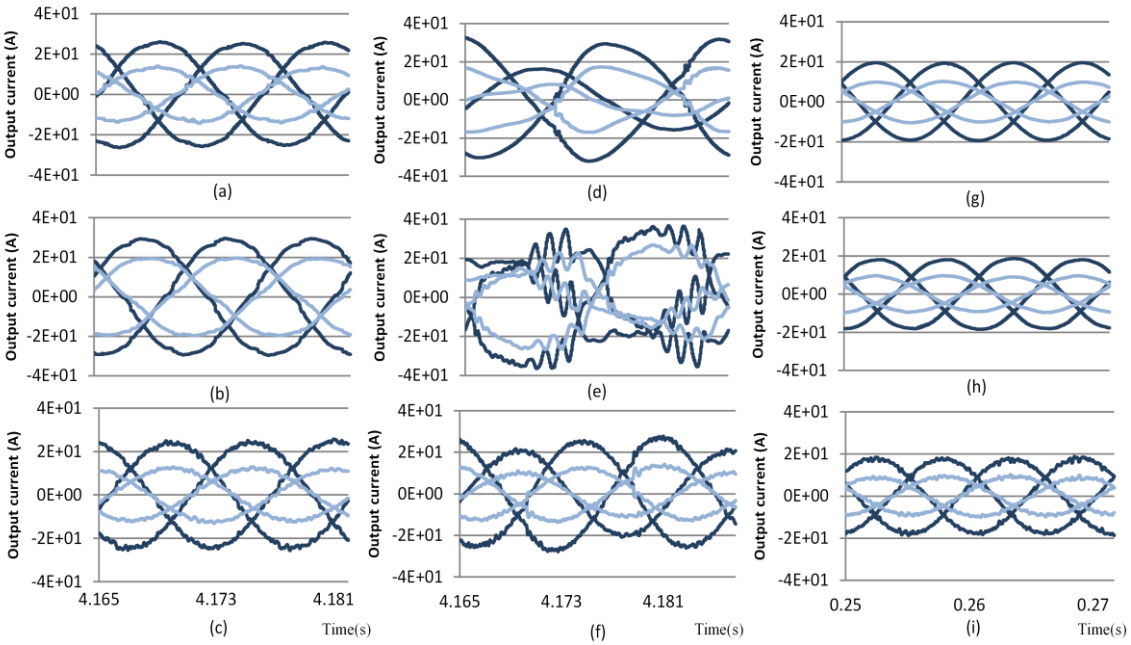

Fig. 4.20. Zoom-ups of the current waveform of DG1 and DG2

(a)-(c) in the event of a three-phase fault: (a) Multiloop control VSG. (b) VSG with virtual impedance current limiting. (c) FCS-MPC based VSG

(d)-(f) in the event of a line-to-line fault: (d) Multiloop control VSG. (e) VSG with virtual impedance current limiting. (f) FCS-MPC based VSG

(g)-(i) in steady-state: (g) Multiloop control VSG. (h) VSG with virtual impedance current limiting. (i) FCS-MPC based VSG

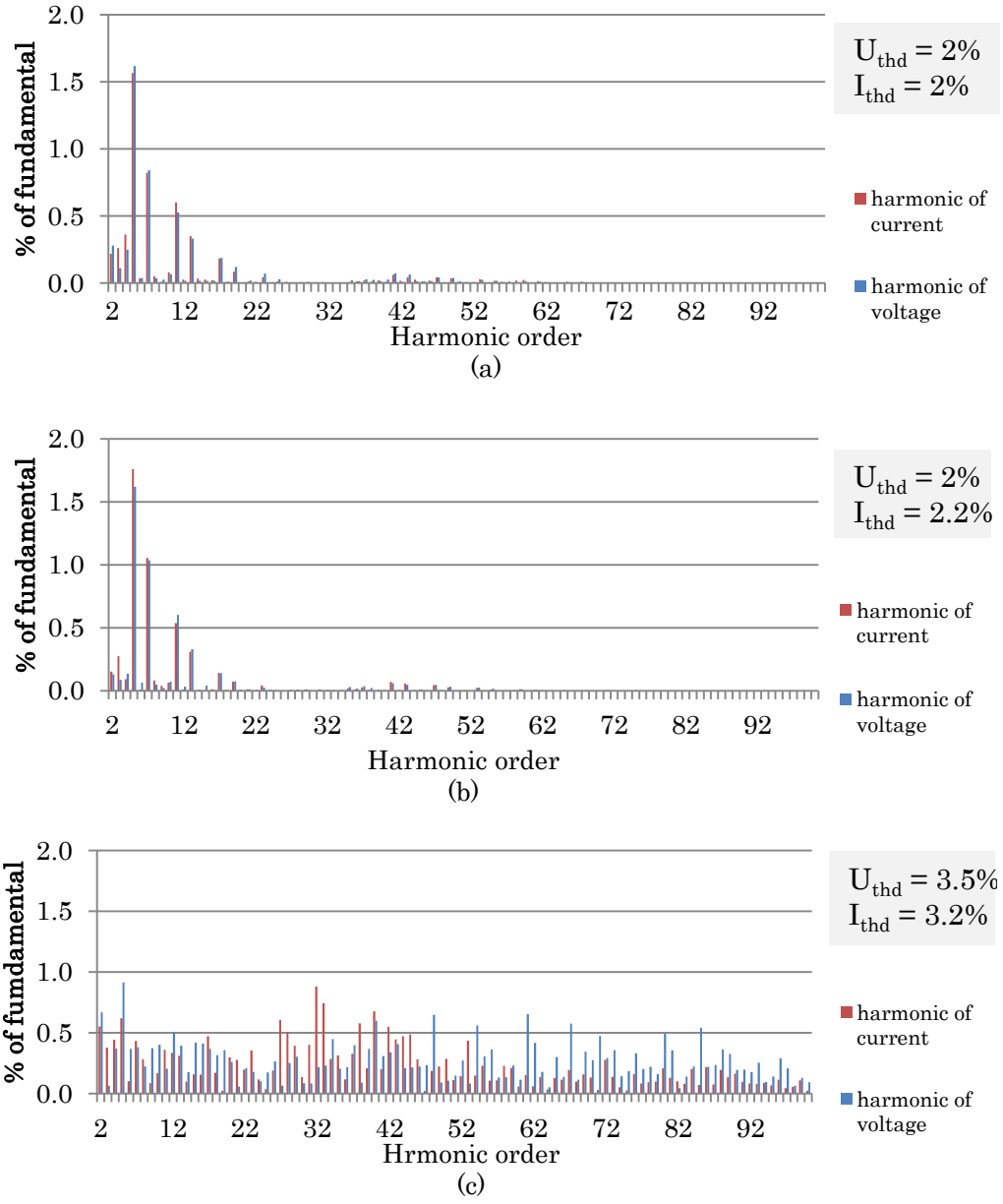

Fig. 4.21. FFT analysis of phase-A-voltage and current waveforms of inverter one (a) Multiloop control VSG. (b) VSG with virtual impedance current limiting. (c) FCS-MPC based VSG

References

[1] J. Driesen and K. Visscher "Virtual synchronous generators," *in Proc. 2008 IEEE Power Energy Soc. Gen. Meeting—Convers. Del. Elect. Energy 21st Century*, pp. 1–3.

[2] K. Sakimoto, Y. Miura, and T. Ise, "Stabilization of a power system including inverter type distributed generators by the virtual synchronous generator," *IEEJ Trans. Power and Energy*, vol. 132, no. 4, pp. 341–349, Apr. 2012.

[3] Q.-C. Zhong and G. Weiss, “Synchronverters: inverters that mimic synchronous generators,” *IEEE Trans. Ind. Electron*., vol. 58, no. 4, pp. 1259–1267, Apr. 2011.

[4] Q.-C. Zhong, P.-L. Nguyen, Z. Ma, and W. Sheng, “Self-synchronized synchronverters: inverters without a dedicated synchronization unit,” *IEEE Trans. Power Electron.*, vol. 29, no. 2, pp. 617–630, Feb. 2014.

[5] M. Guan, W. Pan, J. Zhang, Q. Hao, J. Cheng, and X. Zheng, “Synchronous generator emulation control strategy for voltage source converter (VSC) stations,” *IEEE Trans. Power Syst.*, vol. 30, no. 6, pp. 3093–3101, Nov. 2015.

[6] H. Wu, X. Ruan, D. Yang, X. Chen, W. Zhao, Z. Lv, and Q.-C. Zhong, “Small-signal modeling and parameters design for virtual synchronous generators,” *IEEE Trans. Ind. Electron*., vol. 63, no. 7, pp. 4292–4303, Jul. 2016.

[7] Japanese Grid-interconnection Code, JEAC 9701-2012, addendum-2012-No.1

[8] N. Bottrell, and T. Green, “Comparison of current-limiting strategies during fault ride-through of inverters to prevent latch-up and wind-up,” *IEEE Trans. Power Electron*, vol. 29, no. 7, pp. 3786–3797, 2013.

[9] Z. Shuai, W. Huang, C. Shen, J. Ge, and Z. J. Shen, "Characteristics and Restraining Method of Fast Transient Inrush Fault Currents in Synchronverters," *IEEE Transactions on Industrial Electronics*, vol. 64, no. 9, pp. 7487-7497, Sept. 2017.

[10] J. Liu, Y. Miura and T. Ise, "Power Quality improvement of microgrids by virtual synchronous generator control," *2016 Electric Power Quality and Supply Reliability (PQ)*, Tallinn, 2016, pp. 119-124.

[11] J. Alipoor, Y. Miura and T. Ise, "Voltage sag ride-through performance of Virtual Synchronous Generator," *2014 International Power Electronics Conference (IPEC-Hiroshima 2014 - ECCE ASIA)*, Hiroshima, 2014, pp. 3298-3305.

[12] A. Perera, "Virtual Synchronous Machine-based Power Control in Active Rectifiers for Micro Grids," MSc. Thesis, Norwegian University of Science and Technology, Trondheim, Norway, July 2012

[13] S. D'Arco, J. A. Suul, and O. B. Fosso, "Automatic Tuning of Cascaded Controllers for Power Converters Using Eigenvalue Parametric Sensitivities," *IEEE Transactions on Industry Applications*, vol. 51, no. 2, pp. 1743-1753, March-April 2015.

[14] A. D. Paquette and D. M. Divan, "Virtual Impedance Current Limiting for Inverters in Microgrids With Synchronous Generators," *IEEE Transactions on Industry Applications*, vol. 51, no. 2, pp. 1630-1638, March-April 2015.

[15] J. Jongudomkarn, J. Liu and T. Ise, “Comparison of Current-Limiting Strategies of Virtual Synchronous Generator Control during Fault Ride-Through,” *IFAC-PapersOnLine*, vol. 51, issue 28, 2018, pp. 256-261.

[16] W. Zhang, J. Rocabert, J.I. Candela, P. Rodriguez, “Synchronous Power Control of Grid-Connected Power Converters under Asymmetrical Grid Fault,” *Energies* 2017, vol. 10, pp. 950.

[17] M. S. Moon and R. W. Johnson, “DSP control of UPS inverter with overcurrent limit using droop method,” in *Proc. 30th IEEE PESC*, 1999, vol. 1, pp. 552–557.

[18] S. Barsali, M. Ceraolo, P. Pelacchi, and D. Poli, “Control techniques of dispersed generators to improve the continuity of electricity supply,” in *Proc. Power Eng. Soc. Winter Meet.*, New York, NY, USA, Jan. 27–31, 2002, pp. 789–794.

[19] J. Jongudomkarn, J. Liu, and T. Ise, "Virtual Synchronous Generator Control with Reliable Fault Ride-through Capability by Adopting Model Predictive Control," *2018 International Power Electronics Conference (IPEC-Niigata 2018 -ECCE Asia)*, Niigata, Japan, May 2018, pp. 3902-3909.

[20] A. D. Paquette and D. M. Divan, "Virtual Impedance Current Limiting for Inverters in Microgrids With Synchronous Generators," *IEEE Transactions on Industry Applications*, vol. 51, no. 2, pp. 1630-1638, March-April 2015.

[21] J. Jongudomkarn, J. Liu, and T. Ise, “Comparison of Current-Limiting Strategies of Virtual Synchronous Generator Control during Fault Ride-Through,” *IFAC-PapersOnLine*, vol. 51, issue 28, 2018, pp. 256-261.

[22] V. Blasko and V. Kaura, "A new mathematical model and control of a three-phase AC-DC voltage source converter," *IEEE Transactions on Power Electronics*, vol. 12, no. 1, pp. 116-123, Jan. 1997.

[23] C. Bajracharya, M. Molinas, J. A. Suul, and T. M. Undeland, “Understanding of tuning techniques of converter controllers for HVDC,” in *Proc. NORPIE*, Helsinki, Finland, Jun. 9–11, 2008, pp. 1–8.

[24] W. Leonhard, *Control of Electrical Drives*. Heidelberg, Germany, Springer-Verlag, 1985.

[25] J. M. Guerrero, J. Matas, L. G. de Vicuna, M. Castilla, and J. Miret, “Decentralized control for parallel operation of distributed generation inverters using resistive output impedance,” *IEEE Trans. Ind. Electron.*, vol. 54, no. 2, pp. 994–1004, Apr. 2007.

[26] J. He and Y. W. Li, “Analysis, design, implementation of virtual impedance for power electronics interfaced distributed generation,” *IEEE Trans. Ind. Appl.*, vol. 47, no. 6, pp. 2525–2538, Nov./Dec. 2011.

[27] C. A. Plet and T. C. Green, “A method of voltage limiting and distortion avoidance for islanded inverter-fed networks under fault,” in *Proc. EPE*, Birmingham, U.K., Aug. 30–Sep. 1, 2011, pp. 1–8.

[28] J. Liu, Y. Miura, H. Bevrani, and T. Ise, “Enhanced virtual synchronous generator control for parallel inverters in microgrids,” *IEEE Trans. Smart Grid*, vol. 8, no. 5, pp. 2268–2277, Sep. 2017.

[29] S. Vazquez et al., "Model Predictive Control with constant switching frequency using a Discrete Space Vector Modulation with virtual state vectors," 2009 *IEEE International Conference on Industrial Technology*, Gippsland, VIC, 2009, pp. 1-6.

[30] H. Moon, J. Lee, and K. Lee, "A Robust Deadbeat Finite Set Model Predictive Current Control Based on Discrete Space Vector Modulation for a Grid-Connected Voltage Source Inverter," *IEEE Transactions on Energy Conversion*, vol. 33, no. 4, pp. 1719-1728, Dec. 2018.

[31] J. Lee, J. Lee, H. Moon, and K. Lee, "An Improved Finite-Set Model Predictive Control Based on Discrete Space Vector Modulation Methods for Grid-Connected Three-Level Voltage Source Inverter," *IEEE Journal of Emerging and Selected Topics in Power Electronics*, vol. 6, no. 4, pp. 1744-1760, Dec. 2018.

[32] Z. Ma, S. Saeidi, and R. Kennel, "FPGA Implementation of Model Predictive Control With Constant Switching Frequency for PMSM Drives," *IEEE Transactions on Industrial Informatics*, vol. 10, no. 4, pp. 2055-2063, Nov. 2014.

[33] J. Xu, S. Xie, and J. Kan, "*LCL*-filter design for grid-connected inverter to suppress grid-induced low-order current harmonics," *2015 IEEE Energy Conversion Congress and Exposition (ECCE)*, Montreal, QC, 2015, pp. 1178-1183.

[34] Yong-Jung Kim and H. Kim, "Optimal inductance ratio of *LCL* filter for grid-connected inverters considering with low order harmonics," *IECON 2016 - 42nd Annual Conference of the IEEE Industrial Electronics Society*, Florence, 2016, pp. 2355- 2360.

Chapter 5
Implementation of Multivariable FCS-MPC Based Virtual Synchronous Generator Control for Indirect Boost Matrix Converter-interfaced DGs

5.1 Introduction

AC/AC converter can broadly be found in standard industrial applications such as adjustable speed motor drives and power quality conditioners. Among them, the applications in distributed generation (DG) with variable ac-source using a permanent magnet synchronous generators (PMSGs), such as wind turbines, hydrokinetic turbines, and gas engine, have recently attracted a lot of attention from power engineers. Currently, the conventional back-to-back (B2B) converter [1]–[3] is the preferred choice for interfacing decentralized sources and utility distribution grid. However, bulky and lifetime-limited dc-link electrolytic capacitors are still often considered as a disadvantage of B2B converters. Hence, matrix converters (MCs) [4]–[17] are commonly investigated as a possible alternative to B2B converters since only a small or no dc-link capacitor is involved in the MCs topology. This is especially beneficial for applications where volume and weight restrictions are required. Nevertheless, the downside of MCs is that any change in the power command must be compensated by the energy stored in the DG unit itself, unlike in the case of the B2B converter, where the dc-link capacitor provides short-time energy and decouples the rectifier and inverter stages. Therefore, the control schemes for MC are more complex.

The MCs can be typically categorized into two types [4]: conventional direct matrix converters (DMCs) and indirect matrix converters (IMCs). Conventionally for a three-phase to three-phase conversion, a direct matrix converter utilizes nine bidirectional transistor-switches to establish a direct connection between the input and the output. Such an arrangement provides full bidirectional power flow, which is not useful for DGs, where power is only flowing from the sources to the distribution grid and thus causing a surplus of transistor switches [18]. The IMCs, on the other hand, can be simplified to reduce the number of transistor switches if a unidirectional power flow control is utilized. This topology is also known as sparse matrix converters (SMCs) [11]–[13]. Nevertheless, both SMSs and general DMCs have a low voltage gain, which is a limiting factor for a grid interfaced with DGs. This is notably the case for a connection between the utility and variable source voltages such as a PMSG-based energy conversion system driven by a wind turbine or gas engine, as these variable sources operate in a variable

speed mode, during which a varying voltage ranged from a low voltage to the PMSG rated voltage is generated. Therefore, a number of methods to increase the voltage gain have been proposed in the literature. The strategy can be done either in the modification of modulation strategies, as suggested in [14], or in the modification of the topology by adding more components to the virtual dc-link, as presented in [15]–[16]. Nevertheless, these methods can cause other disadvantages to the system. For instance, high filter requirements are needed for the given method in [14] due to higher input current THD, and the adding of passive components will increase overall system losses.

Alternatively, references [17] and [18] proposed the implementation of a reverse power flow operation of IMCs to generate a voltage-boost property. This configuration is an attractive solution for DG applications as it achieves a voltage gain larger than 1.4 just by reversing the order of the IMC to have a current source converter at the grid side and a voltage source converter at the side of the power source. It will be termed as an indirect boost matrix converter (IBMC) in this paper. Although the advantages of IBMC topology are clearly noticeable, the existing control methods are almost directly adopted from IMCs with conventional topology. Therefore, some shortcomings still exist, for instance, the resonance phenomenon of output CL-filter caused by the generation of low order harmonics components. This resonance may profoundly disturb the output current [8], so that it usually requires the addition of a passive damping resistor at the grid interfacing side [17], [18]. The existing modulation methods also only utilize the information of the phase angle to control the CSI side, and the amplitudes of output values cannot be regulated directly due to the fact that zero current vectors are not be used in the CSI side of IBMC [17], [18]. Thus it is challenging to apply active damping with such a control method. Another shortcoming of the existing control method lies in the fact that the existing control schemes are grid-following controls, which are only capable of operation in the grid-connected mode. Although a control scheme for islanded operation is proposed in [18], it faces a challenge of managing the transition of control mode between grid-connected and islanded operation. Furthermore, grid-following controls do not actively control their output frequency to support grid frequency stability. This is an essential topic for the future grid, where DGs are highly penetrated because, unlike synchronous generators (SGs), DGs lack rotating inertia.

One of the highly-rated solutions for these problems is the implementation of a virtual synchronous generator (VSG). The results of the past research works have clearly demonstrated that the VSG-based DGs can solve issues related to frequency deviations, and also capable of islanded operation [19]–[27]. However, the referred VSG controls are typically designed for a system with energy storage elements such as the B2B converter-interfaced system, as the inertial power of the referred VSG controls is provided by this storage element. Therefore, it is challenging to implement these VSG controls in a system without a dc-link energy storage element, such as the IBMC-interfaced DG. Without the energy storage element to draw a short-time power from, the controller needs to be able to dispatch the power directly from the input source in order to support the frequency stability of the grid. Furthermore, the integration of VSG control will further complicate the modulation of IBMC, which is already complicated due to the coupling between input control and output control.

As discussed in Chapter 2, finite control set model predictive control (FCS-MPC) has emerged over the last few years as an attractive alternative for the control of power electronics applications since it offers several benefits including simple multivariable control, the possible inclusion of constraints, straightforward control law, and fast dynamic response [30]. As for DGs, a number of control solutions based on FCS-MPC appeared in the literature [31]–[36]. Among these, the multivariable FCS-MPC-based VSG for VSI proposed in [36] shows high compatibility between FCS-MPC and VSG. In addition to an integration of inertia support feature, the FCS-MPC-based control scheme utilizes a simultaneous control of both voltage and current of the output *LCL*-filter, to provide a fault-ride-though ability, and to restrain the resonant energy oscillation between the inductances and the capacitances, which will occur if either one of the filter voltage or the filter current is solely controlled. This performs an alternative method to damp the filter resonance without a dedicated active damping part in the control algorithm [36]–[39].

The FCS-MPC constitutes a promising approach for implementation of VSG control-based IBMC compared with standard schemes because the FCS-MPC allows several control objectives to be fulfilled simultaneously by utilizing the system model and the real-time values of the system to determine the optimized converter's physical switching states directly. This grants the predictive controller significant advantages over the existing PWM-based methods, as it is capable of regulating the amplitudes of output values without employing zero current vectors. Therefore, the FCS-MPC is more suitable for the implementation of VSG controls, which govern the reactive output power via the regulation of output voltage amplitude. Furthermore, with the real-time variables of physical dc-link used in system model prediction, considerations of the complicated coupling between rectifier and inverter to find the mean values of the dc-link variables can be removed from the control algorithm as shown in the studies of FCS-MPCs for conventional motor/load drive IMC [40]–[42]. Taking into account the flaws of the existing method, such as the usage of a grid-following strategy and the requirement of a passive damping circuit, a novel VSG control based on the FCS-MPC is proposed to improve the performance of the IBMC-based DG. First, thanks to the adoption of the VSG strategy, the ability to operate in both grid-connected and islanded modes is achieved, while the controller is capable of dispatching the inertial power directly from the input sources, and is able to regulate the output reactive power through the manipulation of the output voltage. Furthermore, active filter resonance damping is provided by the multivariable control of capacitor voltage and inductor current of the output CL-filter.

The rest of this chapter is organized as follows. In Section 5.2, the topology of IBMC and its existing control methods are discussed. The shortcomings of the control method under investigation are analyzed and verified with simulation results shown in this section. The novel FCS-MPC for IBMC based on VSG control is proposed in Section 5.3. In Section 5.4, the performance of the proposed control scheme is verified by simulation results along with discussions to highlight its advantages. Experimental verification is then conducted in a scale-down manner in Section 5.5 to validate the results of the simulation study. Finally, this chapter is concluded in Section 5.6.

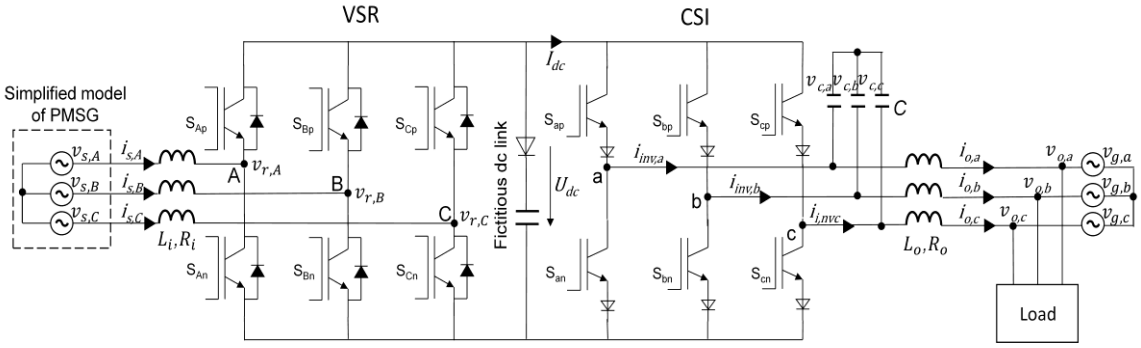

Fig.5.1 Topology of indirect boost matrix converter

5.2 Indirect Matrix Converter Topology

Adopted from [18], a topology of unidirectional IBMC is illustrated in Fig. 5.1. The converter consists of twelve power transistor switches. Among these, six switches have antiparallel diodes and are arranged as a front-end voltage source rectifier (VSR). The other six switches have series diodes for forming a rear-end current source inverter (CSI). This topology clearly differs from conventional IMC, where current source rectifier (CSR) and VSI are utilized. This reversed configuration allows the IBMC to have boost property. Nevertheless, according to [18], a clamped diode in series with a small film capacitor termed as "fictitious dc-link" is required at the physical link between VSR and CSI as a mean to maintain dc-voltage and suppress its spike.

This dc-link capacitor is vital for IBMC because unlike the CSR of conventional IMC, where null states are never used, VSR utilizes zero voltage vectors, during which all the upper or lower switches of the VSR are turned on, and the dc-link current becomes zero. As a consequence, no dc current is supplied to the CSI, and thus all switches in the CSI are turned off. Without the DC-link capacitor, this will result in DC-link voltage becoming zero, which should be avoided as it can cause short-circuits between output filter capacitors and antiparallel diodes in the VSR side. However, the presence of the DC-link capacitor means that DC-link voltage can be discharged via the CSI to the output filter capacitances, generating a sizeable circulating current and distorting the output current of IBMC. In order to avoid this, the DC-link capacitor should be so small that the amount of the discharging current is ignorable. Nevertheless, the voltage spikes will not be sufficiently suppressed in this case. Alternatively, a clamping diode could be added in series with the capacitor, as shown in Fig. 5.1, to prevent the discharging, thus allowing a larger DC-link capacitor to be used.

5.3 Review of Existing Control Methods

The modulation of CSI and VSR studied in this work are adopted from [18]. As mentioned previously, the controllers of the CSI and VSR have to be dependently implemented since there is no dc-link capacitor to decouple the two stages. The modulation of each stage will be explained as follows.

5.3.1 CSI Side

The objective of modulation in the CSI side is to keep the dc-link voltage commutating between the largest and the second-largest positive line-to-line grid voltages. In this method, none of the null states are used to avoid circulating current between the fictitious dc link and the shorted phase-leg. This leaves us with only six active stages, where only one of the upper (bottom) switches and one of the bottom (upper) switches remains ON at all instants. All other switches remain off. These states can be described with the corresponding ON switches and placement on the space vector diagram, as illustrated in Fig. 5.2. The reference IMC output current can be synthesized by making use of the two adjacent active current vectors from the possible six active vectors (SC1-SC6), which divide the space vector into six sextants, as illustrated in Fig. 5.2. The current reference phasor is set to follow grid phasor, thus, if the grid phasor θ_g is located in one of the sextants, two nearest space vector to the current reference phasor will be chosen for reproducing the references. Even so, if we consider Fig. 5.2, it can be seen that when the IMC output current is generated from only two active current vectors without the null vectors, the amplitude of the current cannot be adjusted, and only the phase angle of the output current can be regulated. Under this condition, only the current vectors on the hexagon boundary that is depicted in Fig. 5.2 (a) are generated. Therefore, the corresponding active duty ratios (d_1 and d_2) for the CSI can be determined with the phase angles θ_a, θ_b and θ_c alone. Giving the fact that $\cos\theta_a + \cos\theta_b + \cos\theta_c = 0$, d_1 and d_2 can be eventually determined for the example of sextant 1 as follows:

$$d_1 = -\cos\theta_b/\cos\theta_a\,, d_2 = -\cos\theta_c/\cos\theta_a \tag{5.1}$$

Nevertheless, since the amplitude of the IMC output current cannot be adjusted, in order to create a sinusoidal current, the modulation is designed to generate a dc-link current with sinusoidal distributed amplitude through modulation in VSR. This can be achieved by applying a sinusoidal distributed average dc-link voltage during the calculation of the VSR side's modulation index. This voltage can be determined as follows.

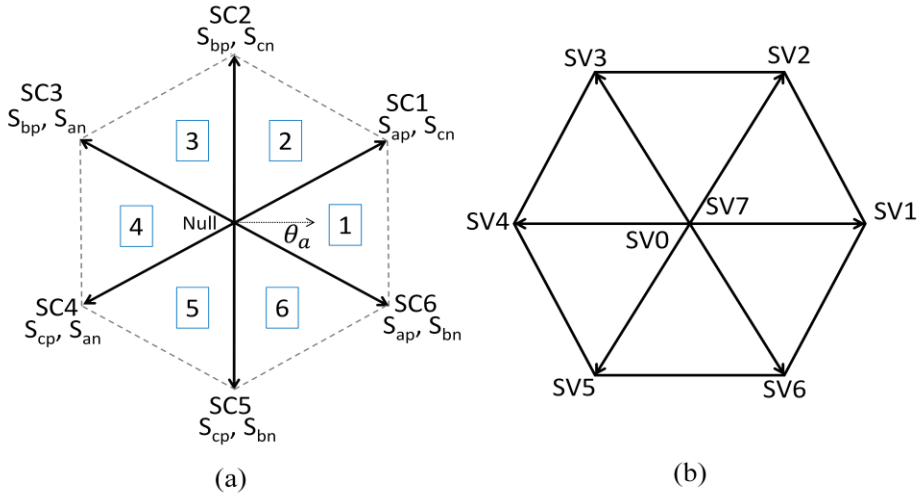

Fig.5.2 Space vector representations of (a) CSI and (b) VSR

$$V_{DC(av)} = \begin{cases} \frac{3V_{om}}{2|m_{max}|} cos\emptyset_0, & \text{for sextants} = 1,3,5 \\ \frac{3V_{om}}{2|m_{min}|} cos\emptyset_0, & \text{for sextants} = 2,4,6 \end{cases} \quad (5.2)$$

where $m_{max} = max(\cos\theta_a, \cos\theta_b, \cos\theta_c)$, $m_{min} = min(\cos\theta_a, \cos\theta_b, \cos\theta_c)$, and $\emptyset_0$ is the output power factor angle. Because of (2), the resulting average amplitude of dc-link current ($i_{DC(av)}$) would vary in inverse proportion to $v_{DC(av)}$, which results in $I_a \approx kcos\theta_a$ that resembles sinusoidal current. This relation can also be applied for computation of the output currents I_b and I_c.

5.3.2 VSR Side

For the control of the voltage source rectifier side, space vector modulation (SVM) is implemented to produce the desired input current at unity power factor. The VSR switching sequence must utilize zero space voltage vectors (SV0 and SV7) to boost the input voltage (i.e., using the input inductance). The zero voltage vectors are performed by turning ON either all upper ($\boldsymbol{S_{ap}}, \boldsymbol{S_{bp}}, \boldsymbol{S_{cp}}$) or all lower switches ($\boldsymbol{S_{an}}, \boldsymbol{S_{bn}}, \boldsymbol{S_{cn}}$) of the VSR. The reference voltage vector is synthesized by making use of the zero voltage vectors and two adjacent active vectors of the possible six active vectors (SV1 – SV6). Additionally, compensation for the varying dc-link voltage has to be executed to generate a DC-link current with sinusoidal distributed amplitude. Hence, the modulating reference $\boldsymbol{d_A}$ for phase A can be written with the following equation.

$$d_A = \frac{v_A + V_{off}}{V_{DC(av)}/2} \quad (5.3)$$

where v_A, v_B and v_C represent three-phase input voltage references before normalization. V_{off} is the triple order harmonic offset commonly added to gain a 15% increase in modulation index [9].

Finally, coordination between the commutation of CSI and VSR modulations is required to avoid an error. For instance, CSI needs to commutate when the zero voltage vector is applied in VSR. This can be done by comparing a standard triangular carrier with d_1 from (5.1) and setting their intersecting point at the commutating point for CSI. Then the sampling period T_s of CSI will be divided into d_1T_s and d_2T_s. These two periods are used as modulation periods of VSR, within which the commutations of VSR will be executed. Thus commutation of CSI will occur at the start and the end of the modulation period d_1T_s and d_2T_s during which the zero voltage vectors are applied. More explanations can be found in [10].

5.3.3 Analysis of Control Algorithm for DG Applications

Despite the effort to compensate dc-link current through modulation in VSR**,** the modulation alone cannot ideally generate the desired dc-current amplitude and low harmonic order components are generated in the CSI side. These harmonics seem to be amplified in the control of IBMC since the IBMC is connected to voltage sources in both input and output sides as opposed to conventional RL-load drive

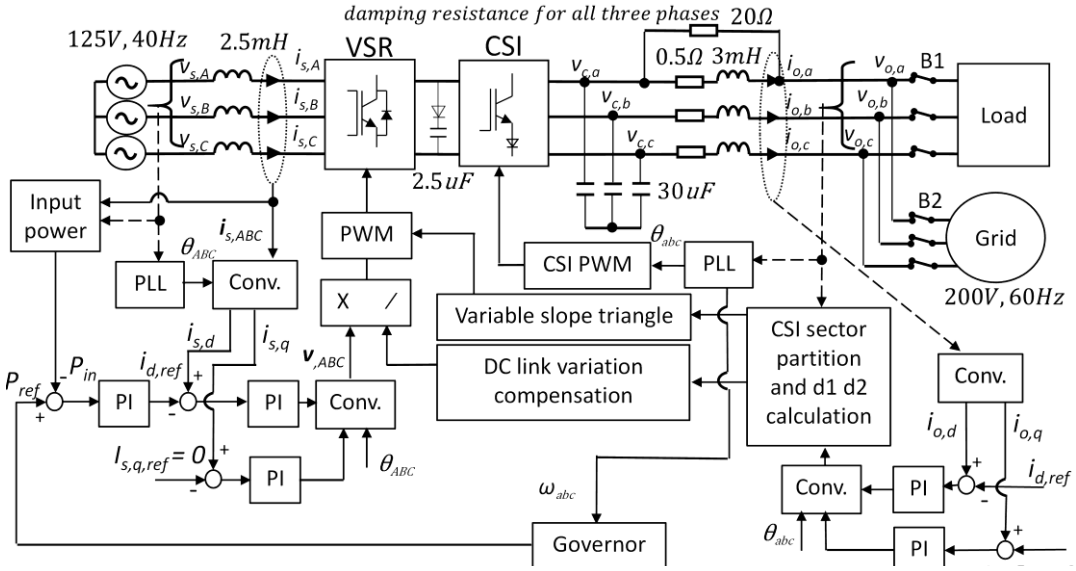

Fig. 5.3 The control diagram of the existing PWM-based method

IMC, where voltage source only exists at the input side. The differences in frequencies, phase angles, or amplitudes between input and output voltage sources are bound to affect the generated dc-link current. Hence low order harmonic distortion can be observed in the generated output current waveforms. This low harmonic order can excite *CL*- filter resonance in the grid side of IBMC, which causes the output current to be highly distorted, as shown in [8]. In order to suppress the oscillation caused by filter resonance, it requires the addition of a passive damping resistor at the grid interfacing side, as suggested in [17], [18]. Nevertheless, it will cause high power losses in the converter. Although various active damping strategies to eliminate distorted input current of *RL*-drive IMC are proposed in the literature [28]–[29], which could be modified for the suppression of distorted output current of IBMC, they require a complicated modification in control algorithm and higher switching frequency, which causes higher switching losses. Hence, similarly to [17], [18], a damping resistor is added to the circuit, as shown in Fig. 5. 3 to deal with resonance issues in this work.

The objective of DGs in grid-connected operation is to track the dispatch power command, which is realized by the control diagram shown in Fig. 5.3. The current command $i_{d,ref}$ of VSR is obtained via PI control of the outer active power control loop. The active power command is set at 5 kW. For unity power factor operation, $i_{s,q,ref}$ is set to zero. The computed current reference is subsequently tracked by the measured source current $i_{s,dq}$ by feeding their error to a PI controller. As for the CSI, three-phase modulation references are obtained through *dq/abc* transformation after the PI control processing, as shown in Fig. 5.3. The same current command $i_{d,ref}$ as used in the VSR side is employed and for unity power factor operation, $i_{o,q,ref}$ is set to zero. However, only the phase angle information is used for the CSI modulation, as shown in (1). The other block diagrams, shown in Fig. 5..3, are well described in [17], [18].

The modulation index of the CSI is fixed at 1 since only the phase angle information is used. This arrangement is suitable for IMC without reversed configuration, where modulation of CSR is set to the

maximum so that the power can be designed by the VSI side's control and the load. The output power of the IBMC, on the other hand, is managed by the input control and is not affected by the output network. This implies that the control algorithm for the IBMC is not suitable for islanded operation, where the balance between DG's power and load power needs to be maintained. A different control scheme is suggested in [18] for the islanded operation of the IBMC, which utilizes the measured output voltage drop in order to determine the power command for the VSR controller according to the relationship of $P = V^2/R$. However, this method requires control modes changing between grid-connected and islanded operations. Furthermore, the relationship between output voltage drop and output power can only be accurately deployed if no reactive load exists in the islanded network.

In order to study the performance of the existing PWM-based method for IBMC, the test circuit depicted in Fig. 5.3 is set to simulate in PSCAD/EMTDC. The DG system is connected to the grid and is set to operate according to the droop characteristic with the reference active power obtained following the equation of $P_{ref} = P_0 - k_p(\omega_{abc} - \omega_{base})$, where ω_{abc} is the measured grid frequency, ω_{base} is grid nominal frequency, which is fixed at 376.99 rad/s and the frequency droop gain k_p is chosen at 40 pu for which nominal output power P_0 is set at 5 kW. The effect of filter resonance is first simulated by removing the resistive damping and replacing it with a small 0.5 Ω resistor. The PI parameters of the inner current control loop ($k_{p,i}$ and $T_{i,i}$) are selected as 0.5 pu and 0.0025 pu, respectively. Sampling frequency $f_{s,csi,pwm}$ 10 kHz is selected for the CSI of the PWM-based method, which results in the average switching frequency of 20 kHz and 10 kHz for the VSR and the CSI, respectively.

The dc-link voltage, the input current, the dc-link current, and the output current for the case without the damping resistor are illustrated in Fig. 5.5. It can be seen from the figure that without damping resistor, massive distortion (due to filter resonance) is shown in output current waveform. The input power injected to the converter amounts to 5 kW. The active output power is slightly smaller than the active input power, mostly due to the losses in input and output filter resistances and in switching devices. The reactive input power is maintained at 0 var to obtain the unity power factor. The reactive output power, on the other hand, is uncontrolled and is almost 1 kvar. The reactive output power can be controlled at 0 var by setting the power factor angle $\emptyset_0$ in (5.2) appropriately. However, it is not recommended since the increase in $\emptyset_0$ leads to a reduction in dc-link voltage according to (5.2), which can lead to more distortion in output current waveform.

To suppress the filter resonance, a damping resistor is required in the circuit, as previously discussed in this subsection. The transfer function of output current $\boldsymbol{i}_o$ with respect to inverter current $\boldsymbol{i}_{inv}$ and grid voltage $\boldsymbol{v}_g$ can be derived based on Fig. 5.4, as below.

$$\boldsymbol{i}_o = \frac{sL_o/R_d + 1}{s^2L_oC + s(R_oC + L_o/R_d) + 1}\,\boldsymbol{i}_{inv} - \frac{\frac{s^2L_oC}{R_d} + sC}{s^2L_oC + s\left(R_oC + \frac{L_o}{R_d}\right) + 1}\boldsymbol{v}_g, \tag{5.4}$$

Derived from (5.4), the damping ratio ζ for the second-order system can be calculated with (5.5)

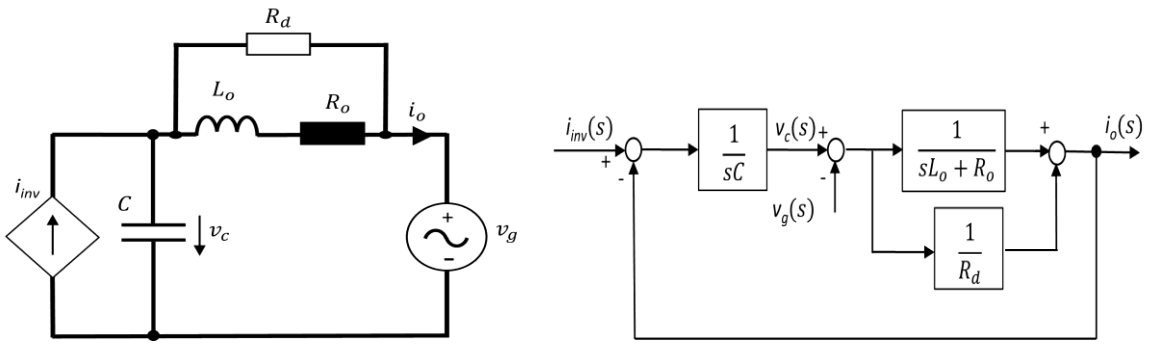

(a) (b)

Fig. 5.4 Model and block diagram for phase-a current in CSI side of the IBMC: (**a**) Model; (**b**) block diagram

$$\zeta = \frac{R_o C + L_o/R_d}{2\sqrt{L_o C}} \tag{5.5}$$

According to (5.5), large damping resistor R_d is needed to increase the ζ. the presence of R_d can increase the ζ**.** Hence, R_d equal to 20 Ω is added to achieve the desired damping. The dc-link voltage, the input current, the dc-link current, and the output current for this case are illustrated in Fig. 5.6. As can be seen in the figure, distortion in output current is significantly eliminated. However, the losses in the output filter resistances increase because of the damping resistor. The total losses are approximately 300 W, which amounts to around 6 % of the input power. We can conclude from this result that the using of passive damping is not an attractive solution for the filter resonance suppressing due to the losses inflicted by R_d. The THDs of input and output currents of the converter during steady-state are concluded in Table 5.1.

TABLE 5.1

CURRENT THDS FOR EXISTING PWM-BASED METHOD

Condition	Output current *THD*	Input current *THD*
The PWM-based method without a damping resistor	≈ 7 %	≈ 3 %
The PWM-based method with a damping resistor	≈ 3 %	≈ 2 %

Although a droop controller is applied, this method is still a grid-following control. Thus, it is not capable of operating when the converter is disconnected from the grid. To validate this, the test circuit is simulated for the case of sudden islanding from the grid at time T = 1 s. The output power and the output frequency illustrated in Fig. 5.7 clearly show that the controller has no mean to control the output frequency, as it keeps rising after grid islanding. The increase in frequency also leads to a

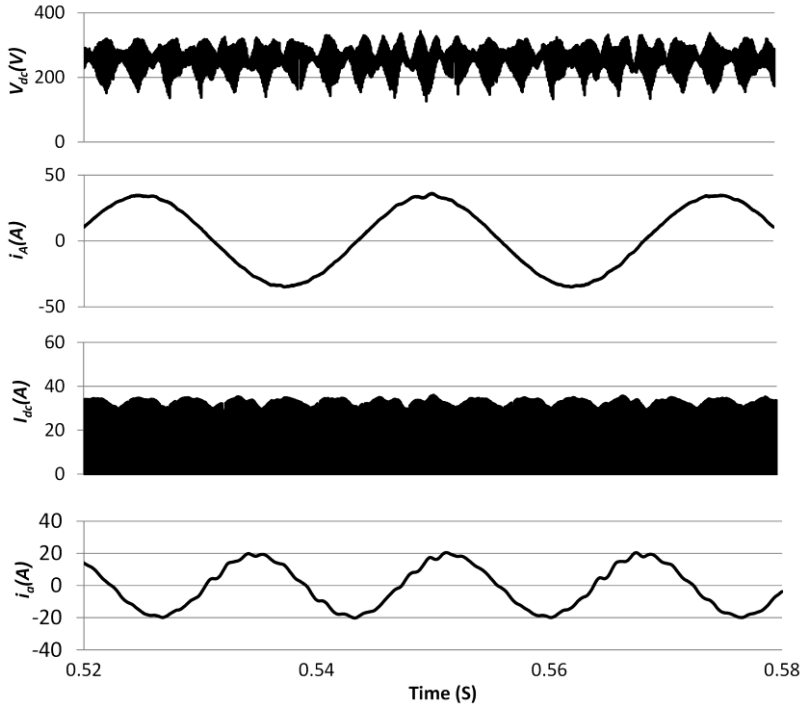

Fig. 5.5 The dc-link voltage, the phase-A input current, the dc-link current, and the phase-a output current of the PWM-based method without damping resistor, from top to bottom, respectively.

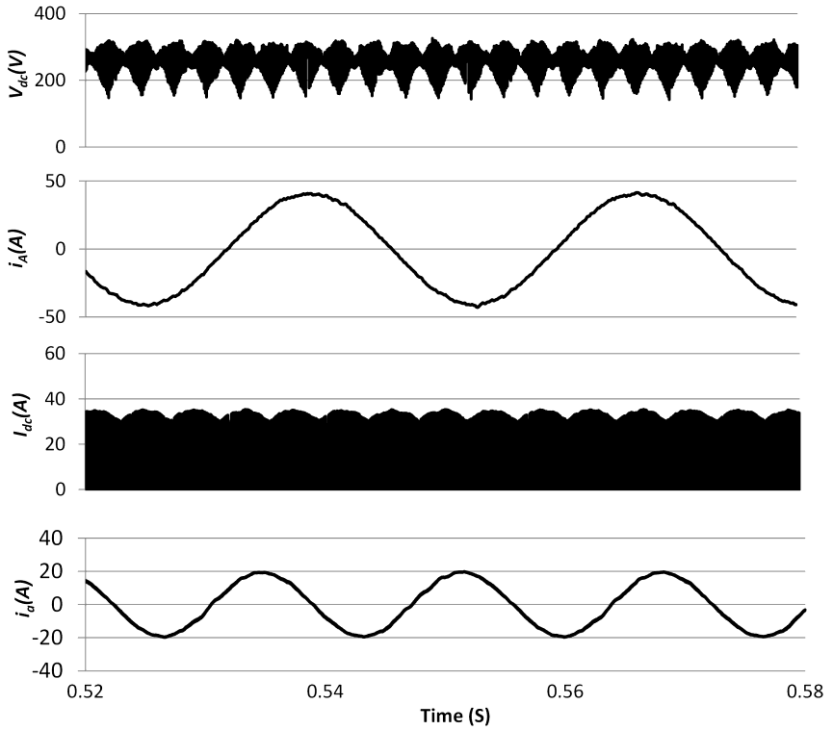

Fig. 5.6 The dc-link voltage, the phase-A input current, the dc-link current, and the phase-a output current of the PWM-based method with a damping resistor, from top to bottom, respectively.

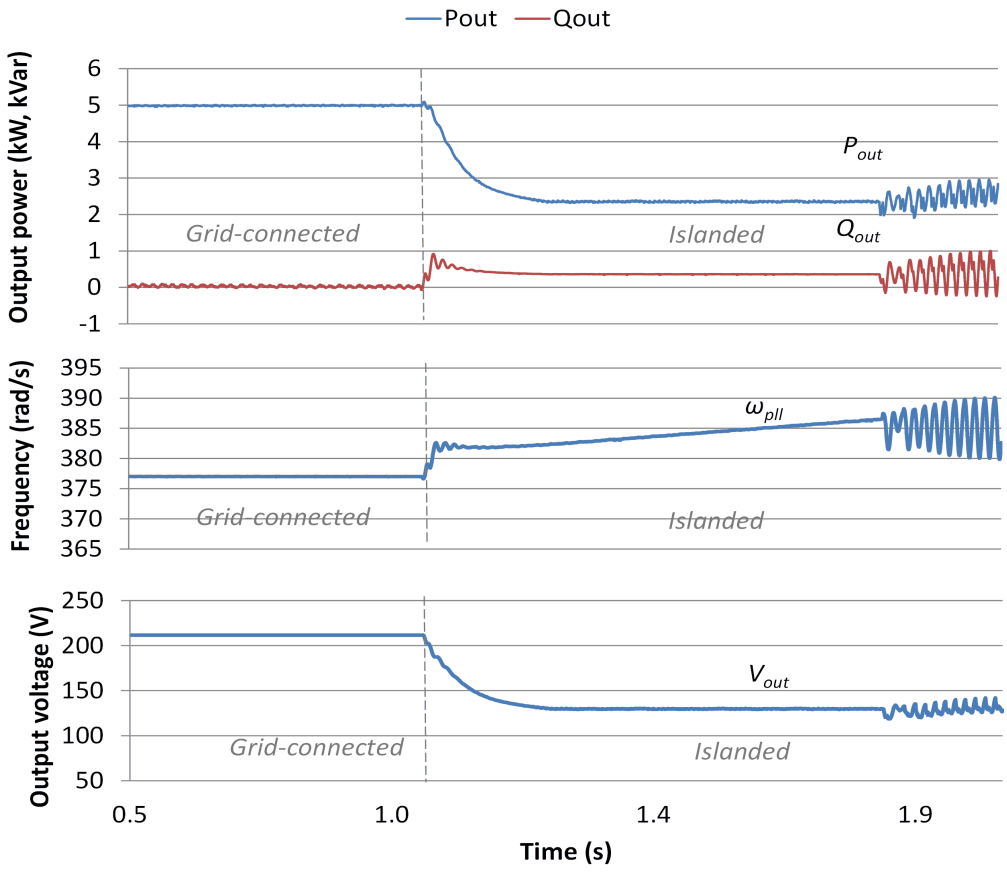

Fig. 5.7 The output active and reactive power, the output frequency and the output voltage amplitude of the existing PWM-based method with a damping resistor before and after grid-islanding, from top to bottom, respectively.

decrease in output power due to the characteristic of the *P-f* droop controller since the output power of the IBMC is determined purely by the power command of VSR and is not affected by the output network. The power command decreased until it reached zero, and the control system collapsed, as illustrated in Fig. 5.7. This figure also indicates that the controller cannot maintain the amplitude of the output voltage when the DG is islanded from the grid due to the nature of the modulation methods for the IBMC, which only utilizes the phase information in the control of the inverter side and has no control over the amplitude of the output voltage. All of these emphasize the unsuitability of such modulation methods for the implementation of the grid-forming-based VSG control, which needs to be able to control both voltage and frequency actively

5.4 The Proposed Control Scheme

5.4.1 Overall Control Scheme

The IBMC topology used for the proposed control scheme is adopted from the one explained in section 5.2. It consists of a VSR and a CSI, as shown in Fig. 5.1. However, the topology for the proposed scheme differs slightly from the one in Fig. 5.1, since the clamp diode is removed from fictitious

dc-link, as shown in Fig. 5.8. Because in the proposed control scheme, distortion in capacitor voltage caused by discharging current from the dc-link capacitor, as happened in the PWM-based method when a clamp diode is absent, can be avoided with direct control of capacitor voltage. Furthermore, the short circuit in parallel diodes of the VSR side under a negative dc-link voltage can be prevented by including an additional constraint in the cost function, as explained in subsection 5.4.2.

The overall control diagram of the proposed control is shown in Fig. 5.8. It is composed of the VSG control and the FCS-MPC parts. In order to achieve the grid-forming control, the VSG control part provides the output voltage and the output current commands for the CSI side of the IBMC. Furthermore, a power-command for the VSR side of IBMC in accordance with the power angle of the output network is also provided by the VSG control. This grants the DG with the ability to draw inertial power from the input source. In this work, the FCS-MPC is chosen for the implementation of VSG control instead of PWM-method based on two main reasons. First, the modulation index of CSI PWM is not adjustable because the zero current vector cannot be used in IBMC topology, as discussed in subsection 5.3.1. Without the zero current vector, PWM cannot control the amplitude of the output voltage according to the voltage command of VSG control. This implies that the ability of VSG control to regulate reactive power according to the *Q-V* droop cannot be recreated with the PWM-based method. Second, although the output amplitude of CSI can be indirectly controlled through the modulation of VSR PWM, proper tracking of voltage command cannot be ensured due to the complex coupling between the rectifier and the inverter controls, as discussed in section 5.3. The FCS-MPC, on the other hand, utilizes the system model and the real-time values of the system to determine the optimized converter's physical switching states directly, thus enabling proper tracking of voltage and current commands even without the use of zero current vectors of CSI.

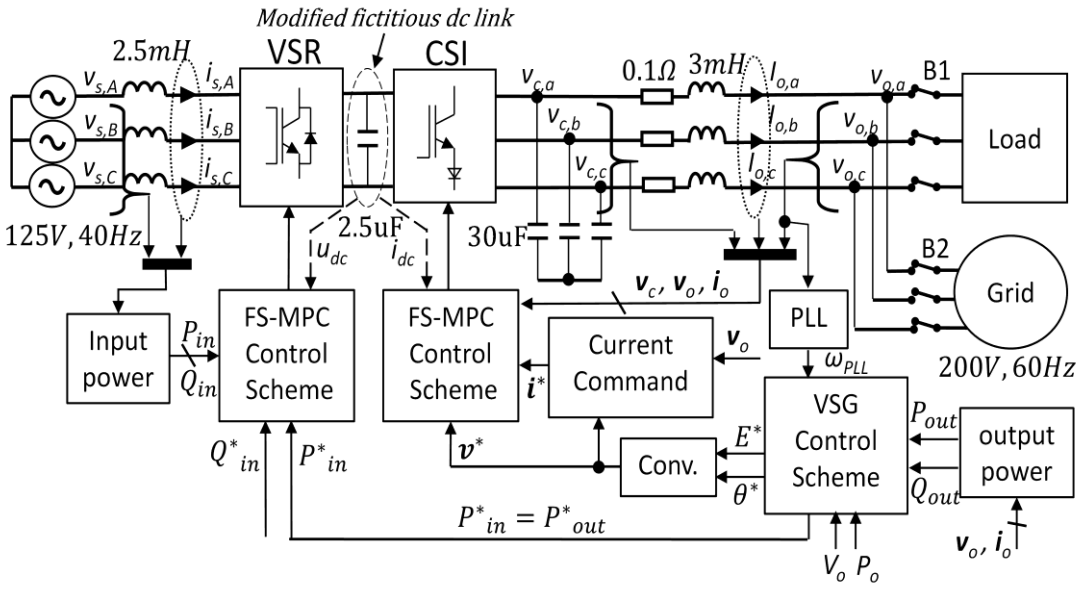

Fig. 5.8 The proposed control diagram of FCS-MPC for IBMC-based VSG

5.4.2 FCS-MPC Design

In this work, the FCS-MPC is chosen for the implementation of VSG control instead of PWM-methods based on two main reasons. First, the modulation index of CSI PWM is not adjustable because the zero current vectors cannot be used in IBMC topology, as discussed in subsection 5.3.1. Without zero current vectors, the PWM cannot control the amplitude of the output voltage according to the voltage command of VSG control. This implies that, with the PWM-based method, the ability of VSG control to regulate reactive power according to the *Q-V* droop cannot be recreated, and the amplitude of the output voltage cannot be maintained during islanded mode as discussed in subsection 5.3.2. Second, although the output amplitude of CSI can be indirectly controlled through the modulation of VSR PWM, proper tracking of voltage command cannot be ensured due to the complex coupling between the rectifier and the inverter controls, as discussed in section 5.3. The FCS-MPC, on the other hand, utilizes the system model and the real-time values of the system to determine the optimized converter's physical switching states directly. Thus it enables proper tracking of voltage and current commands even without the use of zero current vectors of CSI.

The FCS-MPC is also applied in the VSR side of the IBMC because of the faster dynamic response of the FCS-MPC compared to the PWM-based methods. This is crucial for the proposed VSG control, as the inertial power is provided from the power control of the VSR side.

1) IBMC SYSTEM MODEL

In order to use MPC to forecast the future values of the system variables, first, the mathematical model of the system is required. Therefore, the adopted models for both CSI and VSR sides will be explained in this section.

To realize a DG that can operate in both grid-connected and islanded modes, the inverter output voltage and inverter current controls should be the objectives of MPC for the CSI side. Thus, the model of a three-phase CSI with output *CL*-filter, as depicted in Fig. 5.1 is utilized to forecast the voltage and current outputs of the system. This model can be described in $\alpha\beta$-frame using capacitor dynamics equation (5.6) and inductance dynamics equation (5.7).

$$C\frac{d\boldsymbol{v}_c}{dt} = \boldsymbol{i}_{inv} - \boldsymbol{i}_o \tag{5.6}$$

$$L_o\frac{d\boldsymbol{i}_o}{dt} = \boldsymbol{v}_c - \boldsymbol{v}_o \tag{5.7}$$

where $\boldsymbol{v_c} = \left[v_{c,\alpha}\ v_{c,\beta}\right]^T$, $\boldsymbol{v}_o = \left[v_{o,\alpha}\ v_{o,\beta}\right]^T$, $\boldsymbol{i}_{inv} = \left[i_{inv,\alpha}\ i_{inv,\beta}\right]^T$ and $\boldsymbol{i}_o = \left[i_{o,\alpha}\ i_{o,\beta}\right]^T$ are capacitor voltage, output voltage, inverter current, and the output current. These equations can be rewritten as follows (5.8):

$$\frac{d\boldsymbol{x}}{dt} = \boldsymbol{A}\boldsymbol{x} + \boldsymbol{B}\boldsymbol{v}_o + \boldsymbol{B}_d\boldsymbol{i}_o \tag{5.8}$$

where $\boldsymbol{x} = \begin{bmatrix} i_{o,\alpha} \\ i_{o,\beta} \\ v_{c,\alpha} \\ v_{c,\beta} \end{bmatrix}, \boldsymbol{A} = \begin{bmatrix} 0 & 0 & \frac{1}{L_o} & 0 \\ 0 & 0 & 0 & \frac{1}{L_o} \\ \frac{1}{C} & 0 & 0 & 0 \\ 0 & \frac{1}{C} & 0 & 0 \end{bmatrix}, \boldsymbol{B} = \begin{bmatrix} -\frac{1}{L_o} & 0 \\ 0 & -\frac{1}{L_o} \\ 0 & 0 \\ 0 & 0 \end{bmatrix}$ and $\boldsymbol{B_d} = \begin{bmatrix} 0 & 0 \\ 0 & 0 \\ -\frac{1}{C} & 0 \\ 0 & -\frac{1}{C} \end{bmatrix}$.

A discrete-time model of the system derived from (5.8), using the general forward-difference Euler formula, for a sampling time T_s can be expressed in (5.9).

$$\boldsymbol{x}(k+1) = \boldsymbol{A}_q \boldsymbol{x}(k) + \boldsymbol{B}_q \boldsymbol{v}_o(k) \ + \boldsymbol{B}_{dq} \boldsymbol{i}_o(k) \tag{5.9}$$

where $\boldsymbol{A}_q = e^{\boldsymbol{A}T_s}, \boldsymbol{B}_q = \int_0^{T_s} e^{\boldsymbol{A}\tau} \boldsymbol{B} d\tau$ and $\boldsymbol{B}_{dq} = \int_0^{T_s} e^{\boldsymbol{A}\tau} \boldsymbol{B}_d d\tau$. From (5.8)–(5.9), it can be seen that the future values $\boldsymbol{v}_c(k+1)$ and $\boldsymbol{i}_o(k+1)$ can be determined according to inverter stage current $\boldsymbol{i}_{inv}(k)$. Obtaining the model of CSI is done according to the discussion in section 2.4.1. For each active current vectors (SC1-SC6) of CSI, the inverter stage current $\boldsymbol{i}_{inv}(k)$ is defined as follows:

$$\boldsymbol{i}_{inv}(k) = [S_{ap} - S_{an} \quad S_{bp} - S_{bn} \quad S_{cp} - S_{cn}]^T i_{DC} \tag{5.10}$$

where S_{ap}, S_{bp}, S_{cp} , S_{an}, S_{bn}, S_{cn} represent the switching states of the six switches in the rectifier stage, depicted in Fig. 5.1. The value of the switching state consists of 1 and 0, for which it represents the closed and open states, respectively. As shown in (5.10), although only active current vector (SC1-SC6) can be used in the CSI of IMBC, by predicting the inverter output variables corresponding to all the possible current vectors, the switching state that produces the desired amplitude and phase of the inverter output variables can be found. In contrast to the modulation method of the PWM-based control, which only follows the phase angle reference and only utilizes two nearest space vector to the reference phasor to generate output current, FCS-MPC certainly has more freedom to select an optimal switching state to fulfill the inverter control goal.

In order to accomplish the grid frequency supporting feature of VSG, the active input power must be controllable, as active power and grid frequency have an interdependent relationship. Additionally, the reactive power should be kept at zero to achieve unity power factor. Therefore, the control objectives of MPC for the VSR side are active and reactive power controls. The model of a three-phase voltage source rectifier with input *L*-filter depicted in the VSR side of IBMC in Fig. 5.1 is utilized for input active and reactive powers predictions. This model can be derived in αβ-frame with the inductance dynamics equation (5.11).

$$\boldsymbol{v}_s = \boldsymbol{v}_r + \boldsymbol{i}_s R_i + L_i \frac{\mathrm{d}\boldsymbol{i}_s}{\mathrm{d}t} \tag{5.11}$$

where $\boldsymbol{v}_s$ is the source voltage, $\boldsymbol{v}_r$ is the rectifier voltage, $\boldsymbol{i}_s$ is the source input current and R_i is the input filter resistor. The instantaneous rectifier input active and reactive powers from the source can be derived from (5.11), as described with the following equations.

$$P_{in} = \frac{3}{2} Re\{\boldsymbol{v}_s \boldsymbol{i}_s{}^*\} = \frac{3}{2}\left(v_{s\alpha} i_{s\alpha} + v_{s\beta} i_{s\beta}\right) \tag{5.12}$$

$$Q_{in} = \frac{3}{2} Im\{\boldsymbol{v}_s \boldsymbol{i}_s{}^*\} = \frac{3}{2}\left(v_{s\alpha} i_{s\beta} - v_{s\beta} i_{s\alpha}\right) \tag{5.13}$$

According to [43], the equations (5.12)-(5.13) can be rewritten in discretized forms as follows.

$$P_{in}(k+1) = T_s\left[-\frac{R_i}{L_i} P_{in}(k) - \omega_{in} Q_{in}(k) + \frac{3}{2L}\left(|\boldsymbol{v}_s{}^2| - Re\{\boldsymbol{v}_s \boldsymbol{v}_r{}^*\}\right)\right] + P_{in}(k) \tag{5.14}$$

$$Q_{in}(k+1) = T_s\left[\omega_{in} P_{in}(k) - \frac{R_i}{L_i} Q_{in}(k) - \frac{3}{2L} Im\{\boldsymbol{v}_s \boldsymbol{v}_r{}^*\}\right] + Q_{in}(k) \tag{5.15}$$

where $P_{in}(k+1)$ and $Q_{in}(k+1)$ are the forecast active and reactive powers, respectively and ω_{in} is the input source voltage frequency. Thus, the future value of input active and reactive powers of the DG for all voltage vectors can be predicted using the measured values of source voltage, source current and system parameters such as R_i L_i ω_{in}, and the set of possible rectifier voltages. As discussed in section 2.2.1 of Chapter 2, the rectifier voltage for each voltage vector (SV0-SV7) is defined according to the following expression:

$$\boldsymbol{v}_r(k) = [S_{Ap} - S_{An} \quad S_{Bp} - S_{Bn} \quad S_{Cp} - S_{Cn}]^T u_{DC} \tag{5.16}$$

where S_{Ap}, S_{Bp}, S_{Cp} , S_{An}, S_{Bn}, S_{Cn} represents the switching state of the six switches in the inverter stage, whose value is 1 or 0 for closed state and open state, respectively.

To prevent a short circuit in the antiparallel diodes of VSR, the dc-link voltage must always be positive. To ensure this, we must predict the value of dc-link voltage for each switching state using the capacitor voltages $\boldsymbol{v_c}$, which can be done according to the following equations.

$$u_{DC} = [S_{ap} - S_{an} \quad S_{bp} - S_{bn} \quad S_{cp} - S_{cn}] * \boldsymbol{v}_c \tag{5.17}$$

2) COST FUNCTION DEFINITION

Contrarily to classical control schemes, the presence of the cost function allows FCS-MPC to take into account a number of control goals, and to control different state variables simultaneously. Therefore, it is highly relevant to define the cost function appropriately. For the control of IBMC, variable quantities of both sides of the converter must be considered to make the whole system operate correctly.

In the CSI side, the control system is set to track the voltage and current references simultaneously. This can be achieved by defining the cost function (5.18).

$$g_{CSI} = k_v(\boldsymbol{v}_{c,\alpha\beta,pu}(\mathrm{k}+1) - \boldsymbol{v}^*{}_{\alpha\beta,pu})^2 + k_i(\boldsymbol{i}_{f,\alpha\beta,pu}(\mathrm{k}+1) - \boldsymbol{i}^*{}_{\alpha\beta,pu})^2 + g_m \tag{5.18}$$

where $\boldsymbol{v}^*{}_{\alpha\beta} = \left[v^*{}_\alpha \; v^*{}_\beta\right]^T$ is the reference vector of the capacitor voltage, $\boldsymbol{i}^*{}_{\alpha\beta} = \left[i^*{}_\alpha \; i^*{}_\beta\right]^T$ is the reference vector of the inductor current, $\boldsymbol{v}_{c,\alpha\beta}(k+1) = \left[v_{c,\alpha} \; v_{c,\beta}\right]^T$ is the predicted capacitor voltage and $\boldsymbol{i}_{f,\alpha\beta}(k+1) = \left[i_{f,\alpha} \; i_{f,\beta}\right]^T$ is the predicted inductance current and the subscript *pu* indicates the per-unit value. g_m is a constraint, which is included in the cost

function to ensure that dc-link voltage never becomes negative. It can be defined with the following equation (5.19).

$$g_m = \begin{cases} 10^8, & u_{DC}(k+1) < 0 \\ 0, & u_{DC}(k+1) \geq 0 \end{cases} \tag{5.19}$$

In the VSR side, the control objectives are to control input active and reactive power according to the input commands. This can be achieved by defining the cost function as follows.

$$g_{VSR} = (P_{in}(k+1) - P^*{}_{in})^2 + (Q_{in}(k+1) - Q^*{}_{in})^2 \tag{5.20}$$

where $P^*{}_{in}$ and $Q^*{}_{in}$ are the input active and reactive power commands, respectively.

Although FCS-MPC is capable of controlling different variables at the same time through the modification of the cost function, the tuning of the weighting parameters is a highly complex task when a number of terms exist in the cost function. This issue is considered one of the most critical open topics for the FCS-MPC. In the literature, different approaches have been thoroughly analyzed, and several solutions have been proposed [44]–[47].

In this control system, the weighting parameters exist in cost functions (5.18) and (5.20). However, the controls of active and reactive power in (5.20) are equally important, and the weighting parameters can be omitted from the cost function. In the case of the CSI, to properly tune the weights in (5.18), the system has been initially simulated in a steady-state condition ($P^*{}_{in} = 5\ kW, Q^*{}_{in} = 0\ Var$) using PSCAD/EMTDC. The ratio between the weighting parameter k_v and k_i has been arbitrarily set equal to 1:1. Subsequently, the total harmonic distortion (THD) of the output currents during steady-state in grid-connected operation and the ability of the controller to synchronize with the grid has been analyzed for different weighting parameter ratios, as concluded in Table 5.2. Conclusively, a higher ratio of k_i compared to k_v helps to reduce the current THD. However, as k_i keeps increasing, the controller's ability to track voltage command worsens, which leads to a failure in grid synchronization. Hence $k_v : k_i$ equal to 1:3 has been selected for the proposed controller.

3) FILTER RESONANCE DAMPING

To ensure proper operation, the IBMC requires an inductive input filter on the VSR and a capacitive output filter on the CSI. However, in order to improve the quality of the waveforms, *CL*-filter is usually preferred. Nevertheless, the presence of resonance frequency has to be taken into account, since FCS-MPC possesses a spread harmonic spectrum. It might contain harmonics components at the resonant frequency of *CL*-filter at a certain point of operating. However, this will result in resonance, if only the output inverter current $\boldsymbol{i}_o(s)$ alone is directly controlled, whereas the capacitor age $\boldsymbol{v}_c(s)$, is indirectly controlled by the current and thus highly dependent on filter impedances.

My proposed FCS-MPC utilizes a multivariable system to control both $\boldsymbol{v}_c(s)$ and $\boldsymbol{i}_o(s)$ simultaneously. This is different from conventional cascade control of voltage and current, where settling time of the inner loop has to be significantly faster than the settling time of the outer loop. Therefore, at the resonant frequency where $\boldsymbol{v}_c(s)$ and $\boldsymbol{i}_o(s)$ are oscillating with the same dynamics, the control of the outer loop is not fast enough to provide damping effect. Contrarily, the multivariable con-

trol of FCS-MPC is conducted at the same bandwidth. This ensures that the regulation of $\boldsymbol{v}_c(s)$ can damp the distortion caused by the harmonics of $\boldsymbol{i}_o(s)$ and the control of $\boldsymbol{i}_o(s)$ is able to reduce the disturbance caused by the harmonics of $\boldsymbol{v}_c(s)$. Hence, by controlling both *CL*-filter voltage and current at the same instances, the frequency response of the filter is no longer influenced by its impedance alone. Thus the uncontrolled resonant energy oscillation between the inductances and the capacitance is effectively avoided. This concept has been successfully applied in FCS-MPC-based grid-connected VSI in [36], whereas similar concepts were also proposed in [37]–[39] for the grid-connected FCS-MPC-based AC/DC converter

5.4.3 The Proposed Virtual Synchronous Generation Control for IBMC

The objective of VSG is to track the dispatch power command while providing virtual inertia to the DG to slow down any deviation of the grid frequency. This can be realized for IBMC-interfaced-DG using the proposed VSG control, as shown in Figure 5.9. Some of the blocks contained in the proposed VSG control are modified from [27]. It consists of the "Swing Equation Function", the "Governor", and the "Q droop" parts. P_o, P_{out}, P_{gov}, Q_o, Q_{out}, V_{out}, ω_m, ω_{PLL}, E^* and θ^* represent the output active power command, the output active power, the shaft power from governor, the output reactive power command, the output reactive power, the output voltage amplitude, the mechanical frequency of rotors, the output frequency measured by PLL, the voltage reference magnitude and the power angle reference, respectively. Virtual inertia is emulated in the block "Swing Equation Function" with the help of the well-known swing equation (5.21).

$$P_{gov} - P_{out} + D(\omega_{base} - \omega_{PLL}) = J\omega_m \frac{\mathrm{d}\omega_m}{\mathrm{d}t} \tag{5.21}$$

where J is the moment of inertia, D is the damping factor produced by the damper windings, P_{out} is the output active power, and ω_{base} is nominal grid frequency. The function of the shaft power P_{gov} regulated by a governor is shown in (5.22).

$$P_{gov} = P_0 - k_p(\omega_m - \omega_{base}) \tag{5.22}$$

TABLE 5.2
FCS-MPC WEIGHT PARAMETER TUNING

k_v: k_i ratio	Current *THD*	Synchronization
1:1	10 %	OK
1:2	5 %	OK
1:3	2.5 %	OK
1:4	-	Failed

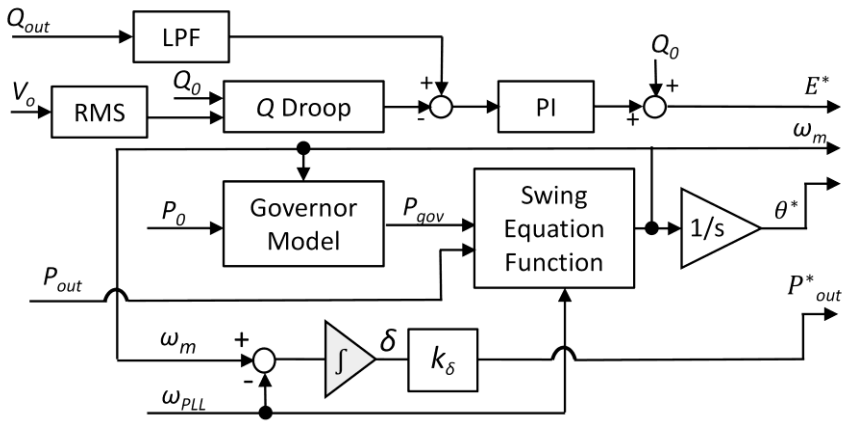

Fig. 5.9 The control diagram of the VSG control scheme for IBMC

where k_p is the droop coefficient. The block "Q droop", as well as the design details of all blocks in Fig. 5.9, and the tuning of VSG parameters, are all explained in [27] and hence will be omitted in this work.

In the previous research works of VSG applications for the VSIs [26], [27], [36], the output active power of the converter was drawn directly from the energy storage element in correspondence to the phase angle difference between the inverter output voltage and the grid voltage. Hence, the output power of such VSG control can be regulated by merely controlling the output voltage. However, due to the lack of energy storage elements in the present work, the output power of the IBMC must be controlled by the input power command of the VSR side, as the output power will follow the controlled power flows from the VSR to the fictitious dc-link before reaching the output network. Thus, the output power of the IBMC can no longer be controlled with the output voltage control alone.

If we consider the swing equation (5.21), it can be concluded that the inertial response is created by the power exchange between the power of the mechanical rotor (P_{gov}), which is controlled by the governor, and the power injected to the grid (P_{out}), which is influenced by the output network variables such as frequency and phase angle. Hence, in order to create a proper inertial response, the input power command needs to be regulated to mimic how the output power of SGs exchanges power with the electrical grid according to the power angle. Contrarily, if the powers command of VSR is delivered by methods such as average dc-link voltage control, P_{out} will be independent of the change in the frequency of the output network. Thus the power exchange between the mechanical rotor and the electrical grid of SGs will not be recreated. The power command of VSG control can thus be determined with the help of the equation of the active power flow in a two-bus bar system [48] shown in (5.23).

$$P_{out} = \frac{V_o V_c}{X_o} sin\,\delta \tag{5.23}$$

where V_o is the output voltage amplitude, V_C is the output filter's capacitor voltage amplitude, X_o

is the output filter reactance, and δ is the phase angle difference between DG and grid. Assuming V_o, V_c and X to be constant and $sin\,\delta \approx \delta$ for a small phase angle, P_{out} is equal to $K\delta$ when $K = V_c V_o / X_o$. However, since the value K of the proposed control is not limited by the physical values of the system like real SGs and can be arbitrarily selected to optimize the system performance, P_{out} of the proposed VSG control can be rewritten as.

$$P_{out} = k_\delta \delta \tag{5.24}$$

where k_δ is the optimized synchronizing constant, and δ can be determined with the following equation (5.25).

$$\delta = \int (\omega_m - \omega_{PLL})\, dt \tag{5.25}$$

With (5.24)–(5.25), the active power command for VSR is obtained as depicted in Fig. 5.9. As for the reactive power command of VSR, it is set to zero for unity power factor operation.

In the CSI side, the voltage command for FCS-MPC is obtained with the VSG control scheme in Fig. 5.9. However, to achieve resonance damping, both voltage and current control must be embedded into a single loop control, as depicted in Fig. 5.8. Therefore, the current command must be provided for FCS-MPC. The current command can be determined by considering the relationship between the inverter output voltage, the output current, and the capacitor phase voltage shown in Fig. 5.1. It can be described in a stationary frame or $\alpha\beta$-frame with Eq. (5.26).

$$\boldsymbol{v}_{c,\alpha\beta} = \boldsymbol{v}_{o,\alpha\beta} + \boldsymbol{i}_{o,\alpha\beta}(R_o + j(X_o)) \tag{5.26}$$

where $\boldsymbol{v}_{c,\alpha\beta}$ is the capacitor voltages, $\boldsymbol{i}_{o,\alpha\beta}$ the output current and $\boldsymbol{v}_{o,\alpha\beta}$ is the output voltages. $X_o$denotes the filter reactance and R_o denotes filter resistance. If we consider that the $\boldsymbol{v}_{c,\alpha\beta}$ in (5.26) equals to the voltage command described by $E^*$and θ^* from the VSG control, the currents references i_α^* and i_β^* can be expressed in the stationary frame as illustrated in (5.27), and they will be used as the current command for the CSI side of FCS-MPC.

$$\begin{bmatrix} i_\alpha^* \\ i_\beta^* \end{bmatrix} = \boldsymbol{Y}\left\{ \begin{bmatrix} E^* cos\theta^* \\ E^* sin\theta^* \end{bmatrix} - \begin{bmatrix} v_{o,\alpha} \\ v_{o,\beta} \end{bmatrix} \right\} \tag{5.27}$$

where $\boldsymbol{Y} = \frac{1}{{R_o}^2 + {X_o}^2} \begin{bmatrix} R_o & X_o \\ -X_o & R_o \end{bmatrix}$.

1) STABILITY AND TRANSIENT PERFORMANCE ANALYSES

The modification of the VSG control explained in section 5.4, suggests the use of ω_{PLL} to determine the output power command. However, the dynamic response of the phase-locked loop (PLL), which is given by (5.28), is lower than the real $\omega_g$and this might affect the performance of the modified VSG control. In order to study the influence of the PLL toward the stability and transient performance of the VSG control, a state-space model for the proposed VSG control (with PLL) is obtained as given in (5.29)–(5.35). The model and the transient response of the PLL is well discussed in

[49]. The transient response can be described with the following expression.

$$G_{pll}(s) = \frac{\omega_{PLL}(s)}{\omega_g(s)} = \frac{k_{p,pll}s + k_{i,pll}}{s^2 + k_{p,pll}s + k_{i,pll}} \tag{5.28}$$

Since the dynamic response of the FCS-MPC is fast, the output power is assumed to be equal to the power command. Then the state-space model can be expressed as follows.

$$\begin{cases} \dot{\boldsymbol{x}} = \boldsymbol{A}\boldsymbol{x} + \boldsymbol{B}u + \boldsymbol{E}w \\ \boldsymbol{y} = \boldsymbol{C}\boldsymbol{x} \end{cases} \tag{5.29}$$

where $\boldsymbol{x}$, u, w and $\boldsymbol{y}$ are states, input, disturbance and outputs vectors, respectively, and

$$\boldsymbol{y} = [\Delta\omega_m \quad \Delta P_{out} \quad \Delta\omega_{PLL}]^T \tag{5.30}$$

$$\begin{gathered} \boldsymbol{x} = \left[\Delta\omega_m \quad \Delta P_{out} \quad \int \Delta\,\delta_{err,pll} \quad \Delta\,\delta_{err,pll}\right]^T \\ u = \Delta P_0 \\ w = \Delta\omega_g \end{gathered} \tag{5.31}$$

$$\boldsymbol{A} = \begin{bmatrix} \frac{-(k_p + D)}{J\omega_o} & \frac{-1}{J\omega_o} & \frac{Dk_{i,pll}}{J\omega_o} & \frac{Dk_{p,pll}}{J\omega_o} \\ k_\delta & 0 & -k_\delta k_{i,pll} & -k_\delta k_{p,pll} \\ 0 & 0 & 0 & 1 \\ 0 & 0 & -k_{i,pll} & -k_{p,pll} \end{bmatrix} \tag{5.32}$$

$$\boldsymbol{B} = \left[\frac{1}{J\omega_o} \quad 0 \quad 0 \quad 0\right]^T \tag{5.33}$$

$$\boldsymbol{E} = [0 \quad 0 \quad 0 \quad 1]^T \tag{5.34}$$

$$\boldsymbol{C} = \begin{bmatrix} 1 & 0 & 0 & 0 \\ 0 & 1 & 0 & 0 \\ 0 & 0 & k_{i,pll} & k_{p,pll} \end{bmatrix} \tag{5.35}$$

where $\delta_{err,pll} = \int(\omega_g - \omega_{PLL})dt$.

It is clear that the poles of $Y(s)/W(s)$ transfer function are available in the eigenvalues of $\boldsymbol{A}$. The loci of eigenvalues of $\boldsymbol{A}$ with a variation of $k_{i,pll}$ is shown in Fig. 5.10 when $k_{p,pll}$ is selected according to [49]. First, it can be seen in Fig. 5.10 that all the poles of the system located on the left half of the *s*-plane, which implies that the system is stable. It is also shown in Fig. 5.10 that if the PLL has a rather quick dynamic response (if $k_{i,pll}$ is large enough), the effect of the third pole that locates near the dominant poles will be lessened as it is located farther to the left of the two dominant poles. In this case, the response of the system will be mostly defined by the two dominant poles, as can be described with the following expressions [50]:

$$\omega_n = \sqrt{\frac{k_\delta}{J\omega_0}} \tag{5.36}$$

$$\zeta = \frac{k_p + D}{2\sqrt{k_\delta J\omega_0}} \tag{5.37}$$

where ω_n is the undamped natural frequency, and ζ is the damping ratio. However, as shown in Fig. 5.10, even with a properly designed PLL with a fast dynamic response, the locations of the two additional poles are not far enough to the left of dominant poles, their effect cannot be totally neglected. Hence, the response of P_{out} will be slower than the previous VSG controls, thus finally results in a less inertial response. This can be interpreted as a delay effect of the PLL, because unlike the VSG system with an energy storage element, P_{out} of the proposed control is not dispatched directly from the energy storage element. It is instead regulated by the power command, which depends on the ω_{PLL}. This is crucial for VSG control, as P_{out} needs to react quickly to the power imbalance in order

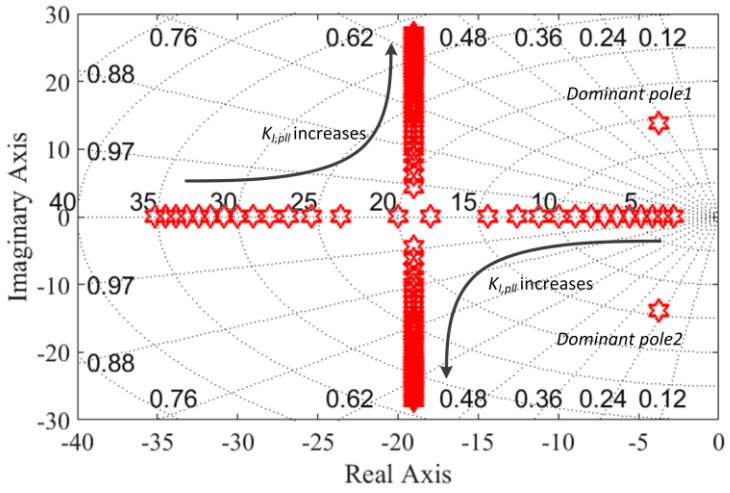

Fig. 5.10 Eigenvalue loci with changing of $k_{i,pll}$

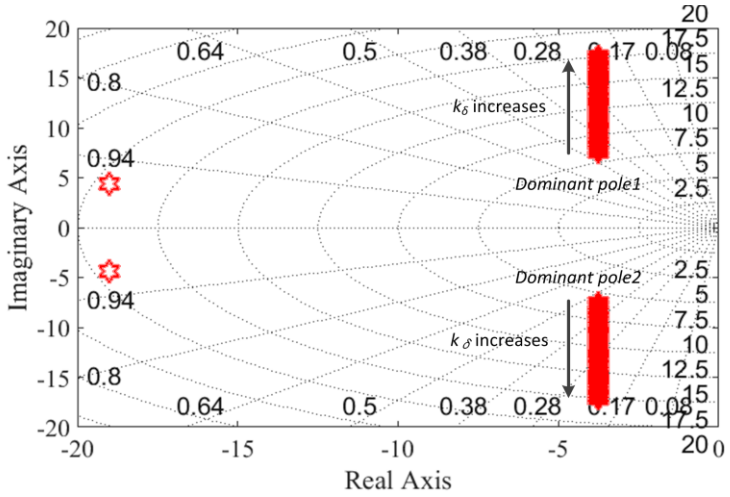

Fig. 5.11 Eigenvalue loci with changing of k_δ

to create a proper inertial response. Since k_δ of the proposed VSG control is not limited by the physical values of the system and can be arbitrarily selected, we can find an optimal value of k_δ by studying the effect of adjusting k_δ with the loci of eigenvalues of $\boldsymbol{A}$, as shown in Fig. 5.11. It indicates that increasing k_δ leads to an increase in ω_n. This can compensate for the delay effect of the PLL. Hence, $k_\delta = 2.5{*}V_c V_o / X_o$ is chosen for the proposed control.

5.5 Simulation and Discussion

In order to evaluate the performance of the proposed control scheme, simulation-based comparative studies between the proposed scheme and the investigated existing method are performed in the PSCAD/EMTDC environment. Line impedance of 0.03 mH and 0.5 Ω is added to the simulation circuit in order to create a mismatch between the parameters used for model prediction and real values of line and filter impedance. This will verify whether the proposed MPC scheme can operate with an inaccurate model. The simulation parameters are given in Table 5.3, where M is the inertia constant and is equal to$(J\omega_{base}{}^2)/S_{base}$. In order to generate comparable average switching frequency to PWM-based method, the sampling frequency for the VSR $(f_{s,vsr,mpc})$ is selected at 40 kHz and the sampling frequency for the CSI $f_{s,csi,mpc}$ of FCS-MPC-based control is selected at 20 kHz, respectively.

TABLE 5.3
SIMULATION PARAMETERS

Parameter	Value	Parameter	Value
S_{base}	5 kVA	J	0.28 $kg \cdot m^2$
k_p	40 pu	D	200 pu
V_{based}	200 V	k_δ	70000
$\omega_{base} = \omega_{grid}$	376.99 rad/s		
$f_{s,csi}$	20 kHz	$f_{s,vsr}$	40 kHz

5.5.1 Normal Operation

The performance of the proposed VSG control for the IBMC is verified with simulations of the test circuit displayed in Fig. 5.8. Initially, the DG system is connected to the grid with the reference active power of DG (P_0) equals 4 kW and reference reactive power of DG (Q_0) equals 1 kvar. The power commands are changed to 5 kW and 0 kvar at T = 3 s. The DG system is then set to operate in islanded mode at T = 5 s. The load initially connected to the system is 3 kW + 1 kvar, and it is increased to 5.5 kW + 0.05 kvar at T = 7 s. The phase-A input current and the phase-a output current during the grid-connected operation of the proposed method in the event of power command changing at T = 3 s is illustrated in Fig. 5.12. The figure shows that the input and output current waveforms are smoothly changed when the power command is changed. The zoom-ups of the dc-link

voltage, the input current, the dc-link current, and the output current for the grid-connected operation are depicted in Fig. 5.13. This figure shows that both input and output current waveforms are sinusoidal, and neither voltage nor current spikes are observed on the dc capacitor. Therefore the converter is operating properly.

The proposed VSG-based control is inherently capable of islanded operation like a traditional SG. To illustrate this feature, the phase-A input current, the phase-a output voltage, and the phase-a output current are displayed in Fig. 5.14. This figure clearly shows that the controller is capable of riding through the grid islanding while producing sinusoidal waveforms of voltage and current in both modes of operation. The output active and reactive powers, the output frequency, and the output voltage amplitude for the whole simulation are illustrated in Fig. 5.15. It can be seen that the system quickly and seamlessly commutates from the grid-connected mode into the islanded mode, supplying the required 3 kW + 1 kvar of power to the local load. The system is also able to react to change in load during islanded operation, as evidenced in Figs. 5.15 and 5.16, where waveforms of the phase-A input current, the phase-a output voltage, and the phase-a output current are depicted. The output frequency and the output active power of the control system in Fig. 5.15, are illustrating how the system is settling to operate at a different frequency according to the droop characteristic, whereas the output voltage amplitude of the system is maintained around the nominal ue (V_{based}) throughout the operation. Furthermore, the change in output frequency during the load transition in islanded mode demonstrates the inertial response of the controller, as the output frequency slowly decreases from around 378.5 rad/s to around 376 rad/s. The reduction of frequency occurs for around 1 s until the new frequency set point is reached. This is a typical VSGs performance, as analyzed in [26], [27]. The zoom-ups of the dc-link voltage, the input current, the dc-link current, the phase-a output voltage, and the output current for islanded operation illustrated in Fig.

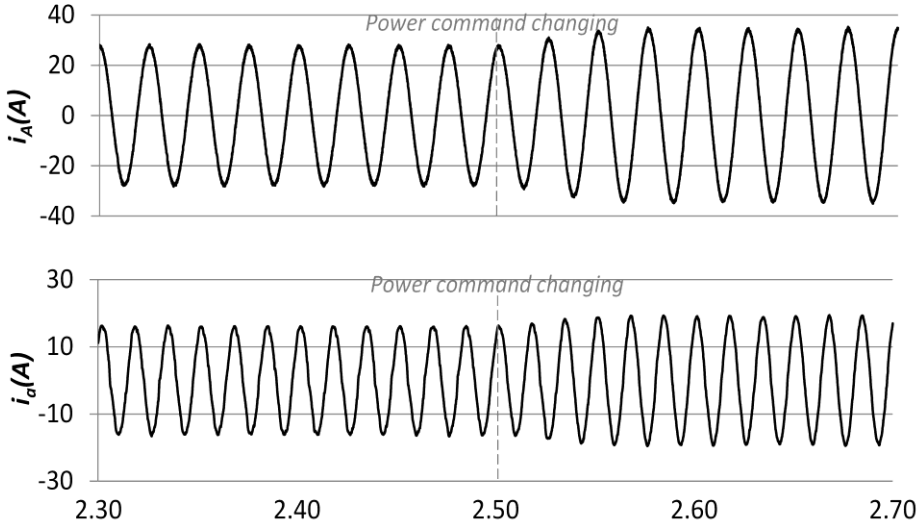

Fig. 5.12 The phase-A input current, and the phase-a output current of the proposed method during power command changing in the grid-connected mode

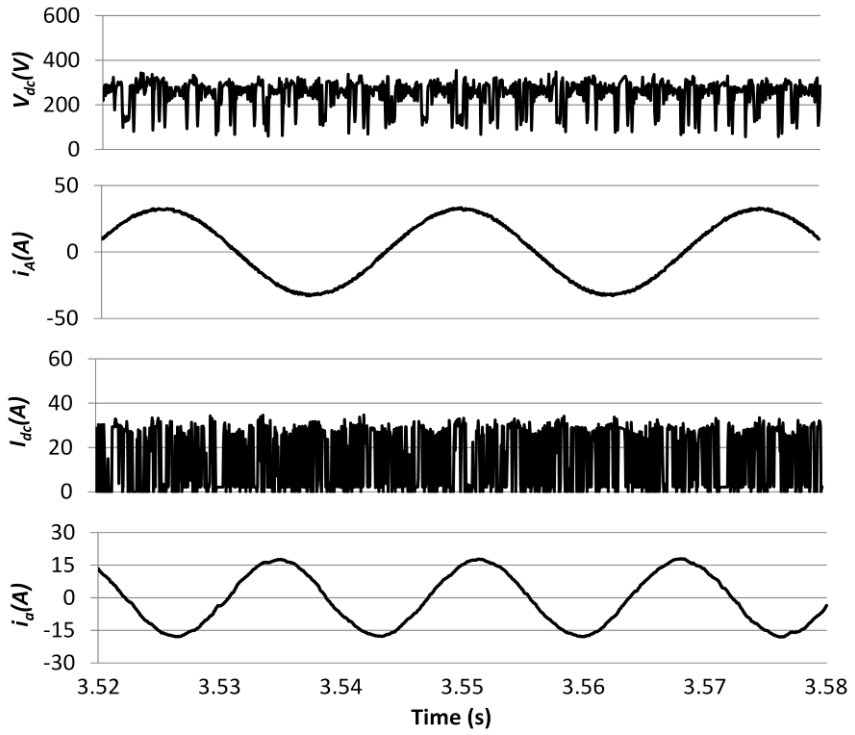

Fig. 5.13 The dc-link voltage, the phase-A input current, the dc-link current, and the phase-a output cur-rent of the proposed method during the grid-connected mode, from top to bottom, respectively.

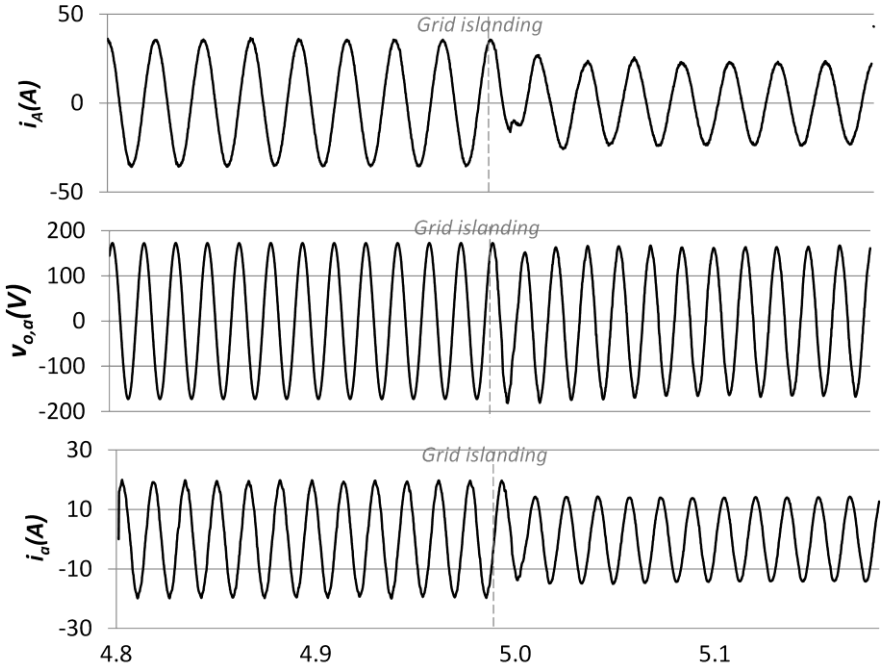

Fig. 5.14 The phase-A input current, the phase-a output voltage, and the phase-a output current of the proposed method during grid islanding

5.17, indicates that current and voltage are almost sinusoidal even without a passive damping resistor

Lastly, the THD of input and output currents of the proposed control during steady-state are concluded in Table 5.4. Compared to Table 5.1, it is clearly shown that the proposed control can achieve comparable and even superior resonance damping ability compared to the exiting method with a damping resistor.

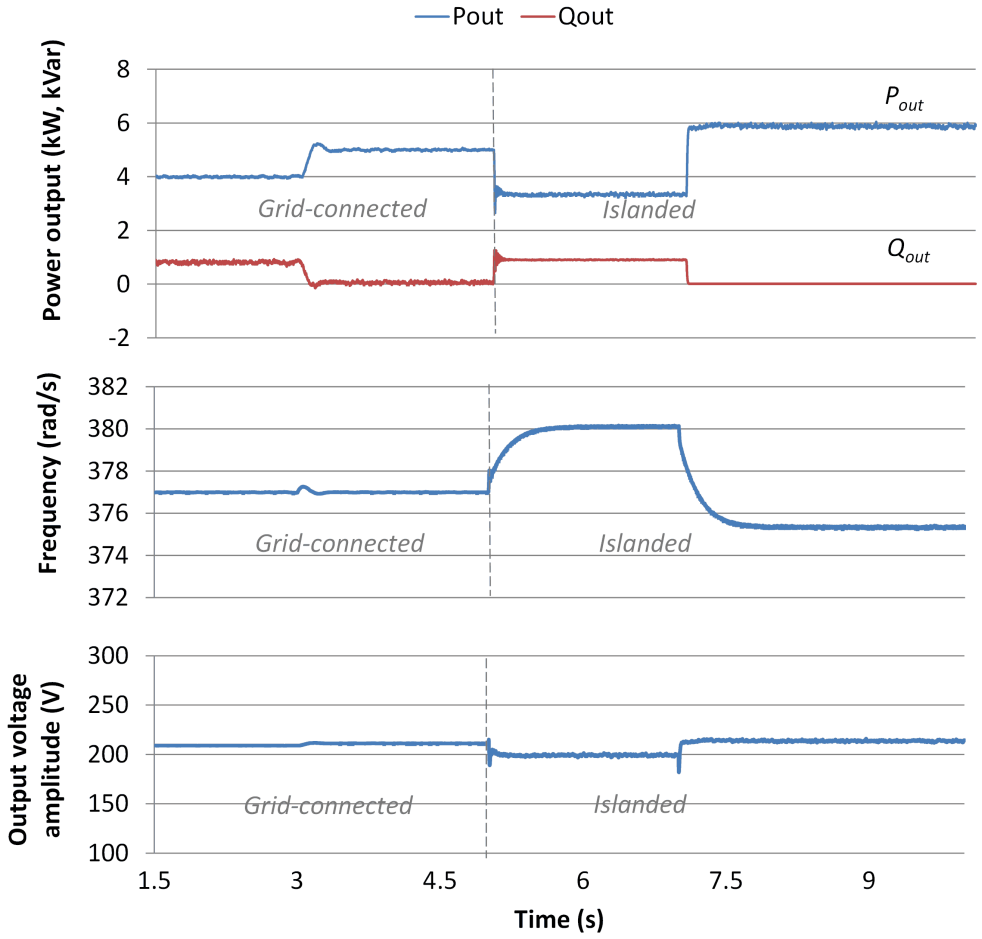

Fig. 5.15 The output active and reactive power, the output frequency, and the output voltage amplitude of the proposed control scheme, from top to bottom, respectively.

TABLE 5.4

CURRENT THDS FOR THE PROPOSED SCHEME

Condition	Output current *THD*	Input current *THD*
The proposed method during grid-connected mode	≈ 3 %	≈ 1.5 %
The proposed method during islanded mode	≈ 2 %	≈ 1 %

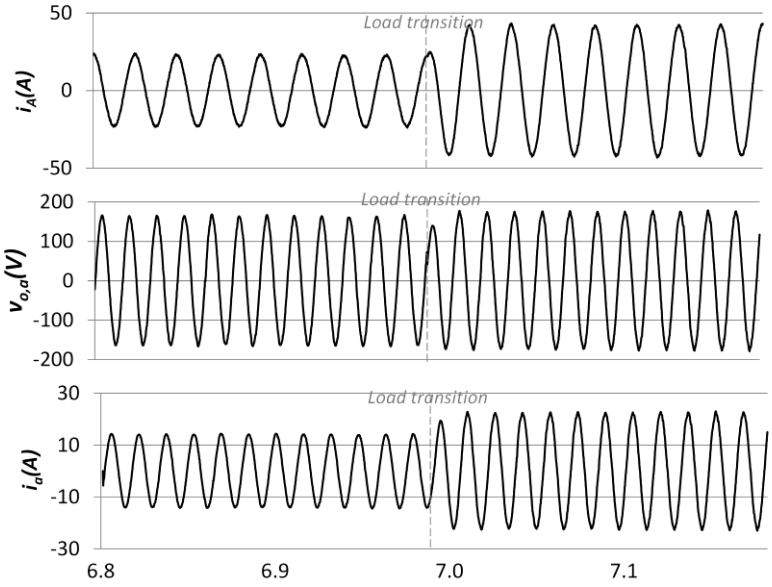

Fig. 5.16 The phase-A input current, the phase-a output voltage, and the phase-a output current of the proposed method during load transition in islanded mode

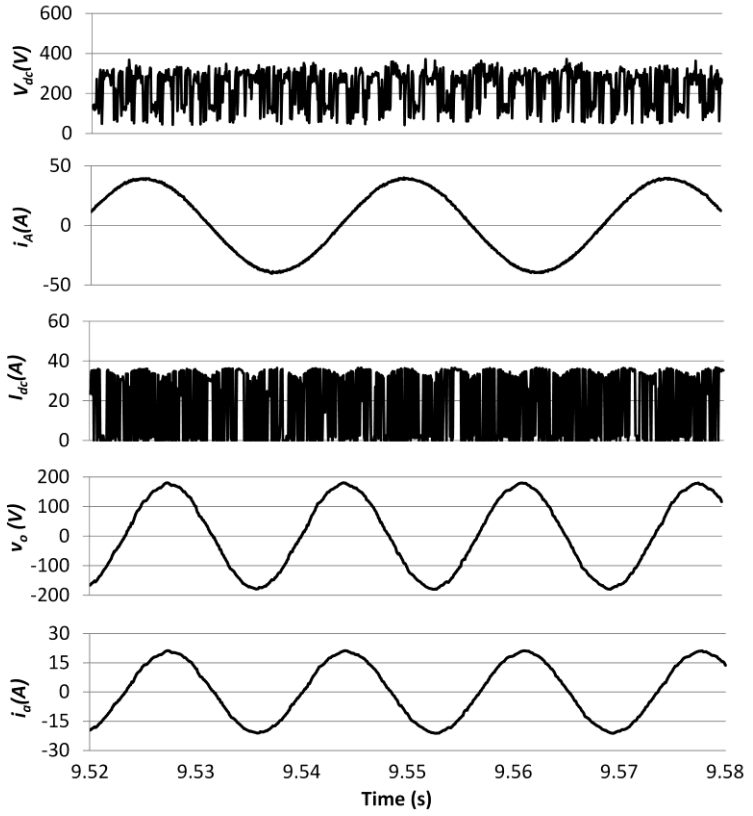

Fig. 5.17 The dc-link voltage, the phase-A input current, the dc-link current, the phase-a output voltage, and the phase-a output current of the proposed method during the islanded mode, from top to bottom, respectively

5.5.2 Operation in the Presence of Model Uncertainty

In practice, the real values of the inductance and capacitance could deviate from the supposed ones, especially on the grid side due to the presence of the line impedance. Here, to explore the robustness of the proposed control, the performance of the proposed control scheme is examined when the model used for prediction is not accurate. The simulations of the test circuit shown in Fig. 5.8 are conducted again with mismatches between the parameters used for prediction and real system parameters. In the first case, the values of output filter inductance and capacitance are changed from 3 mH and 30 μF to 2.5 mH and 25 μF, respectively. Then in the second case, the inductance and capacitance are changed to 5 mH and 40 μF, respectively. The parameters used for prediction and other parameters are the same as the previous case. The output active and reactive powers, the output frequency, and the output voltage amplitude of Case 1 and Case 2 are illustrated in Fig. 5.18. and 5.19, respectively. For both cases, the predictive controller is able to achieve proper control similar to the case when the model of the system is accurate. Hence, we can conclude that the proposed FCS-MPC is not sensitive to uncertainty in prediction parameters

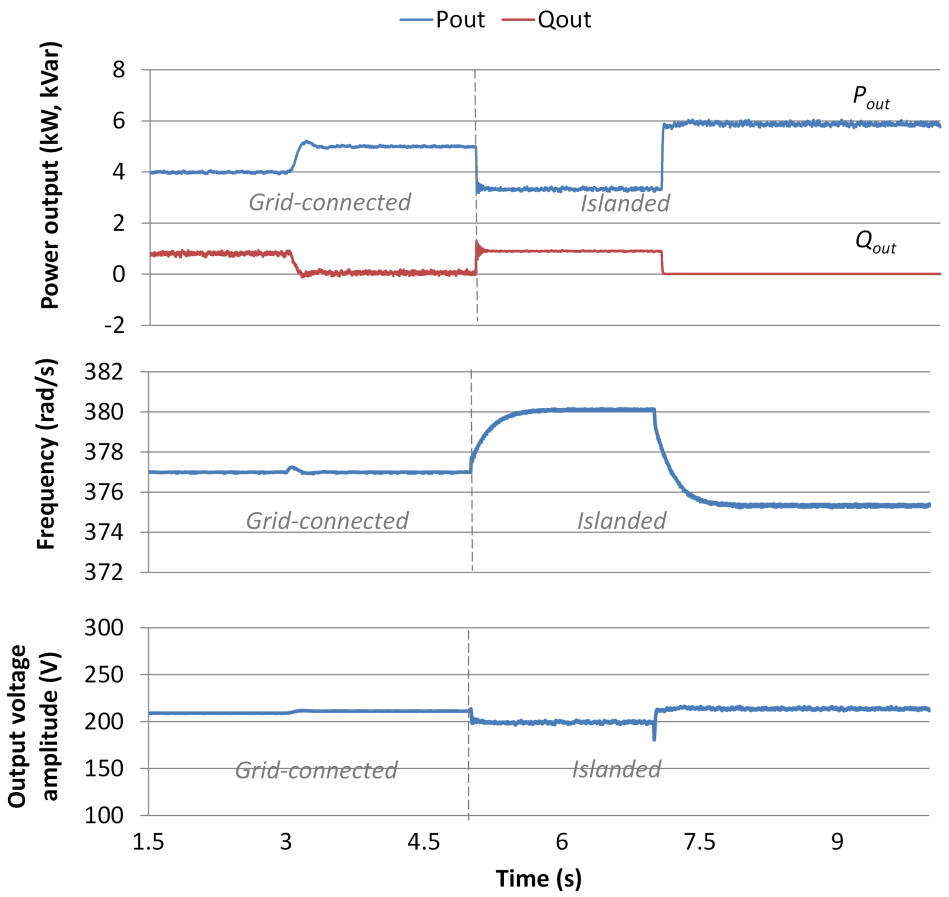

Fig. 5.18 The output active and reactive power, the output frequency, and the output voltage amplitude of the proposed control scheme with uncertainty in the prediction model (Case1).

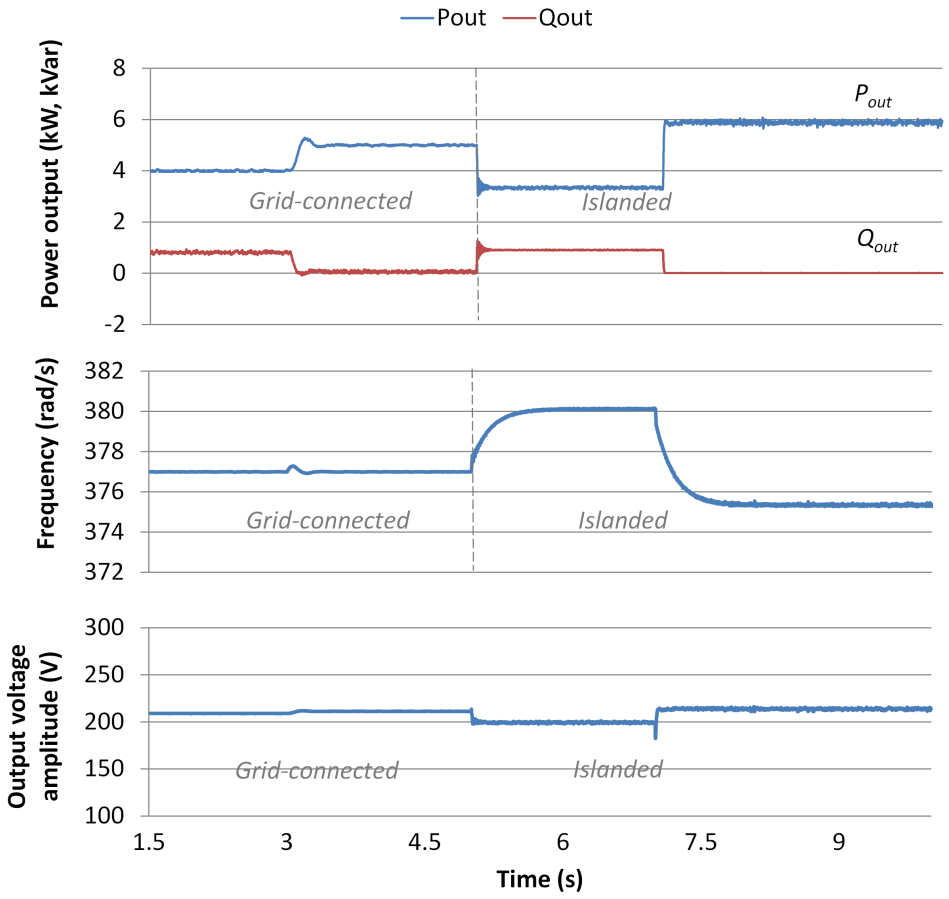

Fig. 5.19 The output active and reactive power, the output frequency, and the output voltage amplitude of the proposed control scheme with uncertainty in the prediction model (Case2).

5.5.3 Inertial Response

To demonstrate the inertial response of the VSG when the load is increased from 3 kW + 1 kvar to 5.5 kW + 0.05 kvar during the islanded operation, The simulations of the test circuit displayed in Fig. 5.8 are conducted again with the same simulation parameters. However, different values of parameter J are simulated in order to study the responses of the output active power and the converter frequency, as shown in Fig. 5.20. From this figure, it can be seen how the frequency of the VSG with larger inertia constant is more reluctant to change, and an increase in the inertia constant leads to an increase in settling-time of the output frequency. However, it is indicated in the same figure that larger inertia constants result in larger ripples of the active power in steady-state. Nevertheless, from these results, we can clearly conclude that the proposed VSG control is capable of providing an inertial response even without the presence of an energy storage element. It is also noticeable that the transient response of P_{out} is slightly lower than the typical VSGs performance analyzed in [26], [27] due to the delay effect of the PLL. This effect can be lessened with an increased k_{δ}, as discussed in the stability analysis of section 5.4.3.

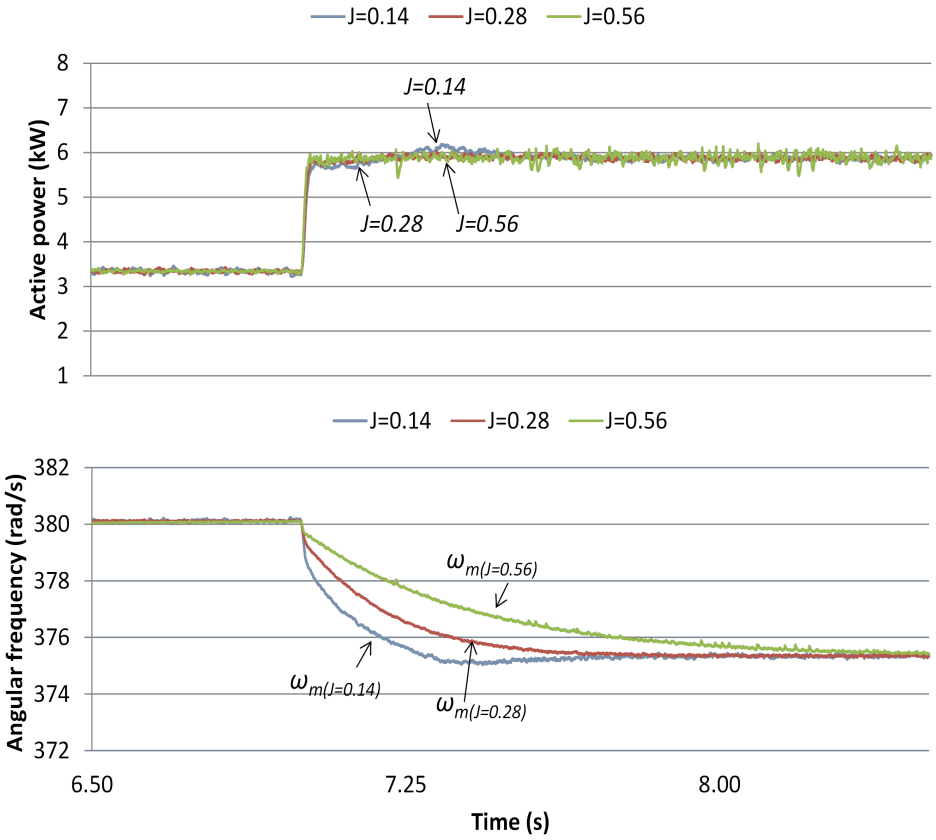

Fig. 5.20 The measured output frequency and output active power of the proposed method when the output load is changed from 3 kW + 1 kvar to 5.5 kW + 0.05 kvar during islanded operation mode.

5.6 Experimental Verification

To verify the simulation results, a scaled-down version of the simulation circuit depicted in Fig. 5.8 is conducted with the testbed illustrated in Fig. 5.21. Three-phase 30 Hz / 40 V (line-to-line RMS) input ac-source and 60 Hz / 60 V (line-to-line RMS) stepped-down grid voltage are considered for the experiment. The parameters indicated in Fig. 5.1 were respectively realized as follows, L_i = 7 mH, R_i = 0.1 Ω, L_o = 4 mH, R_o = 0.1 Ω, C = 30 μF and 2 μF for fictitious dc-link capacitor. These values are chosen from those available in the laboratory. S_{base} and V_{base} are changed to 150 W and 60 V, respectively. $k_\delta$is set to $2.5*{V_{base}}^2/X_o$, whereas other control parameters are the same as Table 5.3. The experiment scenarios are adopted from the simulations. First, the IBMC is set to operate in grid-connected mode, and then it is islanded from the grid and operates independently to supply local load. This is done to verify the grid-forming ability of the proposed control. Then the load changing is performed in the islanded operation to demonstrate the inertial behavior of the controller. Both the CSI and the VSR are controlled by a digital control unit Myway PE-Expert IV, and the presented data are internal variables of the control unit, which are recorded using the embedded function of PE-View X, the software interface of Myway PE-Expert IV, which can illustrate 100k data per second with 14 bit resolution for 16 channels. It is notable that the oscil-

loscope presented in Fig. 21 is only used for monitoring the synchronization process of the proposed control system based AC-source with the grid during the experiment. Additionally, HIOKI PW6001 Power analyzer was used to measure the THDs. To imply the FCS-MPC-based control, the sampling frequency for the VSR $(f_{s,vsr,mpc})$ is selected at 35 kHz for the CSI $f_{s,csi,mpc}$ at 20 kHz, respectively, which results in average switching frequency around 15 kHz for VSR and 10 kHz for CSI.

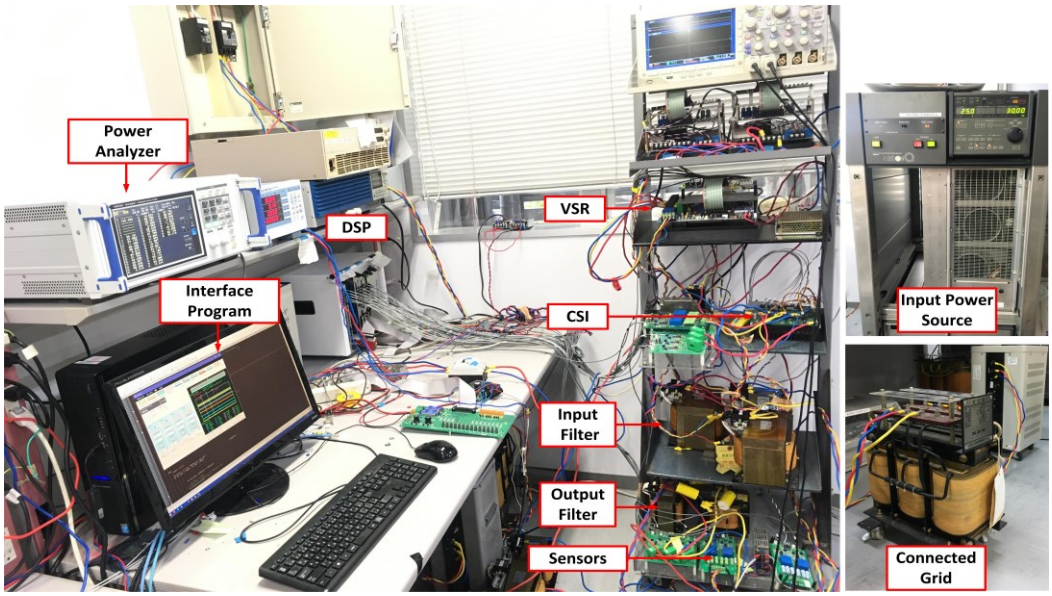

Fig. 5.21 Experimaental Testbed

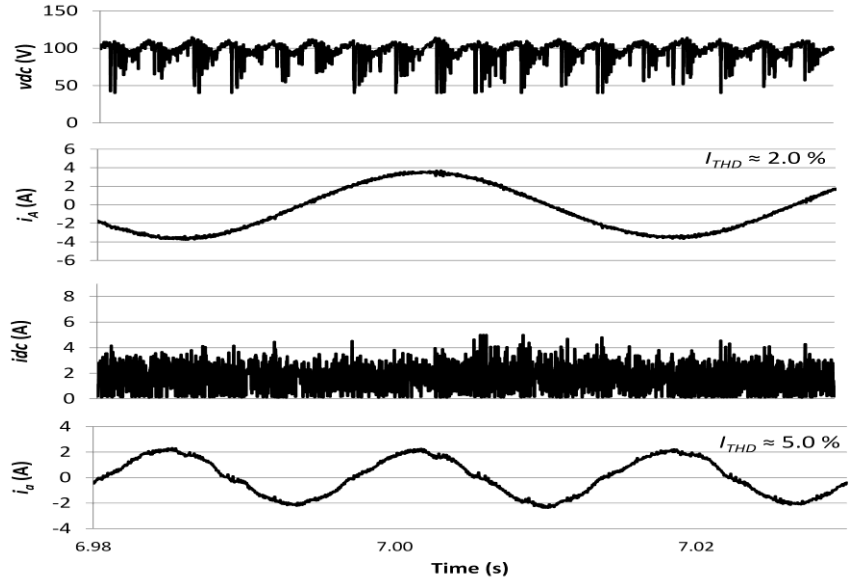

Fig. 5.22 Experimental results of steady-state wavwforms of the dc-link voltage, the phase-A input current, the dc-link current, and the phase-a output current of the proposed method during the grid-connected mode, from top to bottom, respectively.

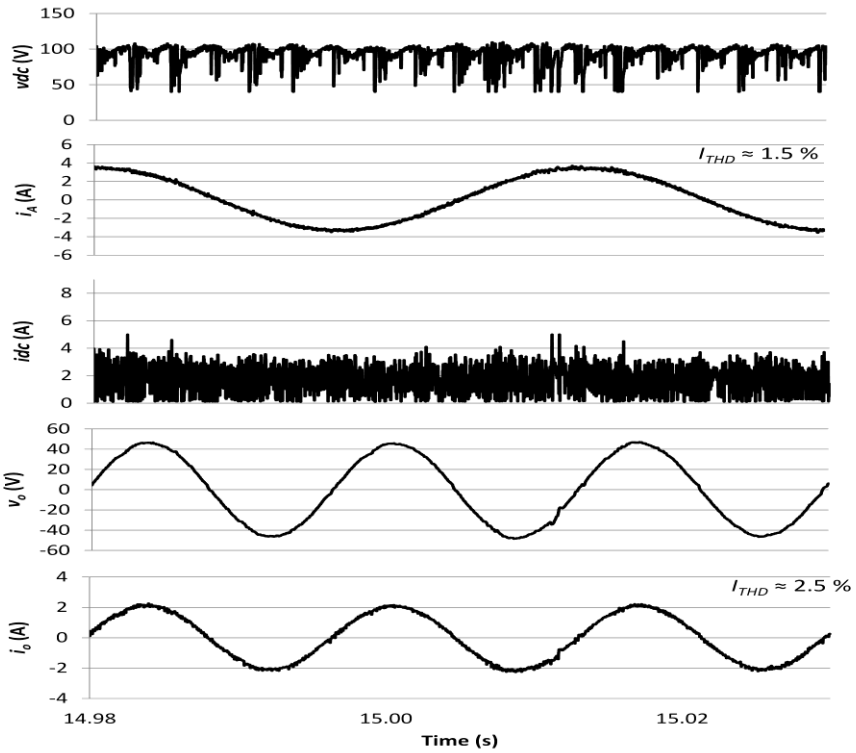

Fig. 5.23 Experimental results of steady-state wavwforms of the dc-link voltage, the phase-A input current, the dc-link current, the phase-a output voltage, and the phase-a output current of the proposed method during the islanded mode, from top to bottom, respectively.

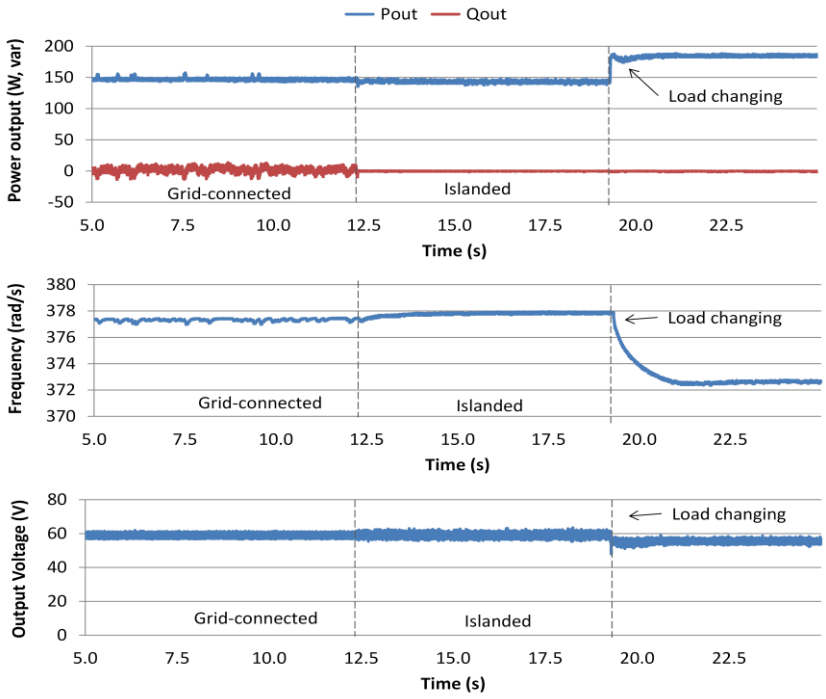

Fig. 5.24 Experimental results of the output active and reactive power, the output frequency, and the output voltage amplitude of the proposed method during the grid connected mode, islanded mode and load changing transition in islanded mode from top to bottom, respectively.

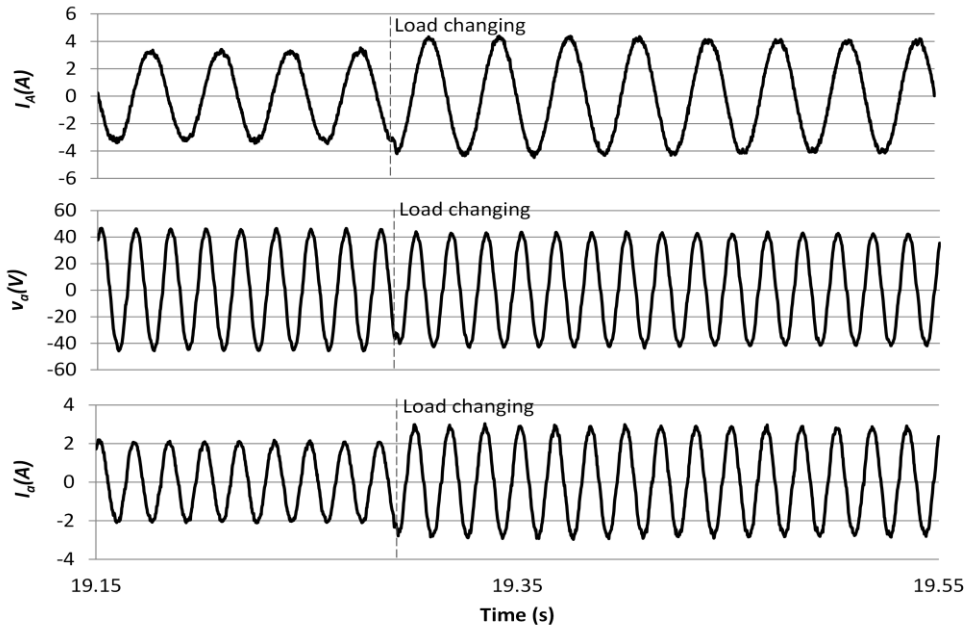

Fig. 5.25 Experimental results of transient waveforms of the phase-A input current, the phase-a output voltage, and the phase-a output current of the proposed method during load transition in the islanded

By comparing the experimental results displayed in Figs. 5.22 and 5.23 to the simulation results displayed in Figs. 5.13 and 5.17, it can be concluded that all comments on simulation results still stand for the experimental results. The dc-link voltage, the phase-A input current, the dc-link current, and the phase-a output current for the grid-connected operation are depicted in Fig. 5.22. This figure shows that both input and output current waveforms are sinusoidal. Additionally, the measured THDs up to the 50th order are also displayed in Fig. 5.22. It indicates that the THDs of the input and output currents are around 2.0% and 5.0%, respectively. This approves the results of the simulation study that the low order harmonic distortion due to the effect of *CL*-filter resonance can be suppressed by the multivariable control of filter voltage and current. Hence, the THDs of around 5.0% can be achieved even without a passive damping resistor. The dc-link voltage, the phase-A input current, the dc-link current, the phase-a output voltage, and the phase-a output current for the islanded operation illustrated in Fig. 5.23 indicates that current and voltage are also sinusoidal during islanded operation. The even lower THDs than grid-connected operation are observed for both input and output currents, which amount around 1.5% and 2.5%, respectively.

The output active and reactive powers, the output frequency, and the output voltage amplitude throughout the experiment scenarios are illustrated in Fig. 5.24. The input active and reactive powers are set to follow the reference values of $P^*_{in} = 150\,W$ and $Q^*_{in} = 0\,Var$. It can be seen that the system quickly and seamlessly transfers from the grid-connected mode into the islanded mode, supplying the power to a 20 Ω local load, whereas the output voltage amplitude of the system is maintained around the nominal value $(60\,V)$ throughout the operation. The system is also able to react to

the load changing during islanded operation when another star-connected 50 Ω local load is connected, as shown in Fig. 5.24 at $T \approx 19$ s and Fig. 5.25, where waveforms of the phase-A input current, the phase-a output voltage, and the phase-a output current are depicted. The results of the output frequency and the output active power verify the characteristic of VSG control, as discussed in Section 5.4. Hence, the experimental results clearly validate the effectiveness of the proposed control scheme.

5.7 Conclusions

The investigation on the IBMC has shown that the relevant existing control method is not explicitly designed for DG applications, and shortcomings such as the incapability of both grid-connected and islanded operation, the lack of virtual inertia, and the generation of distorted output current, exist in the control system. To solve these problems, a novel control scheme based on multivariable FCS-MPC for the implementation of VSG is proposed in this paper.

Comparative studies between the proposed control schemes and the existing method performed in PSCAD/EMTDC simulation have demonstrated that the proposed grid-forming control scheme offers many advantages over the existing methods, which utilize a grid-following strategy. For instance, thanks to the deployment of the proposed VSG control, the controller can provide the inertia property from the power source to support the grid frequency stability and is also capable of operating independently in islanded operation, maintaining the control of output voltage and output frequency actively. The utilization of the FCS-MPC ensures that an intricate coupling between the input control and output control of the IBMC is avoided and thus allowing a natural inclusion of VSG into the control system. Lastly, the proposed scheme generates approximately the same amount of current THD even without damping resistor to the existing PWM-based method with a damping resistor, owing to the inclusion of several control targets, variables, and constraints into a single cost function for simultaneous control. The effectiveness of the proposed control is also verified in a scale-down experiment, which highlights the grid-forming ability, the inertial behavior, and the active damping feature.

The presented work is an initial step to apply a VSG control in an AC/AC converter without a bulky energy storage element, and for future steps of this work, conducting experimental tests for a higher rating of IBMC are considered for evaluating and validating the proposed control strategy.

References

[1] E. J. Bueno, S. Cobreces, F. J. Rodriguez, A. Hernandez, and F.Espinosa, “Design of a back-to-back NPC converter interface for wind turbines with squirrel-cage induction generator,” *IEEE Trans. Energy Convers.*, vol. 23, no. 3, pp. 932–945, Sep. 2008.

[2] J. W. Kolar, T. Friedli, J. Rodriguez, and P. Wheeler, “Review of three phase PWM ac–ac converter topologies,” *IEEE Trans. Ind. Electron.*, vol. 58, no. 11, pp. 4988–5006, Nov. 2011.

[3] T. Friedli, J. W. Kolar, J. Rodriguez, and P. W. Wheeler, "Comparative Evaluation of Three-Phase AC–AC Matrix Converter and Voltage DC-Link Back-to-Back Converter

Systems," *IEEE Transactions on Industrial Electronics*, vol. 59, no. 12, pp. 4487-4510, Dec. 2012.

[4] P. Wheeler, J. Rodriguez, J. Clare, L. Empringham, and A. Weinstein, "Matrix converters: A technology review," *IEEE Trans. Ind. Electron.*, vol. 49, no. 2, pp. 276–288, Apr. 2002.

[5] Y. D. Yoon and S. K. Sul, "Carrier-based modulation technique for matrix converter," *IEEE Trans. Power Electron.*, vol. 21, no. 6, pp. 1691–1703, Nov. 2006.

[6] S. L. Arevalo, P. Zanchetta, P. W. Wheeler, A. Trentin, and L. Empringham, "Control and implementation of a matrix-converter-based AC ground power-supply unit for aircraft servicing," *IEEE Trans. Ind. Electron.*, vol. 57, no. 6, pp. 2076–2084, Jun. 2010.

[7] C. Klumpner, F. Blaabjerg, I. Boldea, and P. Nielsen, "New modulation method for matrix converters," *IEEE Trans. Ind. Appl.*, vol. 42, no. 3, pp. 797–806, May 2006.

[8] A. Escobar-Mejía, J. K. Hayes, J. C. Balda and C. A. Busada, "New control strategy for indirect matrix converters operating in boost mode," 2013 *IEEE Energy Conversion Congress and Exposition*, Denver, CO, 2013, pp. 2715-2720.

[9] P. C. Loh, F. Blaabjerg, F. Gao, A. Baby, and D. A. C. Tan, "Pulsewidth modulation of neutral-point-clamped indirect matrix converter," *IEEE Trans. on Industry Applications*, vol. 44, no. 6, pp. 1805-1814, Nov. 2008.

[10] P. C. Loh, R. J. Rong, F. Blaabjerg, and P. Wang, "Digital carrier modulation and sampling issues of matrix converters," *IEEE Trans. Power Electron.*, vol. 24, no. 7, pp. 1690–1700, Jul. 2009.

[11] J. W. Kolar, M. Baumann, F. Schafmeister, and H. Ertl, "Novel three-phase ac-dc-ac sparse matrix converter. Part I—Derivation, basic principle of operation, space vector modulation, dimensioning," *in Proc. 17th Annu. IEEE Appl. Power Electron. Conf. Expo*., Dallas (TX), vol. 2, Mar. 10–14, 2002, pp. 777–787.

[12] M. Baumann, F. Stogerer, and J. W. Kolar, "Novel three-phase ac-dc-ac ¨ sparse matrix converter. Part II—Experimental analysis of the very sparse matrix converter," *in Proc. 17th Annu. IEEE Appl. Power Electron. Conf. Expo*., Dallas (TX), vol. 2, Mar. 10–14, 2002, pp. 788–791.

[13] J. W. Kolar, F. Schafmeister, S. D. Round, and H. Ertl, "Novel three-phase ac–ac sparse matrix converters," *IEEE Trans. Power Electron*., vol. 22, no. 5, pp. 1649–1661, Sep. 2007.

[14] G.T. Chiang, and J. Itoh, "Comparison of two overmodulation strategies in an indirect matrix coverter," *IEEE Transactions on Industrial Electronics*, vol. 60, no. 1, pp. 43-53, January 2013.

[15] B. Ge, Q. Lei, W. Qian, and F.Z Peng, "A family of Z-source matrix converters," *IEEE Transactions on Industrial Electronics*, vol. 59, no. 1, pp. 35-46, January 2012.

[16] T. Wijekoon, C. Klumpner, P. Zanchetta, P.W. Wheeler, "Implementation of a Hybrid AC–AC direct power converter with unity voltage transfer," *IEEE Transactions on Power Electronics*, vol.23, no. 4, pp. 1918-1926, July 2008.

[17] X. Liu, P. Wang, P. C. Loh, and F. Blaabjerg, "Distributed generation interface using indirect matrix converter in boost mode with controllable grid side reactive power," *2012 10th International Power & Energy Conference (IPEC)*, Ho Chi Minh City, 2012, pp. 59-64.

[18] X. Liu, P. C. Loh, P. Wang, F. Blaabjerg, Y. Tang and E. A. Al-Ammar, "Distributed Generation Using Indirect Matrix Converter in Reverse Power Mode," *IEEE Transactions on Power Electronics*, vol. 28, no. 3, pp. 1072-1082, March 2013.

[19] J. Driesen and K. Visscher "Virtual synchronous generators," *in Proc. 2008 IEEE Power Energy Soc. Gen. Meeting—Convers. Del. Elect. Energy 21st Century*, pp. 1–3.

[20] Q.-C. Zhong and G. Weiss, "Synchronverters: inverters that mimic synchronous generators," *IEEE Trans. Ind. Electron*., vol. 58, no. 4, pp. 1259–1267, Apr. 2011.

[21] K. Sakimoto, Y. Miura, and T. Ise, "Stabilization of a power system including inverter type distributed generators by the virtual synchronous generator," *IEEJ Trans. Power and Energy*, vol. 132, no. 4, pp. 341–349, Apr. 2012.

[22] S. D'Arco and J. A. Suul, "Virtual synchronous machines - Classification of implementations and analysis of equivalence to droop controllers for microgrids," *2013 IEEE Grenoble Conference*, Grenoble, 2013, pp. 1-7.

[23] Q.-C. Zhong, P.-L. Nguyen, Z. Ma, and W. Sheng, "Self-synchronized synchronverters: inverters without a dedicated synchronization unit," *IEEE Trans. Power Electron.*, vol. 29, no. 2, pp. 617–630, Feb. 2014.

[24] M. Guan, W. Pan, J. Zhang, Q. Hao, J. Cheng, and X. Zheng, "Synchronous generator emulation control strategy for voltage source converter (VSC) stations," *IEEE Trans. Power Syst.*, vol. 30, no. 6, pp. 3093–3101, Nov. 2015.

[25] H. Wu, X. Ruan, D. Yang, X. Chen, W. Zhao, Z. Lv, and Q.-C. Zhong, "Small-signal modeling and parameters design for virtual synchronous generators," *IEEE Trans. Ind. Electron*., vol. 63, no. 7, pp. 4292–4303, Jul. 2016.

[26] J. Liu, Y. Miura and T. Ise, "Comparison of Dynamic Characteristics Between Virtual Synchronous Generator and Droop Control in Inverter-Based Distributed Generators," *IEEE Transactions on Power Electronics*, vol. 31, no. 5, pp. 3600-3611, May 2016.

[27] J. Liu, Y. Miura, H. Bevrani, and T. Ise, "Enhanced virtual synchronous generator control for parallel inverters in microgrids," *IEEE Trans. Smart Grid*, vol. 8, no. 5, pp. 2268–2277, Sep. 2017.

[28] J. Lei, B. Zhou, X. Qin, J. Wei, and J. Bian, "Active damping control strategy of matrix converter via modifying input reference currents," *IEEE Transactions on Power Electronics*, vol. 30, no. 9, pp. 5260-5271, Sept. 2015.

[29] J. Lei et al., "Feedback Control Strategy to Eliminate the Input Current Harmonics of Matrix Converter Under Unbalanced Input Voltages," *IEEE Transactions on Power Electronics*, vol. 32, no. 1, pp. 878-888, Jan. 2017.

[30] J. Rodriguez et al., "State of the Art of Finite Control Set Model Predictive Control in Power Electronics," *IEEE Transactions on Industrial Informatics,* vol. 9, no. 2, pp. 1003-1016, May 2013.

[31] H. Miranda, R. Teodorescu, P. Rodriguez, and L. Helle: "Model predictive current control for high-power grid-connected converters with output LCL filter", *Conf. of IEEE Ind. Electron*, Proc. 35th Annu, pp. 633-638, 2009.

[32] B. Arif, L. Tarisciotti, P. Zanchetta, J. C. Clare and M. Degano, "Grid Parameter Estimation Using Model Predictive Direct Power Control," *IEEE Transactions on Industry Applications*, vol. 51, no. 6, pp. 4614-4622, Nov.-Dec. 2015.

[33] J. Hu, J. Zhu, D. G. Dorrell: "Model predictive control of inverters for both islanded and grid-connected operations in renewable power generations", *IET Renewable Power Generation*, Vol. 8, Iss. 3, pp. 240-248, 2014.

[34] L. A. Serpa, S. Ponnaluri, P. M. Barbosa and J. W. Kolar, "A Modified Direct Power Control Strategy Allowing the Connection of Three-Phase Inverters to the Grid Through *LCL* -Filters," *IEEE Transactions on Industry Applications*, vol. 43, no. 5, pp. 1388-1400, Sept.-oct. 2007.

[35] F. Donoso, A. Mora, R. Cárdenas, A. Angulo, D. Sáez, and M. Rivera, "Finite-Set Model-Predictive Control Strategies for a 3L-NPC Inverter Operating With Fixed Switching Frequency," *IEEE Transactions on Industrial Electronics*, vol. 65, no. 5, pp. 3954-3965, May 2018.

[36] J. Jongudomkarn, J. Liu and T. Ise, "Virtual Synchronous Generator Control with reliable Fault Ride-Through Ability: A Solution based on Finite-Set Model Predictive Control," *IEEE Journal of Emerging and Selected Topics in Power Electronics*, early access. DOI: 10.1109/JESTPE.2019.2942943.

[37] P. Falkowski and A. Sikorski, "Dead-time compensation in a new FCS-MPC of an AC/DC converter with a *LCL* filter," *2016 13th Selected Issues of Electrical Engineering and Electronics (WZEE)*, Rzeszow, 2016, pp. 1-6.

[38] N. Panten, N. Hoffmann, and F. W. Fuchs, "Finite Control Set Model Predictive Current Control for Grid-Connected Voltage-Source Converters With *LCL* Filters: A Study Based on Different State Feedbacks," *IEEE Transactions on Power Electronics*, vol. 31, no. 7, pp. 5189-5200, July 2016.

[39] P. Falkowski and A. Sikorski, "Finite Control Set Model Predictive Control for Grid-Connected AC–DC Converters With *LCL* Filter," *IEEE Transactions on Industrial Electronics*, vol. 65, no. 4, pp. 2844-2852, April 2018.

[40] P. Correa, J. Rodriguez, M. Rivera, J. R. Espinoza, and J. W. Kolar, "Predictive Control of an Indirect Matrix Converter," *IEEE Transactions on Industrial Electronics*, vol. 56, no. 6, pp. 1847-1853, June 2009.

[41] M. Rivera, J. Rodriguez, B. Wu, J. R. Espinoza, and C. A. Rojas, "Current Control for an Indirect Matrix Converter With Filter Resonance Mitigation," *IEEE Transactions on Industrial Electronics*, vol. 59, no. 1, pp. 71-79, Jan. 2012.

[42] J. Lei et al., "Predictive Power Control of Matrix Converter With Active Damping Function," *IEEE Transactions on Industrial Electronics*, vol. 63, no. 7, pp. 4550-4559, July 2016.

[43] Y. Zhang, W. Xie, Z. Li and Y. Zhang, "Model Predictive Direct Power Control of a PWM Rectifier With Duty Cycle Optimization," *IEEE Transactions on Power Electronics*, vol. 28, no. 11, pp. 5343-5351, Nov. 2013.

[44] P. Cortes *et al.*, "Guidelines for weighting factors design in model predictive control of power converters and drives," in *Proc. IEEE ICIT*, 2009, pp. 1–7.

[45] P. Zanchetta, "Heuristic multi-objective optimization for cost function weights selection in finite states model predictive control," in *Proc. IEEE PRECEDE*, 2011, pp. 70–75.

[46] F. Villarroel *et al.*, "Multiobjective switching state selector for finite states model predictive control based on fuzzy decision making in a matrix converter," *IEEE Trans. Ind. Electron.*, vol. 60, no. 2, pp. 589–599, Feb. 2013.

[47] S. Alireza Davari, D. A. Khaburi, and R. Kennel, "An improved FCS-MPC algorithm for an induction motor with an imposed optimized weighting factor," *IEEE Trans. Power Electron.*, vol. 27, no. 3, pp. 1540–1551, Mar. 2012.

[48] B. M. Weedy, B. J. Cory, N. Jenkins, Janaka B. Ekanayake, Goran Strbac, *Electric Power Systems*. West Sussex, UK: Wiley, 2012, pp. 205–234.

[49] S. Golestan and J. M. Guerrero, "Conventional Synchronous Reference Frame Phase-Locked Loop is an Adaptive Complex Filter," *IEEE Transactions on Industrial Electronics*, vol. 62, no. 3, pp. 1679-1682, March 2015.

[50] J. Liu, Y. Miura, and T. Ise, "Fixed-parameter damping methods of virtual synchronous generator control using state feedback," *IEEE Access*, vol. 7, pp. 99177–99190, 2019.

Chapter 6
Conclusions

In this dissertation, FCS-MPC-based VSG control was applied to inverter-interfaced DGs, in order to improve the capacity of VSG control regarding the fault-ride-through ability and a separate FCS-MPC-based VSG control was adopted in indirect boost matrix converter-interfaced DGs in order to achieve the grid-forming control, the virtual inertial feature and to reduce the distortion of output current, as found in existing control methods for indirect boost matrix converter.

In Chapter 2, the principles of the primary VSG control were described, and a brief survey of other existing control schemes providing virtual inertia for inverter-interfaced DGs was presented. Then the brief history of MPC control for power converters and the principle and the necessary design procedure of FCS-MPC were introduced.

In Chapter 3, the implementation method of FCS-MPC-based VSG control in inverter-interfaced DGs is explained in detail. The simulation-based study was conducted to ensure that the proposed method indeed inherits the properties of PWM-based VSG control in both grid-connected and islanded operations.

In Chapter 4, a comparative study between the proposed FCS-MPC-based VSG control scheme, the VSG with virtual impedance current limiting, and the multiloop VSG control is presented for a three-phase-inverter-interfaced DGs regarding their FRT-abilities. Results from simulations and experiments have been conducted to show the superior performances of the proposed control in comparison with the existing controls in both grid-connected and islanded operations

In Chapter 5, a control scheme based on multivariable FCS-MPC is proposed for the implementation of VSG in indirect boost matrix converter-interfaced DGs. Comparative studies between the proposed control scheme and the existing methods for indirect boost matrix converter have demonstrated that the proposed control, which utilizes a grid-forming control scheme, offers many advantages over the existing methods, which utilize a grid-following strategy. For instance, the capability to operate in both grid-connected and islanded modes without control mode transition, the active damping ability, and the virtual-inertia-emulating- ability are all achieved.

The ideas and control methods based on FCS-MPC, as proposed in this dissertation, may contribute to the advancement of the capability of VSG control. As illustrated in Chapter 3 and 4, the proposed control can enhance the ability of the VSG control in the challenging aspects such as power quality and current control, granting the VSG control with abilities to prevent the system from overcurrent condition and to ride through fault, while the injection of non-sinusoidal current under conditions of unbalanced voltage sag was suppressed. Furthermore, the study of the possibility of integrating VSG control with different converter topologies other than two-level-inverters is conducted, as shown in Chapter 5 and according to “the author’s best knowledge,” this is the first study to make

the indirect boost matrix converter operate with smooth transition between islanded and grid-connected modes. It is also very rare to find a study in the literature that achieves the inertial feature of the VSG control in the AC-AC converter without the inclusion of a bulky DC-link capacitor, as it is done in chapter 5. Hence, the author believes that the work presented in this dissertation can be considered a significant contribution to the body of knowledge. With the presented enhanced VSG control strategies, a more robust distribution network with a high penetration rate of topologically diverse DGs can be expected in the future.

Still, there are several issues and challenges to be solved on the topic of the operation of VSG control, and there is also room for improvement for this work. For instance, with the multiple control objectives of MPC control, the capacity of the control method can be expanded with the inclusion of additional control terms. This can be a subject for further study. Besides, although the proposed control in Chapter 4 demonstrated a number of advantages over existing methods, the presence of ripple and harmonics need to be reduced to improve the power quality of FCS-MPC-based DG systems. The VSG control method proposed in Chapter 5 also needs to be verified in an experimental setup with a higher rating, as the simulation-based study cannot explore all the aspects of a real system, and the scale-down experiment platform might illustrate a different characteristic in a higher rating. Furthermore, it is fascinating to study whether the effect of the inertial response of an input power source with rotational inertia such as PMSG can be carried out to the grid-side converter of IBMC-interfaced-DGs. Lastly, the stability study of FCS-MPC methods in both Chapter 4 and Chapter 5 can be conducted to optimize the control system and improve the weighting factors selection methods of the proposed controls.

List of Publications

Journal Publications (with review)

[1] Jonggrist Jongudomkarn, Jia Liu, and Toshifumi Ise, "Virtual Synchronous Generator Control with reliable Fault Ride-Through Ability: A Solution based on Finite-Set Model Predictive Control," in *IEEE Journal of Emerging and Selected Topics in Power Electronics*, 2019, DOI: 10.1109/JESTPE.2019.2942943.

[2] Jonggrist Jongudomkarn, Jia Liu, Yuta Yanagisawa, Hassan Bevrani and Toshifumi Ise, "Model Predictive Control for Indirect Boost Matrix Converter Based on Virtual Synchronous Generator, " in *IEEE Access,* 2020, DOI: 10.1109/ACCESS.2020.2983115.

Papers Presented at International Conferences (Oral presentation, with review)

[1] Jonggrist Jongudomkarn, Jia Liu, and Toshifumi Ise, "Virtual Synchronous Generator Control with Reliable Fault Ride-through Capability by Adopting Model Predictive Control" *International Power Electronics Conference, IPEC-Niigata - ECCE Asia 2018*, art. no. 8507402, 2018, pp. 3902-3909.

[2] Jonggrist Jongudomkarn, Jia Liu, and Toshifumi Ise, "Comparison of Current-Limiting Strategies of Virtual Synchronous Generator Control during Fault Ride-Through" *10th IFAC Symposium on Control of Power and Energy Systems, CPES 2018-Tokyo, Japan, 2018*, pp. 256-261.

Acknowledgments

I would like to take this opportunity to express my best gratitude and appreciation to all the people who have helped me during the doctoral course study at Osaka University.

First, I would like to express my sincere gratitude to my first and previous supervisor, Professor Toshifumi Ise, in the Graduate School of Engineering, Osaka University, for his continuous support for my researches and daily life. I also present my sincere appreciation to Dr. Jia Liu, assistant professor at the Graduate School of Engineering, Osaka University, for his kindness and insightful advice on my researches. The door to my supervisors' office was always open whenever I ran into trouble, spot, or had a question about my research or writing. They consistently steered me in the right direction whenever I needed it. Without their persistent help throughout the years of my study, this dissertation would not have been possible.

My sincere thanks also go to my current supervisor Professor Shigemasa Takai in the Graduate School of Engineering, Osaka University, for his careful review of this dissertation that helps me improve the quality of the work tremendously.

Besides, I would like to express my thanks to the other members of my dissertation committee: Professor Tsuyoshi Funaki, Professor Tomoo Ushio, Professor Hiroyuki Shiraga and Invited Professor Shigekazu Sakabe in the Graduate School of Engineering, Osaka University, for their valuable comments and encouragement, and for their challenging questions which incented me to widen my research from various perspectives.

I would like to extend my sincere gratitude to Professor Hassan Bevrani in the Department of Electrical Engineering, University of Kurdistan, Iran, for his helpful advice on my researches and constructive guidance, especially during the revision of my manuscript.

I would like to express my thanks to other staff at Osaka University for their help and supports during the doctoral course study.

I would also like to thank my fellow doctoral students and all present and graduated members of Ise Laboratory, Graduate School of Engineering, Osaka University, for their feedback, cooperation, their kindful help, and of course, friendship.

This work would not have been possible without the financial support received through the Hitachi foundation scholarship to undertake my doctoral course study.

Nobody has been more important to me in the pursuit of this doctoral degree than the members of my family. I would like to thank my parents, whose love and guidance are with me in whatever I pursue.They are the ultimate role models. Most importantly, I wish to thank my wife, Peachaya Jongudomkarn, and my son, Pakin Jongudomkarn, who has been by my side throughout these years. Without your love, spiritual support, sacrifice, and encouragement, I would not have had the determination and the courage to embark on this journey in the first place.